Quantum Resource Engineering

Michael Robert HANKS

Doctor of Philosophy

Department of Informatics
School of Multidisciplinary Sciences
The Graduate University for Advanced Studies,
SOKENDAI

SOKENDAI (THE GRADUATE UNIVERSITY FOR ADVANCED STUDIES)

DOCTORAL THESIS

Quantum Resource Engineering

Author:
Michael Robert HANKS

Supervisor:
Professor Kae NEMOTO

A thesis submitted in fulfillment of the requirements
for the degree of Doctor of Philosophy

in the

Department of Informatics
School of Multidisciplinary Sciences
SOKENDAI (The Graduate University for Advanced Studies)

March 2019

National University
SOKENDAI
The Graduate University for Advanced Studies

Inter-University Research Institute Corporation /
Research Organization of Information and Systems
National Institute of Informatics

Committee

Advisor Dr. Kae NEMOTO
Professor of The National Institute of Informatics/SOKENDAI

Subadvisor Dr. Ken HAYAMI
Professor of The National Institute of Informatics/SOKENDAI

Subadvisor Dr. Mio MURAO
Professor of The University of Tokyo

Examiner Dr. Takeaki UNO
Professor of The National Institute of Informatics/SOKENDAI

Examiner Dr. Yasuhiro TOKURA
Professor of The University of Tsukuba

Examiner Dr. Andrew GREENTREE
Professor of RMIT University, Australia

Examiner Dr. Keiji MATSUMOTO
Associate Professor of The National Institute of Informatics/SOKENDAI

SOKENDAI (THE GRADUATE UNIVERSITY FOR ADVANCED STUDIES)

Abstract

School of Multidisciplinary Sciences
Department of Informatics

Doctor of Philosophy

Quantum Resource Engineering

by Michael Robert HANKS

The discovery of quantum mechanics introduced principles such as entanglement having no classical counterparts. These are now known to allow a twenty-first century technological paradigm shift: Quantum technologies promise unparalleled performance in certain areas of computation, physical simulation, secure communication, and metrology. These promises prompt an investigative process targetting the reliable control of small-scale physical systems. On the design front, schemes for control, communication, and the protection of information have been developed. On the discovery front, a range of disparate physical systems including among others quantum dots, trapped ions, crystal defects, and superconducting circuits, have been investigated for suitability in the machinery of *quantum information processing*. This process of design and discovery forms the immediate context for the work contained in this two-part thesis.

Following a brief general introduction, the first part begins with the protection of information against local noise. Initially, I consider the utility of strong coupling in the protection of Greenberger-Horne-Zeilinger (GHZ) states for quantum sensing. Here it is found that such strong coupling narrows the gap between the sensitivity of the composite sensor and the Heisenberg limit, and that the form of the coupling with distance defines the optimal size of each GHZ state. I then turn to consider the impact of local information on the logical error rate of small-scale topological quantum error correction codes; I show how such information reduces resource requirements.

In the second part I look at how physical qubits might be implemented, considering two defect centers in diamond: The nitrogen–vacancy center and the silicon–vacancy center. Beginning with the nitrogen–vacancy center, I build upon the earlier work of others to show that projective spin measurements via cavity reflection statistics can in principle be achieved with operational fidelities sufficient for fault tolerant quantum information processing. By way of comparison, I then turn to consider measurement and single-qubit rotations on the electronic state of the silicon–vacancy center, but am forced to conclude that despite its promising optical properties, such operations are not forthcoming with the silicon–vacancy center to fidelities sufficient for fault tolerant quantum information processing. I end by linking results in this second part with prior proposals, describing the potential of a nitrogen–vacancy center photonic module for distributed quantum information processing tasks. I argue that the potential of such modules for high-fidelity entangled link generation puts them in a promising position to implement near term proof-of-principle devices for quantum repeaters and distributed parameter estimation, and that this promise further extends in the longer term to large-scale quantum computation.

Preface

Motivation and Opinion The field of quantum information processing has advanced in leaps and bounds since its conception in the 1980s [1–4]. Algorithms and protocols have been developed for a series of interesting and rewarding applications, and in quantum cryptography and nano-scale sensing the developments in this field are already contributing to commercial society. Progress does not proceed at a constant rate or difficulty, however, and it seems we now face a crossroads: Long-term, high-impact, commercial developments appear to require a level of scalability, either in size or in time, with no ready solution. Each member in the canonical set of physical systems, such as trapped ions and superconducting circuits, seems limited by its own specific fundamental challenges, and the recent surge in commercial interest threatens either to cement the position of the first such system to cross the scalability-threshold or to cause a collapse in interest akin to the so-called *AI Winter* in artificial intelligence research.

It has been said that we now operate in the *noisy intermediate-scale quantum* era [5]. This era is characterised by severe resource limitations, both in qubit number and in time; in contrast to the strict modularisation of the abstraction hierarchy for classical information processing, questions of the design and operation of quantum information processing devices at all levels of abstraction will need to be considered in conjunction with one another. The compilation process for the superconducting-circuit quantum system made available for public use by IBM provides a representative example: Users are forced to consider the physical layout of qubits and local expected operational fidelities at compile-time. Further, the large qubit numbers required for quantum error correction imply that, even once *scalable* operation is reached in the limited sense of the requirements of quantum error correction codes, resource limitations will continue to play a major role in device design and operation, if only due to the sheer magnitude of the costs involved. It is therefore in our interest to consider in detail those resources and methods available to us, to engineer greater levels of efficiency.

There has been an apparent rift between those researchers more immediately interested in demonstrating near-term *quantum supremacy* [6] and those with their sights fixed on continuing the long march toward scalability. Stable interest and development appears to me to require a path *both* allowing for gradual refinement of current technologies in the near term while simultaneously laying the groundwork to meet those larger long-term challenges. To the best of my knowledge, there appear to be four commercially significant applications that can be refined in the near-term: quantum cryptography, quantum random number generation, quantum optimisation algorithms, and quantum metrology. Each of these applications places emphasis on a different aspect of the eventual composite quantum information processing system: Among other considerations, quantum cryptography depends on the quality and repetition rate of single-photon sources and detectors; quantum random number generation depends on the characterisation and speed of single-qubit rotations and measurements; quantum optimisation algorithms appear to depend

on minimising collective and inhomogeneous noise in many-qubit systems with local interactions; and quantum metrology appears to depend on the ability to generate and maintain entangled states, as well as on selective system–environment interactions. In this thesis I have chosen to focus primarily on aspects relevant to the generation and maintenance of entangled states. These are most relevant in the near-term, in my estimation, to quantum metrology, in the mid-term to (perhaps partially error corrected) quantum communication, and in the long-term to the generation of the fully error corrected states of quantum computation.

Structure, Origins and New Results Following a general introductory history to set the context of the work, I have arranged the structure of this report into five sections, grouped into two parts.

In Part I, I consider general schemes for reducing the impact of local noise for small-scale, near-term quantum devices. Chapter 2 begins with a consideration of the potential role of strong-coupling in quantum sensing. It is based on the published work of the same name, *robust quantum sensing with strongly interacting probe systems* [7], performed in conjunction with Shane Dooley, Shojun Nakayama, William J. Munro, and Kae Nemoto. This work was supported in part by the MEXT KAKENKHI Grant number 15H05870. The presentation has however been re-worked to relate the results more directly with the overarching theme of this report, and to avoid plagiarisation of Dr Shane Dooley, to whom is owed primary credit for the authorship of the original text. We are very grateful to Yuichiro Matsuzaki for helpful discussions. The essential feature of this section is the application of strong coupling for passive state protection, a feature well known among researchers interested in passive error mitigation, to quantum sensing. In this way the reduced efficacy of active correction schemes in the presence of one-way relaxation processes is overcome while yet allowing for dynamical decoupling, so that such relaxation processes may remain a limiting factor. Results are presented for a range of inter-qubit coupling strengths and environment temperatures, optimal qubit numbers are determined as a function of the relaxation rate and the form of the interaction with distance, and the example of superconducting flux qubits is described to suggest the near-term utility of the scheme. The two key resources of quantum sensing are time and the number of probe systems; by engineering the composite energy level structure of our system, we enhance the efficiency of these resources as expressed by the *sensitivity* parameter. Chapter 3 continues the discussion of local noise mitigation with a look at the role of local information in the decoding of the *repetition code* and the *surface code* for the protection of quantum states. This work has not yet been published elsewhere, and was performed in conjunction with William J. Munro and Kae Nemoto. Fruitful discussions on this work were had with Simon Devitt and Ashley Stephens, to whom we owe many thanks. The key result of this section is an improvement in resource efficiency when local information is taken into account during the decoding process: the *code distance* (related to the required number of qubits) associated with a given logical error rate is reduced with a magnitude depending on the proximity of the physical error rate to the *accuracy threshold* of the code (the maximum physical error rate for which the logical error rate is not increased). An averaged approach to local information for table-lookup and localised decoding schemes is suggested, a breakdown of these effects for large-scale systems is predicted, and the importance of this resource reduction in the near-term is highlighted.

In contrast to the largely system-agnostic discussion of noise in Part I, Part II considers the implementation of single-qubit gates, particularly measurement, on specific physical systems: The nitrogen–vacancy and silicon–vacancy defect centers

in diamond. Chapter 4 leads this part with a theoretical performance estimate for an indirect measurement of the electronic spin of the nitrogen–vacancy center based on the reflection statistics of a coupled optical cavity. It is based on the published work of the same name, *high fidelity spin measurement on the nitrogen–vacancy center* [8], performed in conjunction with Michael Trupke, Jörg Schmiedmayer, William J. Munro, and Kae Nemoto. This project was made possible through the support of a grant from the John Templeton Foundation. The opinions expressed in this publication are those of the authors and do not necessarily reflect the views of the John Templeton Foundation (JTF #60478). We also acknowledge support from the MEXT KAKENHI Grant-in-Aid for Scientific Research on Innovative Areas "Science of Hybrid Quantum Systems" Grant No. 15H05870. This section opens with an overview of the relevant properties of the nitrogen–vacancy center, followed by a description of the single-photon measurement process considered and its model. Idealised measurement time and fidelity estimates are provided for current and near-term technology. The impacts of the photon bandwidth on the pulse time and the required cavity decay rate are then incorporated, before providing estimates of the additional error incurred by introducing weak coherent light sources in place of single-photon sources. The section ends with a brief discussion stressing the roles of weak coherent light sources and single-photon sources in the near- and long-term respectively. Chapter 5 estimates the achievable performance of single-qubit rotations and spin measurements for the negatively charged silicon–vacancy center in diamond. This previously unpublished work was performed in conjunction with William J. Munro and Kae Nemoto, and we thank Michael Trupke for helpful discussions. Following an overview of the relevant known properties of the silicon–vacancy center, we lead the analysis by justifying a particular field configuration and qubit encoding with respect to the center's energy level structure and decay processes. The adoption of the measurement scheme introduced in the previous section is justified, and performance estimates are given. Unlike the preceding work for the nitrogen–vacancy center, however, this section additionally provides and explains performance estimates for optical stimulated Raman adiabatic passage (STIRAP) single-qubit rotations. We conclude with a discussion emphasising the potential use of silicon–vacancy centers in small-scale or rate-dependent (in contrast to fidelity-dependent) applications. Finally, in Chapter 6 I conclude Part II by outlining potential goals for the near-, mid-, and long-term. This broad discussion is based on the published conference proceedings paper of the same name, *a universal quantum module for quantum communication, computation, and metrology* [9], written in conjunction with Nicoló Lo Piparo, Michael Trupke, Jörg Schmiedmayer, William J. Munro, and Kae Nemoto. However, certain elements have been modified and added to increase the compatibility of that text with this wider report. This section begins by expressing certain of the results in Chapter 4 in the language of rates and probabilities, suitable for the proposed applications to follow. Sections 6.4-6.6 then explain and provide loose performance estimates for

1. single-node, heralded, memory-assisted quantum communication,
2. distributed quantum sensing, and
3. cluster state generation for quantum computation.

After providing a brief comparison with the silicon–vacancy center considered in the preceding section, we conclude by emphasising the suitability of the nitrogen–vacancy center photonic module both for the current resource-limited era and looking further toward scalable quantum information processing.

Though connected by the overall theme and goals of this thesis, the content of each section above is commonly approached as a distinct sub-field in its own right. For this reason, for the sake of those readers with particular interests each section is written to be as self-contained as possible.

The report concludes with a very brief final chapter, wherein I summarise and discuss my hopes for the direction along which this report might contribute to the development of quantum information processing devices.

Acknowledgements First and foremost I must thank my advisor, Kae Nemoto, for allowing me the opportunity to pursue this PhD programme, with the generous assistance of the Japanese government under a Monbukagakusho scholarship, and for her constant support and guidance.

I am also deeply indebted to Bill Munro for invaluable discussions and for his atmosphere of infectious enthusiasm.

There are many people to whom I am grateful for thought-provoking conversations, among whom a small but significant fraction are Michael Trupke and Jörg Schmiedmayer of TU Vienna, Simon Devitt of the University of Sydney Australia, Andrew Greentree of RMIT Australia, Ashley Stephens, Mio Murao of the University of Tokyo Japan, Yuichiro Matsuzaki of NTT Japan, Todd Tilma of Titech Japan, and Mark Everitt of Loughborough University UK.

My time in Tokyo would not have been possible without the patient support of the administrative staff at the National Institute of Informatics. In particular I am deeply grateful to Horishita-san and his team, and also to Megumi Kunioka, Tomoko Uchida, Fumiaki Matsuoka, and Yukiko Sanaka.

It has been a privilege to spend my time here at the National Institute of Informatics surrounded by such friendly and knowledgable people, and so I'd like to thank Burkhard Scharfenberger, Emi Yukawa, Shane Dooley, Shojun Nakayama, Nicoló Lo Piparo, Yusuke Hama, Jaeha Lee, Zeliang Xiang, Victor Bastidas-Valencia, Marta Estarellas, Claude Gravel, Tomo Osada, and Katsuya Furusho.

In a broader sense my time in Japan has been immeasurably improved thanks to the kindness of the personal friendships I have enjoyed in my time here. My warmest wishes to Vanessa, Marlene, Amelia, Michael, Koharu, Karen, Chika, Natalia, Tim, Jenny, Nanako, Ivan, Jihye, Conwin, Maki, Nariko, Noriko, Akemi, Sophia, Miyako, and Andrew.

Finally, I wouldn't be where I am today without the love and support of my family. Much love to my parents, Robert and Amanda, and my brother Chris.

List of Publications

Journal Articles

- Hanks, M., Trupke, M., Schmiedmayer, J., Munro, W. J., & Nemoto, K. (2017). High-fidelity spin measurement on the nitrogen-vacancy center. New Journal of Physics, 19(10), 103002.
- Dooley, S., Hanks, M., Nakayama, S., Munro, W. J., & Nemoto, K. (2018). Robust quantum sensing with strongly interacting probe systems. npj Quantum Information, 4(1), 24.
- Hanks, M., Munro, W. J., & Nemoto, K. (2018). Modelling optical operations on the negatively charged silicon–vacancy center in diamond. *Submitted to Physical Review A*.
- Hanks, M., Munro, W. J., & Nemoto, K. (2018). Decoding quantum error correction codes with local variation. *In Preparation*.

Conference Proceedings

- Hanks, M., Piparo, N. L., Trupke, M., Schmiedmayer, J., Munro, W. J., & Nemoto, K. (2017, August). A universal quantum module for quantum communication, computation, and metrology. In Quantum Photonic Devices (Vol. 10358, p. 103580K). International Society for Optics and Photonics.

Contents

Abstract v

Preface vii

List of Publications xi

1 An Introductory History of Quantum Information Processing 1
1.1 Reversible Computing . . . 2
1.2 Generalisation of Quantum Operations . . . 4
1.3 Quantum Algorithms . . . 5
1.4 Development of Universal Quantum Gate Sets . . . 6
1.5 Quantum Error Correction . . . 7
1.6 Modern Challenges . . . 9

I Local Noise in Near-Term Applications 11

2 Robust quantum sensing with strongly interacting probe systems 13
2.1 Quantifying Measurement Performance . . . 14
2.2 GHZ Sensing . . . 16
2.2.1 Ideal Conditions . . . 16
2.2.2 The Effect of Noise . . . 17
2.3 Temperature and Coupling Strength . . . 18
2.4 An Example . . . 18
2.5 Noise Spectra . . . 19
2.6 Short-Range Interactions . . . 20
2.7 Discussion . . . 22

3 Decoding Quantum Error Correction Codes with Local Variation 23
3.1 Quantifying Significance . . . 24
3.2 The Repetition Code and Chain Length . . . 25
3.2.1 The Impact of Local Variance . . . 26
3.3 The Surface Code and Chain Entropy . . . 27
3.3.1 Lattice Dimension . . . 30
3.4 Discussion . . . 31

II Physical Platform: Defect Centers in Diamond 35

4 High-Fidelity Spin Measurement on the Nitrogen–Vacancy Center 37
4.1 Introduction . . . 37
4.2 The Nitrogen–Vacancy Center . . . 38
4.3 Photonic Readout of the Nitrogen–Vacancy Center State . . . 42
4.4 Simulation of the Measurement Process . . . 45

4.4.1 Realistic Performance Estimate . . . 49
4.4.2 Single Photon Pulses . . . 50
4.5 Weak Coherent Pulses . . . 51
4.6 Discussion . . . 53

5 Operations on the Negative Silicon–Vacancy Center in Diamond 55
5.1 Introduction . . . 55
5.2 The Silicon–Vacancy Center . . . 56
5.3 Qubit Subspace and External Fields . . . 58
5.4 Measurement and Initialisation of the Electronic Spin State . . . 61
5.5 Population Transfer between Spin States . . . 63
5.6 Discussion . . . 65

6 A Universal Quantum Module for Quantum Communication, Computation and Metrology 67
6.1 Introduction . . . 67
6.2 The NV–Cavity Module . . . 68
6.3 Silicon– and Germanium–Vacancy Centers . . . 69
6.4 Quantum Communication . . . 70
6.5 Quantum Metrology . . . 75
6.6 Quantum Computation . . . 77
6.7 Discussion . . . 79

7 Conclusions and Future Work 81

A Numerical Methods 83
A.1 Dynamical Evolution . . . 83
A.2 Scattered Light . . . 83
A.3 Decoding Random Error Configurations . . . 84

List of Figures

1.1 Toffoli's Reversible AND Gate . . . 3
1.2 Toffoli's Universal Gate Set . . . 3
1.3 A Universal Quantum Gate Set . . . 6
1.4 Shor's Quantum Error Correction Code . . . 8

2.1 Spin System Energy Level Structure . . . 14
2.2 Sensitivity with Temperature . . . 18
2.3 Sensitivity with Environment Spectral Density . . . 20
2.4 Sensitivity with Spin Number . . . 21

3.1 Fraction of Logical Errors of Weight $\lfloor \frac{L}{2} \rfloor$ . . . 25
3.2 The Repetition Code . . . 26
3.3 Ratio between the Effects of Variability and Increased Length . . . 27
3.4 Repetition Code Logical Error Rates . . . 28
3.5 Surface Code Diagram . . . 29
3.6 Surface Code Logical Error Rates . . . 32

4.1 NV^- Center Module and Energy Level Diagram . . . 40
4.2 Cavity–Reflection Measurement Overview . . . 42
4.3 Cavity Reflection Spectrum for the NV^- Module . . . 46
4.4 NV^- Measurement Single-Photon Pulse Count and Fidelity with Cavity-Cooperativity . . . 47
4.5 NV^- Measurement Error with Cavity-Cooperativity and Maximum Pulse Number . . . 48
4.6 NV^- Measurement Error with Source and Detector Inefficiency . . . 48
4.7 NV^- Charge State Switching Rate Upper Bound . . . 52
4.8 NV^- Measurement Fidelity with Coherent Light by Pulse Number and Mean Photon Number . . . 52

5.1 SiV Energy Level Structure . . . 57
5.2 SiV Decoherence . . . 60
5.3 SiV Reflection Curves . . . 62
5.4 Measurement Fidelity . . . 64
5.5 STIRAP pulse for population transfer through the optically excited states . . . 65

6.1 Single Node Memory-Assisted Quantum Communication Scheme . . . 71
6.2 Quantum Communication Scheme Circuit . . . 72
6.3 Secret Key and Entanglement Distribution Rates with Distance . . . 74
6.4 Quantum Sensing Circuit and Interaction Graph . . . 76
6.5 Percolation-based Cluster State Generation . . . 78

List of Tables

2.1 Superconducting Flux Qubit Sensitivity 19

4.1 NV^- Center Excited State Energies, Lifetimes, and Transitions 41
4.2 NV^- Measurement Fidelity and Pulse Number with Cavity-Cooperativity and Source and Detection Efficiencies 49

5.1 SiV^- Measurement Fidelity and Pulse Number with Cavity-Cooperativity and Source and Detection Efficiencies 63

List of Abbreviations

CQED	**C**avity **Q**uantum **E**lectro-**D**ynamics
GHZ	**G**reenberger-**H**orne-**Z**eilinger
LDPC	**L**ow-**D**ensity **P**arity **C**heck
NISQ	**N**oisy **I**ntermediate-**S**cale **Q**uantum
NV$^-$	Negatively-Charged **N**itrogen–**V**acancy Center in Diamond
QIP	**Q**uantum **I**nformation **P**rocessing
QC	**Q**uantum **C**omputing
QEC	**Q**uantum **E**rror **C**orrection
RC	**R**eversible **C**omputing
SiV$^-$	Negatively-Charged **S**ilicon–**V**acancy Center in Diamond
STIRAP	**Sti**mulated **R**aman **A**diabatic **P**assage

Chapter 1

An Introductory History of Quantum Information Processing

The computing revolution of the twentieth century was one of the most significant developments in the history of mankind. Steady exponential improvement in the speed and size of modern computers over roughly the past seventy years since the invention of the transistor has changed — and digitised — almost every aspect of our lives.

Since the 1980s [1–4], it has been realised that quantum mechanics offers the potential to revolutionize certain important information processing tasks. Such tasks fall under the categories of secure communication [10–13], precise and accurate metrology and measurement [14–16], the simulation of physical systems [17], and computation tasks such as the famous prime factorisation problem that lies at the heart of most modern public key cryptography [18]. Landmark discoveries, such as Wiesner's conjugate coding [2], the factoring and search algorithms of Shor [18] and Grover [19], or the correction of error in an arbitrary and unknown quantum state [20–22], promise to achieve with technology based on the principles of quantum physics what cannot be achieved with conventional, *classical* machines alone.

There is an expected progression to the development of technologies to accomplish these tasks:

1. Basic (single-qubit) quantum communication and nano-scale metrological applications to encoded- and entangled-state metrology,

2. communication with quantum repeaters (further split into short-term and fully-scalable schemes),

3. simulation of systems with restricted operation sets and $O(100)$ atomic elements, and

4. universal quantum computation.

The applications of point (4), universal quantum computation, will in general require from thousands to billions of entangled qubits [23, 24] and a universal set of quantum operations.

To understand the challenges ahead for quantum information processing, it can help to put these challenges in the context of the historical development of the field. This introductory chapter seeks to do just that, to explain the stages of development of quantum information processing, how they distinguished themselves from their classical foundations, and the unique aspects of the challenges they face.

1.1 Reversible Computing

1960 was a time of rapid and exciting progress in computer technology. Designers were leaving behind vacuum tubes, which were large and generated significant amounts of heat, in favour of transistors (the first computer made from transistors was built in 1953) and magnetic cores (developed also in 1953). Further, the invention of the integrated circuit in 1958 promised to continue the trend of making computers faster, cheaper, and more efficient.

> *"What I want to talk about is the problem of manipulating and controlling things on a small scale.*
> *As soon as I mention this, people tell me about miniaturization, and how far it has progressed today. They tell me about electric motors that are the size of the nail on your small finger. And there is a device on the market, they tell me, by which you can write the Lord's Prayer on the head of a pin. But that's nothing; that's the most primitive, halting step in the direction I intend to discuss. It is a staggeringly small world that is below. In the year* 2000*, when they look back at this age, they will wonder why it was not until the year* 1960 *that anybody began seriously to move in this direction.*
> *Why cannot we write the entire* 24 *volumes of the Encyclopaedia Brittanica on the head of a pin?"*
>
> — Richard Feynman, There's Plenty of Room at the Bottom, 1960 [25]

This milieu, the march toward small, efficient machines, caused people to wonder about the extent to which such progress might continue — *Moore's Law*, observing the exponential growth of transistor circuits, was first described in 1965 [26]. Was there a fundamental law, akin to the second law of thermodynamics, that would ultimately impede progress? It was known that energy (and heat) dissipation was linked to the entropy of the system via this second law: Brillouin [27] and others had argued that each measurement would necessarily dissipate some energy on the order of $k_B T$, the thermal energy associated with a classical degree of freedom, where k_B is Boltzmann's constant and T is the operating temperature. Concerned that such arguments about measurement might not apply to data processing generally, Landauer in 1961 [28] extended them in this direction based on two fundamental arguments: Firstly, he argued that initialisation (or *set*) operations cannot be performed without dissipation, because the result does not depend on the initial state and these therefore cannot be reversible; secondly, though recognising that additional, fixed-state bits can be used to bias truth tables and simulate irreversible classical logical gates, he argued that the storage of extraneous intermediate results would cause the required memory to increase unmanageably. It seemed as if there were indeed a limit.

Landauer's thinking was overturned in 1973 by Bennett [29], when he described a scheme for completely reversible computing without the explosion in memory cost predicted by Landauer. Bennett's scheme had two fundamental ideas: firstly, assuming the use of redundant control bits as described by Landauer to bias the truth tables of logical gates, Bennett proposed a *compute – copy output – uncompute* sequence to avoid throwing away information at the end of a computation despite re-initialisation of the machine; secondly, Bennett suggested that this could be done many times with intermediate steps during the computation, to avoid needing to store the entire history (junk output) across the computation as a whole.

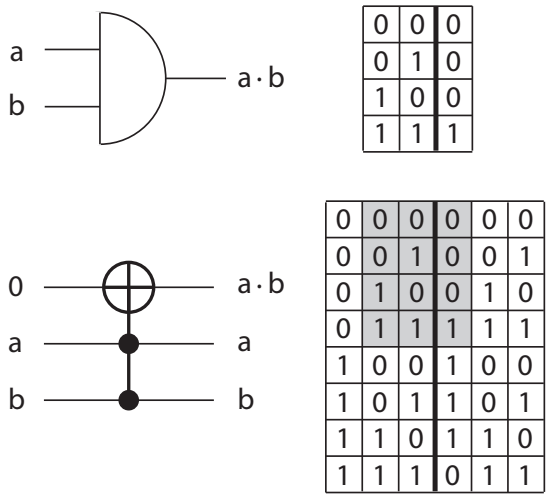

0	0	0
0	1	0
1	0	0
1	1	1

0	0	0	0	0	0
0	0	1	0	0	1
0	1	0	0	1	0
0	1	1	1	1	1
1	0	0	1	0	0
1	0	1	1	0	1
1	1	0	1	1	0
1	1	1	0	1	1

FIGURE 1.1: Toffoli's reversible AND gate. Though the AND gate in its original form (top) is not reversible as the size of the state space is reduced, it may be embedded within a larger reversible gate (bottom).

NOT

$$\begin{bmatrix} 0 & 1 \\ 1 & 0 \end{bmatrix}$$

CNOT

$$\begin{bmatrix} 1 & 0 & 0 & 0 \\ 0 & 1 & 0 & 0 \\ 0 & 0 & 0 & 1 \\ 0 & 0 & 1 & 0 \end{bmatrix}$$

CCNOT

$$\begin{bmatrix} 1 & 0 & 0 & 0 & 0 & 0 & 0 & 0 \\ 0 & 1 & 0 & 0 & 0 & 0 & 0 & 0 \\ 0 & 0 & 1 & 0 & 0 & 0 & 0 & 0 \\ 0 & 0 & 0 & 1 & 0 & 0 & 0 & 0 \\ 0 & 0 & 0 & 0 & 1 & 0 & 0 & 0 \\ 0 & 0 & 0 & 0 & 0 & 1 & 0 & 0 \\ 0 & 0 & 0 & 0 & 0 & 0 & 0 & 1 \\ 0 & 0 & 0 & 0 & 0 & 0 & 1 & 0 \end{bmatrix}$$

FIGURE 1.2: The three gates proposed by Toffoli as a universal set for reversible computation: The NOT, CNOT (Controlled-NOT), and CCNOT. Though the CCNOT gate is itself universal, the addition of the NOT and CNOT gates allow any reversible circuit to be implemented without redundant output bits.

After Bennett showed that all classical processes could be simulated by reversible circuits, people began to search for a standard universal set of reversible logic gates to achieve reversible classical computation. Just as classical logic gates evolved from considerations in sequential logic, so too did reversible logic gates evolve of out work in so-called *conservative logic*, notably by Fredkin and Toffoli [30]. Toffoli [31] gave the reversible version of the AND gate, shown in Figure 1.1, which is universal for reversible computation. This complements Fredkin's universal controlled-swap gate, and these gates are now named after their respective authors.

Additionally, Toffoli proposed a set of three primitive gates that are universal for reversible computation: NOT, CNOT, and CCNOT. Of course, the first two of these are special cases of the CCNOT gate, which is itself universal. Significantly, however, Toffoli found that the NOT, CNOT, and CCNOT gates together (see Figure 1.2) allow us to implement any reversible operation without redundant (or in Toffoli's words, *garbage*) output bits.

In light of these theoretical developments, it was quickly realised that the unitary

evolution of isolated quantum mechanical systems could provide a universal realisation of reversible logic, and in the 1980s there were a number of papers addressing the implementation of reversible computing with quantum mechanical Hamiltonians [32–40]. Feynman's *Quantum Mechanical Computers* [41] for example took the $\hat{\sigma}_X$ Pauli operator in place of the NOT gate, from which definitions equivalent to Toffoli's CNOT and CCNOT follow (see Figure 1.2).

1.2 Generalisation of Quantum Operations

The 1980s also saw the first inklings of the power of quantum mechanical systems to exceed classical ones. The earliest example is perhaps Feynman's famous recognition, in his 1982 lecture *Simulating physics with computers* [1], that quantum systems could potentially simulate other such systems with an exponential improvement in efficiency over their classical counterparts. Around the same time Wiesner published his 1983 paper *Conjugate Coding* [2], the ideas in which were later expanded upon in the quantum cryptographic scheme *BB84* [11]. We can think of the development of these cryptographic ideas as the extension of Toffoli's reversible gates by the addition of the Hadamard operator,

$$\hat{H} = \frac{1}{\sqrt{2}} \begin{bmatrix} 1 & 1 \\ 1 & -1 \end{bmatrix}. \tag{1.1}$$

The conjugate bases of a two-level quantum system could now be accessed and the measurement limitations exemplified by the well-known Stern-Gerlach experiment could now be exploited. The space of states in use here, however, remained the discrete set of four points at the extreme top, bottom, left, and right of a circular projection of the Bloch sphere: the full space of quantum states was not yet included.

The germ of the idea of quantum supremacy *begins* here: Wiesner's conjugate coding was an example of a quantum operation using conjugate bases that could not be reproduced classically, and Feynman's idea on simulation was an example of a calculation for which the resources of a quantum system seemed an exponential improvement. However, these two ideas had not yet been expressed in a manner that could bring them together and generalise them to algorithms beyond analogue quantum simulation. It was in this context that in 1985 Deutsch published his *Quantum Theory, the Church-Turing Principle and the Universal Quantum Computer* [3], in which he argued explicitly that computing with quantum mechanics is more general than with a classical Turing machine, which was itself a special case.

> *"The universal quantum computer Q has all the properties of [Turing's universal computing machine]. But Q admits a further class of programs which evolve computational basis states into linear superpositions of each other."*
>
> — Deutsch, Quantum Theory, the Church-Turing Principle and the Universal Quantum Computer, 1985 [3]

Deutsch suggested four ways in which the universal quantum computer surpassed the classical computer: true random number generation; quantum correlations (in the sense of Bell's theorem [42]); perfect simulation of arbitrary, finite physical systems; and parallel processing on a serial computer. This last point, *quantum parallelism*, would be the spark underlying the central algorithmic results of the

following decade, and in his 1985 paper Deutsch had provided a rough early predecessor to the *Deutsch–Jozsa algorithm* [43] for evaluating the parity of a two-valued function.

This initial claim was followed up by Deutsch with a full circuit representation for quantum logic in his 1989 paper *quantum computational networks* [4]. This quantum network description was a generalisation of the descriptions already in use for classical circuits, *"an acyclic directed graph in which nodes correspond to functions and arcs to variables"* [31]. The quantum case had a few characteristic restrictions worth noting, however. For example, the arcs corresponding to qubits (though the term *qubit* for the quantum analogue of a bit would not be coined until 1995 [44]) were not allowed to split, as the copying of arbitrary quantum information is not possible [45], and the function nodes were assumed to represent only unitary operations.

The second contribution of Deutsch in his 1989 paper was the first definition of a universal quantum logic gate,

$$\hat{D}(\theta)\,|a,b,c\rangle \rightarrow \begin{cases} \left(i\cos(\theta)+\sin(\theta)\hat{\sigma}_x^{(c)}\right) & |a,b,c\rangle\,, \quad (a\wedge b) \\ & |a,b,c\rangle\,, \quad \neg(a\wedge b), \end{cases} \tag{1.2}$$

now known as the *Deutsch gate*, where $\hat{\sigma}_x^{(c)}$, the Pauli-X operator on qubit c, is to be interpreted as *not* c. The Deutsch gate is a generalisation of the Toffoli 3-bit reversible AND gate, and reduces to it for $\theta = \pi/2$.

Though Deutsch had shown his quantum circuit description to be a universal representation of operations on quantum systems, he had not, in 1989, proven it to be an efficient description. If it was not efficient (and indeed, it was not), then it would not be clear that quantum algorithms expressed in this language provided an advantage over those of the classical Turing machine. This problem was solved for the pure-state case in 1993 in two stages; begun by Bernstein and Vazirani [46], the work was completed by Yao [47]. The generalisation to mixed states was provided later by Aharonov et al. [48], following an increased interest in decoherence and quantum error correction.

1.3 Quantum Algorithms

By the 1990s the idea of *quantum parallelism*, pioneered by Deutsch, was being investigated by other authors. The utility of this unique form of parallelism was not immediately apparent, however, as the measurement of a qubit state results in at most one bit of information. Jozsa, in 1991, characterised the collective properties of the output values of functions according to interference patterns derivable from a quantum superposition [49]. Soon afterward, in 1992, having in hand a concrete description of the kinds of (global) properties that could be efficiently extracted from a function by a quantum system, Deutsch and Jozsa then introduced the quantum Fourier transform and published their famous proof-of-principle algorithm: the determination of whether a function is *balanced* with only a single evaluation [43] (later refined in [50]). Following this, detailed discussion took place about how quantum computing should be incorporated into the hierarchy of computational complexity [46, 51–53]. Then, in 1994, Shor built on the approach of Simon [53] to invent an efficient quantum algorithm for the prime factorisation of integers [18]. Many quantum algorithms exist today [54], famously among them Grover's unstructured database search [19] and quantum annealing [55]. Yet, I think it is not an exaggeration to say that Shor's factoring algorithm, for its practical implications with respect to public

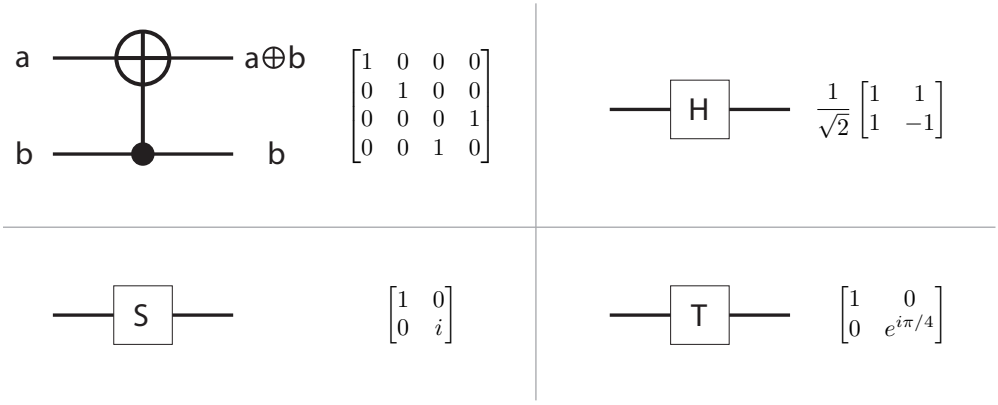

FIGURE 1.3: The four gates CNOT (left, top), Hadamard (right, top), Phase (left, bottom), and $\pi/8$ (right, bottom) are sufficient to generate any arbitrary quantum operation to predetermined accuracy.

key cryptography, has been the primary motivating force behind long-term technological development in this field.

1.4 Development of Universal Quantum Gate Sets

Following Shor's discovery in 1994 of a quantum algorithm with practical utility, development in quantum information processing takes a distinctly practical turn. From here, the development we will be interested in diverges into two main streams: quantum gate sets and quantum error correction, though the two eventually reunify. I begin here with quantum gate sets.

While the Deutsch gate [4] is universal, it is difficult to implement; most quantum mechanical interactions, as indicated by the matrix representation of the Hamiltonian, are at most bipartite. This could potentially have presented quite a practical challenge, as three-bit gates were known to be required for universality in classical reversible logic. Quantum logic, fortunately, turned out to differ in this regard, and in 1995 it was shown that two-qubit gates were universal for quantum computation [56–58]. This discovery began the search for efficient, realisable and universal two-qubit gate sets [59–61] and decompositions of the universal reversible logic gates [62–64]. For example, either the Toffoli gate or the Fredkin gate can be realised with *five* two-qubit gates [64]. A commonly-cited universal set of quantum gates is shown in Figure 1.3.

While Bennett et al. had shown in 1993 that a qubit can be projectively *teleported* at the cost one entangled bit (or *ebit*) [65], Gottesman and Chuang in 1999 made the significant observation that the phenomenon of quantum teleportation could be used to project *gates* onto quantum data using ancillae prepared in particular states [66, 67]. Quantum teleportation therefore provides an alternative standardised two-qubit gate, and this would later become one of the foundations of encoded, fault tolerant gates with magic state distillation [68] and of measurement-based quantum computation [69].

1.5 Quantum Error Correction

With Shor's 1994 factoring algorithm [18], quantum information processing had a clear motivating promise. In turning toward the fulfilment of this promise, however, researchers soon realised a fact that would become a (perhaps *the*) defining challenge for large-scale quantum information processing: despite its origins, quantum computing is *not* strictly reversible. The system cannot be perfectly isolated from its surrounding environment and the resulting interaction allows information to leak out into that environment, where it is lost for all practical purposes and introduces computational error. The significance of this environmental source of error and of cumulative systematic gate errors were formally identified in 1995 [70] and the error rate requirements for large-scale computation, in the absence of correction or stabilisation, were estimated [71–73].

Classically, simple data protection through redundancy had been in use for many centuries, and a formal theory of error correction [74] and fault-tolerant classical information processing [75] had developed alongside the rise of computers in the middle of the twentieth century. Two factors prevented their direct application to quantum information:

1. Measurement destroys information in conjugate bases, so that neither an unknown quantum state nor the individual qubits of an entangled multi-qubit state can be measured without *collapsing* that state. Simple majority-voting schemes could therefore not be directly applied.

2. An unknown quantum state cannot be copied [45], so that classical redundancy cannot be generated *ex post facto*.

The key to overcoming these two issues was identified late in 1994 [20–22], at the onset of popular interest in quantum error rates: The collective state of a set of qubits maximally entangled in a known basis, in the absence of error, can exist in a state of known symmetry. If error disturbs this symmetry, then measurement of the stabilising operators of its subspace (qubit parity-check operators) acts as an error-detecting operation. It is perhaps no surprise that Deutsch and Jozsa, the first people to exploit the utility of functional parity measurements in quantum algorithms, were among the authors who first proposed coherent parity measurements for the stabilisation of quantum states. Quantum error detection would go on to be used for the distillation of high-purity known states from multiple noisy copies [76, 77].

While error *detection* allows for the *post hoc* selection of high-purity states and can mitigate errors susceptible to the quantum Zeno effect [78], more general, memoryless forms of noise are not suppressed in this way. The first quantum error *correcting* code was proposed by Shor in 1995 [79] as a concatenated generalisation of the classical repetition code. This proposal relied upon the fact that the effect of general error on a state in a finite-dimensional Hilbert space can be expressed as the incoherent mixture of a finite set of operations. This is most apparent in the *Bloch vector* representation [80], and a quantum state can therefore be fully protected if it can be protected against the generators of this set: Classical error correction codes can be *nested* within one another to mitigate the noise associated with each generator. Shor's nine qubit code, now named for him, and its nested structure is shown diagrammatically in Figure 1.4.

The following years [81–92] saw a number of results on the identification of the criteria for a quantum error correction code, the discovery of efficient codes, the construction of efficiency bounds, and the discovery of constructions for quantum

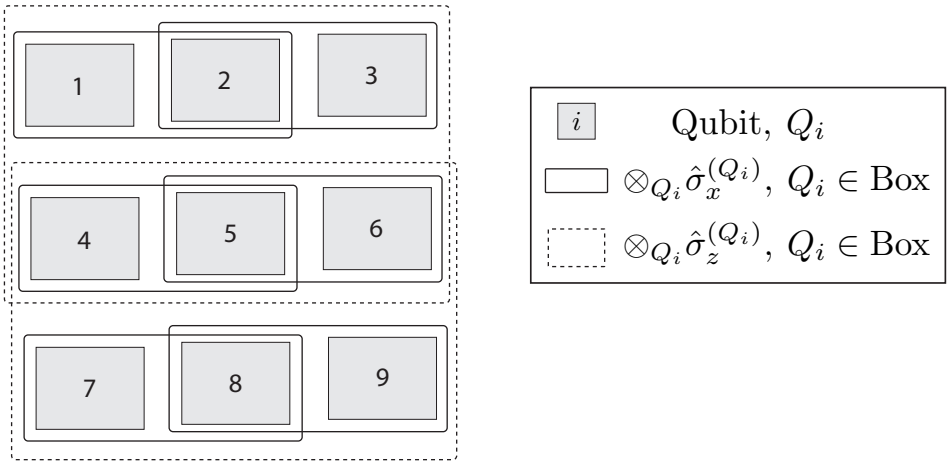

FIGURE 1.4: Shor's quantum error correction code consists of nine qubits and two sub-logical layers. At the first sub-logical layer, errors in the $\hat{\sigma}_z$ basis are mitigated by a classical repetition code of three qubits, with parity checks indicated here by solid boundaries. At the second logical layer, these partially-encoded, three-qubit subsystems are nested inside a second classical repetition code. Errors in the $\hat{\sigma}_x$ basis are mitigated by parity checks indicated here by dashed boundaries. Shor's code can locate and correct any single-qubit error, as well as certain multi-qubit errors at the first logical layer.

error correction codes from classical codes. The primary criterion considered during this period was the efficiency in terms of the number of redundant qubits used as compared with the number of qubits encoded and the number of single-qubit errors that could be simultaneously corrected. One key result was the identification of the very smallest code (of only five qubits) capable of correcting a single error [87, 93]. Nonetheless, the quantum error correction codes discussed above were proposed under the assumption that the operations of syndrome measurement and correction did not introduce a new source of error; they were strictly *storage* codes. If quantum error correction was to be used for computation, it would also need to mitigate the otherwise cumulative effects of faulty operations.

The result, formalised with the *threshold theorem* and the construction of fault-tolerant correction procedures [94–99], is that the error rate is now required to be small on the scale not of the total computation, but only of the parity-check subroutine. The specific requirement is expressed as a threshold error rate and varies with the encoding scheme. The error threshold is also called the *accuracy threshold*. From this point onward, due to the high error rates of real quantum systems, the accuracy threshold would become the primary factor in the comparative analysis of quantum error correction codes, in lieu of the degree of redundancy.

To date, the quantum error correction codes with the largest accuracy thresholds belong to the family of *topological* quantum error correction codes. These codes identify qubits and parity check measurements with the cells of a regular lattice. The first topological code was Kitaev's *toric code*, wherein qubits were identified with the edges of a periodic square lattice, and parity measurements in the X and Z bases with vertices and faces of this lattice respectively [100–102]. The toric code encodes two logical qubits at the cost of L^2 physical qubits, with an accuracy threshold (per correction round, and without measurement error) of about 11%. Here L is the *code distance*, the minimum number of single-qubit operations separating logical encoded states. The periodic structure of this code was recognised as a barrier to its adoption,

however, so it was soon adapted in a planar variant, the *surface code* [103–105], which encodes a single logical qubit in $L^2 + (L-1)^2$ physical qubits with an equivalent accuracy threshold. Error models have been refined since the early development of these codes, and the accuracy threshold per *quantum logic gate* in the presence of measurement error is estimated to be between 0.5% and 1% [106]. These remain the highest per-gate accuracy thresholds found to date for codes protecting against any single qubit quantum error. Operations must be achievable with error rates below these values before any known form of error correction can be implemented.

The theoretical developments of quantum information processing did not of course end with the discovery of topological error correction codes. For instance, protected and multiplexed schemes for quantum state transmission through lossy channels [107–110], the advent of measurement-based quantum computing [111,112], the abstract generalisation of quantum error correction codes [113–116] and the plurality of logical gate implementations [68, 117–119] represent only a fraction of the topics that could be discussed in a comprehensive review. However, we end our brief historical survey here because, from a near-term technological perspective, the essential challenges are those that were defined by the turn of the millenium and mentioned above.

1.6 Modern Challenges

What should we seek to achieve in the near-term? Sub-tasks in communication and quantum metrology have received a lot of attention as they have both seen the most practical success in the forms of medium-range ($\approx$ 200 km) quantum key distribution and (primarily) in-vivo biological imaging, field sensing and temperature sensing. Immediate targets for the implementation of quantum technologies are repeater-based quantum communication, sensing, and simulation, due to the low qubit and operation numbers involved.

The next significant development in quantum communication will likely be the use of single long-lived qubits as middleman storage in 3-point memory-assisted quantum key distribution, eventually working towards the first quantum repeaters encoded against (partial) errors. The developments for quantum metrology look as if they will be extensions of the recent results using relaxation-encoded states, and could also exploit entangled states and dynamical decoupling sequences to enhance measurements of high-frequency periodic processes.

Many physical systems, including ion-traps [120–130], superconducting circuits [131–140], quantum dots [141–149], linear optics [150–152], donor spins in silicon [153–160] and nitrogen–vacancy centers among other defects [161–171], have been proposed to realize such technologies. Key experiments have been performed demonstrating basic required operations [172–178], and small-scale applications have also been demonstrated [179–181]. It remains challenging to realize two-qubit gates and projective measurements with sufficient accuracy in most physical systems.

Yet, we should keep in mind the potential of any scheme to serve as a stepping stone toward large-scale quantum computation. Many technologies are coherence limited; quantum error correction, if only partial correction at first, will be a central component of quantum technologies of any moderate scale. Quantum error correction demands that unitary operations and projective measurements achieve operational error rates less than a code-dependent *accuracy threshold*. For instance

the *surface code* [103–105] has a conservative accuracy threshold of 0.54% [106]). Resource overheads necessitate an error rate significantly below the accuracy threshold, suggesting the practical requirement that the operational fidelity be $> 99.9\%$. These requirements may be lower for quantum communication schemes with limited maximum distances. Topological codes such as the surface code promise to be the easiest to implement in the near future, as multi-qubit systems are also commonly limited by local and operational noise to short error correction protocols. We address the mitigation of these noise sources in Part I.

Part I

Local Noise in Near-Term Applications

Chapter 2

Robust quantum sensing with strongly interacting probe systems

Physical quantities are the guideposts that we use to navigate through life, and the drive toward cheaper, faster, more accurate devices for their measurement has a direct commercial impact through increased productivity and efficiency. The field of quantum metrology [14], and more specifically here quantum sensing [16], promises refinements over existing technologies in two key respects: Firstly, direct control over coherent systems at the nano-scale promises an enhanced spatial resolution, as well as measurement *in vivo* without adverse effects to the host system; secondly, the presence of coherent, quantum correlations and entanglement promise to achieve sample variances dependent, not linearly in the sample size as is characteristic of a classical statistical sample, but with a form approaching a quadratic dependence. This improved scaling is said to approach the *Heisenberg limit*, in contrast to the classical *standard quantum limit*. As mentioned in Section 1.6, quantum sensing is a potential near-term application on account of its low qubit number and restricted operation set.

Quantum sensing devices have been proposed most famously for thermometry, magnetometry [182–184], and frequency estimation (timing) [185]. In this work we focus on quantum sensing with a set of N spin-1/2 systems maximally entangled in a Greenberger-Horne-Zeilinger (GHZ) state [186], as

$$|\mathrm{GHZ}\rangle = \frac{1}{\sqrt{2}}\left(|0\rangle^{\otimes N} + |1\rangle^{\otimes N}\right). \tag{2.1}$$

More specifically, we seek to estimate the mean free energy, ω_μ, of this set of spins, according to their evolution under the Hamiltonian

$$\hat{H}_{\mathrm{Sys}} = \frac{\hbar}{2}\sum_{i=1}^{N}\omega_i\hat{\sigma}_z^{(i)} - \frac{\hbar}{4}\sum_{i=1,j\neq i}^{N} g_{ij}\hat{\sigma}_z^{(i)}\otimes\hat{\sigma}_z^{(j)}, \tag{2.2}$$

$$\omega_\mu := \frac{1}{N}\sum_{i=1}^{N}\omega_i, \tag{2.3}$$

$$G_i := \sum_{j=1,j\neq i}^{N} g_{ij}. \tag{2.4}$$

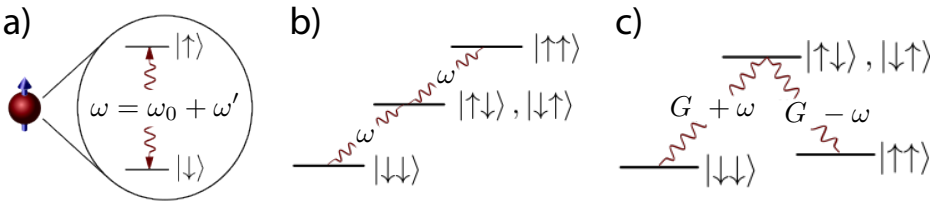

FIGURE 2.1: Energy level structure for **a)** a single spin-1/2 system, with an energy gap ω deviating by a small amount ω' from a known calibration energy ω_0; **b)** two spin-1/2 systems without interaction, under the assumption of equal energy gaps; and **c)** two spin-1/2 systems under strong ferromagnetic coupling with an amplitude $G > \omega$. While in case (b) relaxation to a single insensitive ground state can occur even at zero temperature, case (c) identifies the most sensitive probe states with local ground states to extend the lifetime of the system.

Here ω_i is the free energy of spin i, g_{ij} is the spin-spin coupling between particles i and j, and $\hat{\sigma}_z^{(i)}$ is the operator corresponding to the application of the Pauli z-matrix,

$$\sigma_z = \begin{bmatrix} 1 & 0 \\ 0 & -1 \end{bmatrix}, \tag{2.5}$$

to spin i. We have also defined a collective coupling for spin i, G_i, and the mean free energy of the total spin system, ω_μ. This mean free energy ω_μ, or rather its deviation from a lower-precision calibration point ω_0, can then be related to other physical parameters of interest, such as an axial magnetic field or temperature, through their respective susceptibilities. A coupling term has been introduced to engineer the energy level structure of the composite spin system, with the goal of locating the most sensitive probe states at localised ground states with respect to anticipated spin relaxation [187–197] and thereby reducing the spin number and measurement time resources. While the free energy term in Equation (2.2) is intended to describe the effect of an external field along an arbitrarily selected axis, it is important that the coupling term is aligned with this axis so that the stationary states of the system are preserved. An illustration of this is given in Figure 2.1.

In summary, it is known that entanglement can enhance sensing efficiency, but that this effect is lost in the presence of a memoriless noisy environment. Active correction schemes are known to show reduced effectiveness in the presence of asymmetric relaxation, and cannot improve the T_1 times of individual spins. It is also known that large energy gaps exponentially suppress excitation, forming a passive noise barrier. With these points in mind we would like to answer the following question: How can we create such a passive barrier and under what conditions will it improve sensing performance?

2.1 Quantifying Measurement Performance

Intuitively, the performance of a measurement is related to the difference between the inferred and the true probability distributions governing the measurement outcomes. In quantum sensing, this difference is quantified at the level of differential geometry by the *Fisher information* and through it the *sensitivity* of the measurement. We now take a brief pedagogical detour to explain these terms, summarising loosely the formulation in [198].

The *relative entropy* was introduced in the mid-twentieth century by Kullback and Leibler [199] and by Jeffreys [200] as an asymmetric measure of the distinguishability between two probability distributions. It can be thought of as a slight generalisation of the Shannon entropy [201], becoming

$$S(P||Q) = \sum_{i=1}^{K} p_i \ln\left(\frac{p_i}{q_i}\right), \tag{2.6}$$

where here we assume a discrete set of outcomes labelled $1 \to K$. p_i denotes the probability of each outcome for distribution P, while q_i denotes the probability of each equivalent outcome for distribution Q.

Sanov's theorem [202], valid for large sample sizes M, allows us to interpret the relative entropy as the decay rate of the probability of inferring a sample distribution P_{Sample} if the true distribution is Q,

$$\text{Prob}(P_{\text{Sample}}|Q) \sim e^{-M \cdot S(P_{\text{Sample}}||Q)}. \tag{2.7}$$

The Fisher information matrix $F_{ij}(Q)$, or the *Fisher-Rao metric*, is the metric defining the relative entropy between two infinitesimally close probability distributions, or equivalently the Hessian matrix of the Shannon entropy for the true probability distribution. Note that the relative entropy becomes a symmetric measure in this limit. The Fisher information therefore describes, under the Sanov interpretation, the decay rate of the probability to infer a sample distribution other than the true distribution, as

$$\text{Prob}(P_{\text{Sample}} \neq Q) \sim e^{-M \cdot S(Q+\delta Q||Q)} \tag{2.8}$$

$$= e^{-M \sum_{i,j} \delta Q_i F_{ij}(Q) \delta Q_j} \tag{2.9}$$

$$= e^{-M \cdot \delta Q^2 \cdot F(Q)} \text{ for a one-dimensional distribution.} \tag{2.10}$$

The notion of an estimate being precision-limited by the Fisher information was formalised in the Cramér-Rao bound [203, 204],

$$M \cdot \Delta P^2_{\text{Sample}} \cdot F(Q) \geq 1, \tag{2.11}$$

where $\Delta P^2_{\text{Sample}}$ is the variance of the sampled distribution.

While a quantum generalisation of the Fisher information metric has been developed [205], the simple measurements considered in this section will not require it: The measurement we consider reduces, after evolution of the quantum state, to a simple Bernoulli trial for which the classical Fisher information is sufficient.

Simple Bernoulli trials are known to saturate the Cramér-Rao bound. However, we are interested not in the trial success probability, but rather in an underlying parameter, the mean free-energy ω_μ. The dependence of the probability distribution on this parameter may be curved, so that the bound with respect to this underlying parameter is saturated only in the limit of a large sample size, for which $\Delta P^2_{\text{Sample}}/\Delta\omega^2_\mu \to (\partial P_{\text{Sample}}/\partial\omega_\mu)^2$.

In the final analysis, we have

$$F = \frac{\left(\frac{\partial p}{\partial \omega_\mu}\right)^2}{p(1-p)}, \tag{2.12}$$

so that

$$\Delta\omega_\mu^2 \geq \frac{p(1-p)}{M\left(\frac{\partial p}{\partial \omega_\mu}\right)^2}. \tag{2.13}$$

Given this, the *sensitivity* is defined as the inverse of the product between the total sensing time, T, and the variance of the inferred parameter,

$$S := \frac{1}{\Delta\omega_\mu^2 \cdot T} \tag{2.14}$$

$$\to \frac{M \cdot F}{T}, \text{ in the large } M \text{ limit.} \tag{2.15}$$

When a set of M successive, independent measurements are performed, the total sensing time T can be expressed as a multiple of the characteristic time for a single trial t, as $T = Mt$. This number can therefore be eliminated from the sensitivity, so that we have

$$S \to \frac{F}{t}. \tag{2.16}$$

2.2 GHZ Sensing

2.2.1 Ideal Conditions

Under noiseless evolution, the initial state accumulates a relative phase dependent on the evolution time, t, and the mean free energy of the set of N spin-1/2 systems, ω_μ, as

$$|\text{GHZ}\rangle \to \frac{1}{\sqrt{2}}\left(|0\rangle^{\otimes N} + e^{iN\omega_\mu t}\,|1\rangle^{\otimes N}\right) \tag{2.17}$$

up to a global phase. The interaction term in Hamiltonian Equation (2.2) contributes only a global phase under ideal conditions.

Measurement along an axis in the X/Y plane of the collective Bloch sphere, with the angle of deviation from the X-axis governed by the expected evolution under a lower-precision calibration frequency ω_0, and chosen to linearise the infinitessimal dependence of the outcome probability on $\omega' := \omega_\mu - \omega_0$, then results in a binary measurement outcome (a Bernoulli trial). The success probability of this trial is given by

$$p_{\text{Success}} = \frac{1}{2} + \frac{1}{2}\sin\left(N \cdot \omega' \cdot t\right) \tag{2.18}$$

$$\approx \frac{1}{2}\left(1 + N \cdot \omega' \cdot t\right). \tag{2.19}$$

The Fisher information and sensitivity are then simply calculated to be

$$F = \left.\frac{\left(\frac{\partial p_{\text{Success}}}{\partial \omega'}\right)^2}{p_{\text{Success}}(1 - p_{\text{Success}})}\right|_{\omega' \to 0} = (Nt)^2, \tag{2.20}$$

and

$$S = \frac{F}{t} = N^2 t, \tag{2.21}$$

saturating the Heisenberg limit.

2.2.2 The Effect of Noise

In contrast to the well-known result above, real systems are neither perfectly isolated, nor perfectly controlled. We consider the effects of noise here by allowing the system to interact with a thermal harmonic oscillator environment, and, under the Born, Markov, and rotating wave approximations, the resulting evolution [206, 207] of the projective measurement's expectation value corresponds to a Bernoulli trial probability of

$$p_{\text{Success}} = \frac{1}{2} + \frac{1}{2}\sin\left(N \cdot \omega' \cdot t\right) e^{\frac{-N\Gamma t}{2}} \tag{2.22}$$

$$\approx \frac{1}{2}\left(1 + N \cdot \omega' \cdot t e^{\frac{-N\Gamma t}{2}}\right). \tag{2.23}$$

Here Γ is a decay rate averaged over all spin-1/2 systems, $\frac{1}{N}\sum_i \Gamma_i$, where the Γ_i follow the typical form of rate coefficients in a Linblad-type master equation approximating interaction with a harmonic-oscillator environment ($\omega_i > 0$),

$$\Gamma_i = \Omega\left(|G_i \pm \omega_i|\right)\left(2\bar{n}_i + H\left(G_i + \omega_i\right) - H\left(G_i - \omega_i\right) + H\left(-G_i - \omega_i\right)\right). \tag{2.24}$$

$H(\cdot)$ is the Heaviside step function and $\bar{n}_i$ is the mean photon occupation number for the energy gap separating the ground and first excited states of the spin-1/2 system, while $\Omega\left(|G_i \pm \omega_i|\right)$ is a (potentially) frequency-dependent coupling rate reflecting the spectral density of the perceived environment. The basis of the advantage found in this chapter will be the diminution of $\bar{n}_i$ by increasing G_i.

Under the effect of this noise, the Fisher information and sensitivity become

$$F = (Nt)^2 e^{-N\Gamma t} \tag{2.25}$$

and

$$S = N^2 t e^{-N\Gamma t}. \tag{2.26}$$

We maximise this sensitivity by taking the simple derivative, finding

$$\frac{\partial S}{\partial t} = N^2\left(1 - N\Gamma t\right) e^{-N\Gamma t}, \tag{2.27}$$

$$\Rightarrow t_{opt} = \frac{1}{N\Gamma} \tag{2.28}$$

$$S_{opt} = \frac{N}{e\Gamma}. \tag{2.29}$$

For fixed Γ this sensitivity does not reach the Heisenberg limit, but remains at the linear N-scaling of the standard quantum limit.

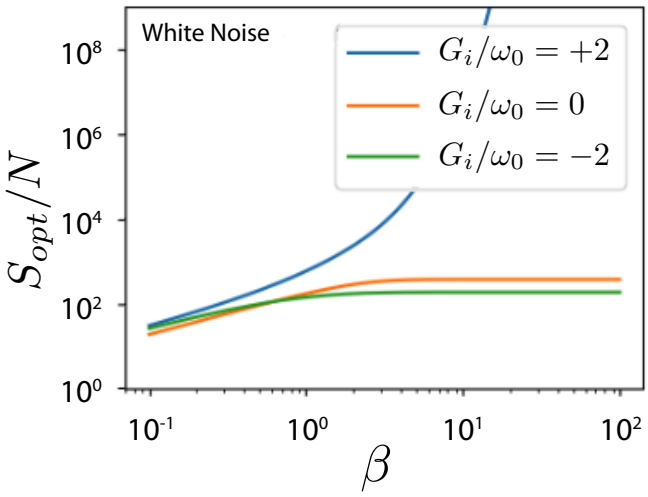

FIGURE 2.2: The scaled optimal sensitivity S_{opt}/N as a function of the inverse temperature β for a constant spectral density $\Omega = 0.001$ (white noise) and *collective coupling – to – approximate free energy* ratios of $+2$ (blue), 0 (orange) and -2 (green). Dominant scaling for strong ferromagnetic coupling (blue) is exponential with a regime change at approximately $\beta = 3$ while both other regimes saturate at $S_{opt}/N \sim 300$.

2.3 Temperature and Coupling Strength

We established in Subsection 2.2.2 that the optimal sensitivity depends linearly on the number of spins N and inversely on the decay rates Γ_i of Equation (2.24). These decay rates depend on the energy gap between the ground and first excited states of the collective spin system in three ways: firstly, the coupling to the environment Ω follows an as-yet unspecified spectral density function; secondly, the mean photon occupation number, assuming a thermal environment, depends exponentially on the ratio between this energy gap and the temperature; and thirdly, the relative magnitudes between G_i and ω_i will determine the values of the Heaviside functions in Equation (2.24), according to whether the system is in the weak, strong anti-ferromagnetic, or strong ferromagnetic coupling regime.

Figure 2.2 shows S_{opt}/N as a function of the inverse temperature $\beta = 1/k_B T_{env}$, where k_B is Boltzmann's constant and T_{env} is the temperature. The spectral density is chosen arbitrarily as the constant value $\Omega = 0.001$. An increasing value of S_{opt}/N indicates an improvement over the standard quantum limit. Even at low temperatures, the decay rates for the weak coupling and strong anti-ferromagnetic coupling regimes saturate at $\Gamma_i \sim \Omega$, giving $S_{opt}/N \sim 300$. For strong ferromagnetic coupling the optimal sensitivity increases exponentially according to Arrhenius' Law $1/\Gamma \sim e^{-\beta \cdot \Delta E}$ [192]; two stages appear corresponding to the two energy gaps $G_i \pm \omega_0$ represented in Figure 2.1. As it is our objective to approach the Heisenberg limit, our focus for the remainder of this section will be the regime of strong ferromagnetic coupling.

2.4 An Example

We now consider a concrete example. Recent experiments have used dynamical decoupling to extend the T_2 time in superconducting flux qubits to the $T_2 \leq 2T_1$ limit

[208–210], while others have demonstrated strong, ferromagnetic coupling between superconducting flux qubits [211–213]. These are the two requirements necessary for the implementation of our proposal, though they have not yet been demonstrated simultaneously.

Assuming an environment temperature of $T_{env} = 20$ mK and uniform coupling rates G_i between all spin pairs, we compare four cases in Table 2.1. The first two rows constitute the base cases against which we compare the last two, and demonstrate through the scaled sensitivity the conclusion of Equation (2.29) that without the coupling term the system operates at the standard quantum limit. The final two rows, in addition to displaying a sensitivity enhancement over the zero-coupling case due to reduced decay, also display a change in the scaled sensitivity relative to one another; the strong coupling of the final two rows allows us to overcome the standard quantum limit.

There are two important factors contributing to the scaled sensitivities in Table 2.1: the relaxation time T_1 and the thermal mean photon occupation number. These are both influenced by the energy gap $|G_i \pm \omega|$, which is in turn affected by the number of spins, N. We note that the sharp decrease in relaxation time for the final row of Table 2.1 is an idiosyncrasy of the particular system considered; the dominant form of environmental noise changes from $1/f$ noise to a combination of Ohmic and other forms of noise at higher frequencies [210]. It is *in spite* of this change that the sensitivity enhancement observed in the final row of this table is achieved.

TABLE 2.1: Estimated sensitivities for superconducting circuits, varying the T_1 time, the free energy ω_0, the collective coupling G_i, and the number of qubits N.

T_1 (μs)	ω_0 (GHz)	$G_i/(N-1)$ (GHz)	N	S_{opt}/N (s)
30	5	0	2	3.5×10^{-6}
30	5	0	4	3.5×10^{-6}
20	2	5	2	5.5×10^{-6}
2	2	5	4	35×10^{-6}

In the final subsections we describe the influence of the qualitative behavioural differences under different spectral noise profiles and of the spin number on the coupling strength for short-range interactions.

2.5 Noise Spectra

We noted in Section 2.4 that for the superconducting flux qubits considered the form of the environmental spectral density changes with the energy gap between the ground and first excited states, from $\Omega \sim \Delta E^{-1}$ to $\Omega \sim \Delta E^{+1}$. In the limit $G_i \gg \omega_0$, the improvement observed in Figure 2.2 should still be present, as the dependence on $\bar{n}_i$ of this energy gap dominates the low-order scaling of coupling to the environment. For $G_i - \omega_0 \to 0_+$, however, sub-Ohmic environmental spectra, with terms that scale sub-linearly in the energy gap, will either cause a divergence in and of themselves or will allow the mean photon occupation number $\bar{n}_i$ to diverge, as

$$\lim_{G_i - \omega_0 \to 0_+} \Omega \cdot \bar{n}_i = \frac{\Omega\left(|G_i - \omega_0|\right)}{\hbar\beta\,|G_i - \omega_0|}. \tag{2.30}$$

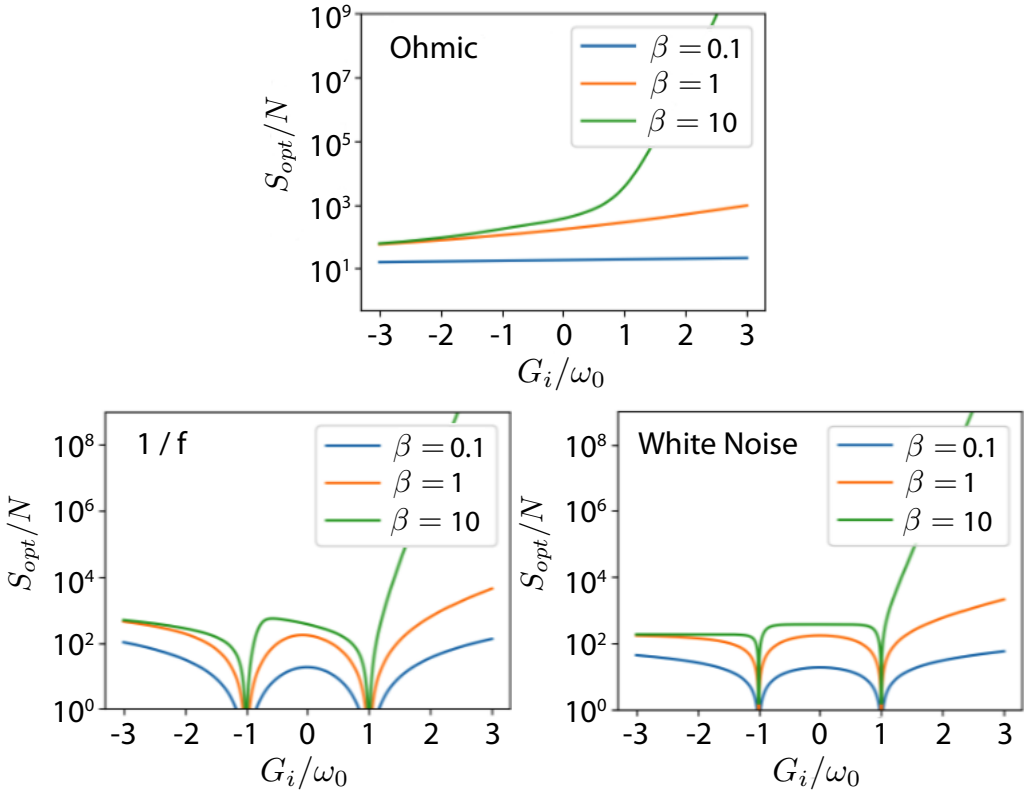

FIGURE 2.3: Rescaled optimal single-trial sensitivity S_{opt}/N as a function of the *relative* collective coupling strength G_i/ω_0 for **(Top)** an Ohmic noise profile, **(Left, Bottom)** a $1/f$ noise profile, and **(Right, Bottom)** a white noise profile. Three sample inverse temperatures, $\beta = 0.1, 1.0$, and 10.0 are shown. While the sensitivity increases monotonically for the Ohmic noise profile, it displays a sharp decrease near the divergences of the $1/f$ and white noise profiles at unit relative coupling strength.

This behaviour is shown in Figure 2.3 for linear (Ohmic), constant (white noise), and inverse ($1/f$ noise) scaling respectively. While the advantage found for the Ohmic spectral density increases monotonically with $|G_i - \omega_0|$, the aforementioned divergence of the white noise and $1/f$ spectra reduces the optimal sensitivity; a threshold value must be reached for the collective coupling before an advantage is found.

2.6 Short-Range Interactions

We have been speaking so far about a collective coupling G_i, but have not made mention of the dependence of this parameter on the pairwise spin-spin couplings g_{ij} from Equation (2.2) that comprise it. While in the ideal case of a uniform interaction the collective coupling increases steadily with the number of spins, in reality these pairwise coupling rates are likely to be distance dependent. A distance dependence in the pairwise coupling rates is significant because it indicates a potential saturation of the average decay rate Γ in the spin number, as additional new qubits are too far to significantly contribute to the collective coupling G_i of the old.

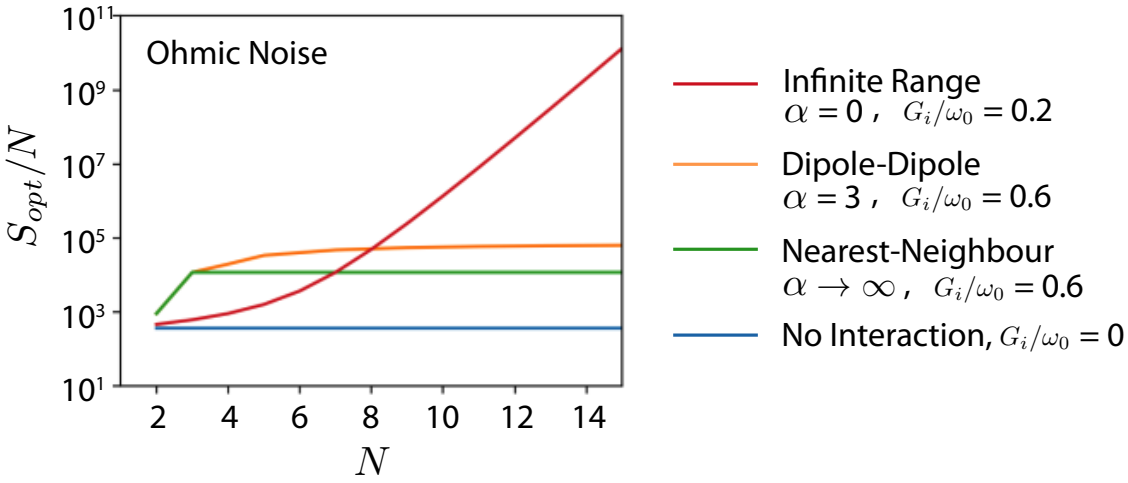

FIGURE 2.4: The rescaled optimal single-trial sensitivity S_{opt}/N as a function of the number of spin-1/2 systems, for an Ohmic noise profile. Four interaction types are shown: **(Blue)** No interaction; **(Green)** nearest-neighbour interactions; **(Orange)** interactions with the distance scaling of dipole-dipole coupling; and **(Red)** infinite-range, uniform interactions. The relative coupling term G_i/ω_0 has been reduced for the infinite range case so that its curvature is visible on the scale of the graph. A saturation of the scaled sensitivity is observed for all but the infinite-range interactions.

In Figure 2.4 we demonstrate this effect by considering pairwise couplings for a periodic, one-dimensional spin chain of the form

$$g_{ij} \sim \frac{1}{|i-j|^{\alpha}}, \tag{2.31}$$

where the subtraction is understood to be modulo the length of the chain for the case of no interaction ($g_{ij} = 0$), infinite-range uniform interaction ($\alpha = 0$), a dipole-dipole coupling interaction ($\alpha = 3$), and nearest neighbour interactions ($\alpha \to \infty$). We find that for short-range coupling the sensitivity rapidly saturates at $N = 3$ for nearest-neighbour interactions and at *about* $N = 7$ for dipole-dipole interactions respectively. The sensitivity continues an unbounded exponential increase with N for the case of uniform coupling.

Beyond the saturation point, adding additional qubits to the entangled probe state will continue to decrease the single-trial optimal sensing time of Equation (2.29), t_{opt}, but the increase in sensitivity will not exceed the standard quantum limit and any application-dependent advantage gained thereby must be considered in light of the progressive difficulty of constructing larger entangled states.

It is a curious observation that the sensitivity for the uniform interaction should increase exponentially with N when the Heisenberg limit appears to suggest a restriction to at most quadratic scaling. In fact, however, there is no contradiction: The Heisenberg limit is quoted $S \sim N^2$ on the assumption that the sensing time t_{opt} is independent of N. Any scheme for which t_{opt} may increase with N contains the potential for super-quadratic scaling.

2.7 Discussion

Recent proposals have shown that error correction schemes can, in principle, improve the sensitivity of a quantum sensor when the limiting noise process is orthogonal to the basis of interaction of the probe field [214–217]. However, even combined with dynamical decoupling [218] in the presence of an AC field, such schemes cannot be used to extend the bound imposed on the coherence time by the $T_2 \leq 2T_1$ limit, because they do not change the T_1 time of the individual physical qubits. Further, their improvement is limited when the noise process is energy relaxation [214, 219].

The passive method presented in this work, exploiting strong coupling to engineer a stable collective ground space, overcomes both of the limitations of active error correction schemes: Firstly, the π-pulses of dynamical decoupling commute with the two-qubit interaction terms and the T_1 times of the individual spins improve, not only the coherence time of the system as a whole — these being related to the Γ_i of Equation (2.24); secondly, since the probe states are local energy ground states the asymmetric relaxation behaviour of the assumed noise process only improves the performance. We have also shown a concrete example, in superconducting flux qubits, where this proposal could be implemented in the near-term to the benefit of T_1-limited applications in quantum metrology.

Not all systems can generate large, strongly coupled clusters; even where this is possible, any application requiring cluster-to-cluster interactions will introduce operational error for which active correction schemes again become necessary. It is in our interest therefore to look also at how the performance of these active schemes can be improved. This we consider in Chapter 3.

Chapter 3

Decoding Quantum Error Correction Codes with Local Variation

It has long been known that quantum information processing devices at any significant scale will face the obstacles of mounting noise and error [70–73]. Quantum error correction codes [220–222] were developed to overcome these obstacles, at the cost of increased qubit and time overheads. Even for smaller devices in the near-term, partially error-corrected approaches have been proposed to mitigate limiting noise processes [214–217]. Present devices face tight resource restrictions and error rates comparable to even the largest accuracy thresholds, so it is not (yet) sufficient to treat quantum error correction schemes as if their choice was agnostic with respect to the underlying technology or application: we must consider all idiosyncrasies and constraints before us. The constraints of most physical systems mean that the family of topological quantum error correction codes seems most promising for any near- to mid-term development, having three characteristic advantages: large accuracy thresholds, small correction circuits, and local interactions. The surface code [103–105], for example, requires only nearest-neighbour interactions. Conversely, many codes without such local constraints, such as Shor's code [79] and other concatenated codes [95], are simply out of reach for many real physical systems.

Just as the form of interaction varies according to our choice of physical system, so too does the form of the noise and error we confront; the very earliest proposals for quantum error correction in fact relied on error *detection* schemes [20–22, 223], under the assumption that the error of the state was subject to the quantum Zeno effect [78]. Standard models did eventually settle on the *depolarising noise channel* [87], but even then parallel streams of development emerged to deal with quantum channels for which depolarising noise was insufficient, such as loss channels [107]. In the last decade we have seen a plethora of results looking at different noise models, verifying the performance of the codes under such models and asking what modifications, if any, might be made to improve performance. Early examples focussed on the tendency for errors to be highly *biased* toward one particular basis (such as dephasing) [224–226]. Since then investigations of qubit loss [227–231], amplitude damping [232,233], correlated error [234–239], and qubit leakage [240,241] have been undertaken.

In this work we focus not on qualitatively distinct channel behaviour, such as loss or amplitude damping, but on local variation in a standard depolarising noise channel. Specifically, we assume that the measurement outcomes associated with each stabiliser operation are asymmetric with respect to their information content. This variability will not be the result of any changing external influence, but inherent in the information content associated with the measurement outcomes themselves.

Any multi-shot measurement scheme in the presence of error is expected to display such local variation, and in particular the cavity-enhanced spin measurements considered in Chapter 4 are expected to roughly follow an exponential distribution at the local level. We perform pseudo-threshold simulations for the repetition and surface codes, comparing the standard, fixed-error-rate case with an error-rate drawn from a discrete, balanced, two-component distribution of equal mean p_μ but a fixed relative width σ,

$$D(x; p_\mu, \sigma) = \frac{\delta\left[x - p_\mu(1-\sigma)\right] + \delta\left[x - p_\mu(1+\sigma)\right]}{2}. \tag{3.1}$$

We also introduce two approximate measures consistent with the simulated results to extrapolate the significance of variation for larger codes and higher dimensions. In Section 3.1 we describe and justify the approximate measures we introduce. Section 3.2 then defines and takes the repetition code as an exemplar of the significance of local variation for increasing code distance, while Section 3.3 extends the analysis to the surface code for comparative inference about the behaviour of codes in higher dimensions. In Section 3.4 we summarise our results and discuss a potential generalisation for alternative decoding schemes before concluding.

To summarise, it is known that the performance thresholds of quantum error correction codes are difficult to meet, and that close to these thresholds, resource requirements are steep. Noise and error processes vary, introducing idiosynchrasies like correlation and bias, and many such effects have been studied. The rate of error itself is often drawn from a known prior distribution at runtime, though consequent local variability is not represented in theoretical quantum error correction models. With these points in mind, we would like to answer the following question: In the simplest case of measurement error with local information, what performance benefits are obtained and under what conditions?

3.1 Quantifying Significance

Our aim will be to investigate the impact of σ on the error rate as a function of the code size and structure. This will be quantified in two ways: Firstly, numerical pseudo-threshold simulations will be performed for the repetition and surface codes, allowing us to compare the *logical error rate* between these two codes and across a range of code distances and local error rates. Secondly, we develop an intuition for the observed numerical behaviour with approximate models; we model the probability that local variance allows an error chain of length $\lfloor \frac{L}{2} \rfloor$ to be less likely than an error chain of length $\lfloor \frac{L}{2} \rfloor + 1$, where L is the code distance.

We consider chains of adjacent lengths because we are interested in the transition point at which local information becomes useful. Additionally, modifications to chains within a homology class — chains resulting in the same logical state — are of at least second order in the link probability. The intuition is that the exponential suppression of a chain's probability with length means that local information will have the most impact when two options are close to one another in length, so that this relationship is a qualitative proxy for the proportion of logical errors that the local information can help us identify and correct.

A chain's length is modelled as a number of successful Bernoulli trials, since a chain need not be contiguous along a given dimension of the lattice to cause a logical error. A binomial distribution approaches a Gaussian distribution for large L; we expect chains of length $\lfloor \frac{L}{2} \rfloor$ will have a lesser share of the tail of this distribution if

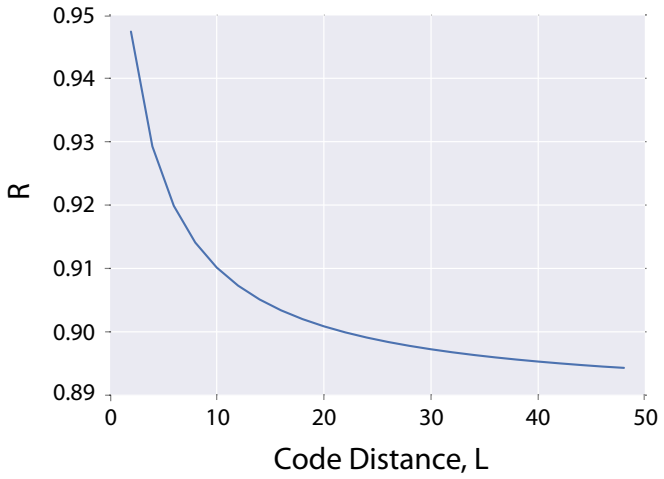

FIGURE 3.1: The fraction of logical errors caused by error chains of length $L/2$ for a one-dimensional lattice, R (Equation (3.2)), as a function of the code distance L. The individual error rate is fixed arbitrarily at $p_\mu = 0.1$.

they are far above the mean number of errors $Q \cdot p_\mu$, where Q is the total number of qubits and p_μ is the mean error rate per qubit. As the code distance increases local information should have a lesser impact on the logical error rate, so that our approximate measure is more valid for small code distances. Along a single dimension, we can justify this assertion by explicitly computing the ratio R,

$$R = \frac{\frac{L!}{(L/2)!^2}\left[p_\mu(1-p_\mu)\right]^{L/2}}{1-\sum_{i=\frac{L}{2}}^{L}\binom{L}{i}p_\mu^i(1-p_\mu)^{L-i}}. \tag{3.2}$$

This is the probability of sampling an error chain of length $L/2$ from L qubits via a binomial distribution, divided by the probability of sampling an error chain greater than or equal to $L/2$. The behaviour of this ratio with increasing L and fixed $p_\mu = 0.1$ is shown in Figure 3.1. Over the range of code distances considered in this report, our approximate measure should correspond well to true behaviour.

3.2 The Repetition Code and Chain Length

The repetition code, depicted in Figure 3.2, is defined by mapping qubit subsystems and operations to a $1 \times L$ chain. It is essentially a classical code, but may nonetheless be used to partially protect quantum information and is useful when the limiting source of error is highly biased along a single dimension. The repetition code embeds one bit of information within the $+1$ eigenspace of parity operators acting on adjacent bits in this 1-dimensional chain,

$$\hat{S}_X(v) = \otimes_{e|v\in\partial e}\hat{\sigma}_x^{(e)}. \tag{3.3}$$

Here v are vertices and e are edges. Vertices of degree-1 are excluded. Equation (3.3) uses a common shorthand notation for operators that are sparse with respect to the

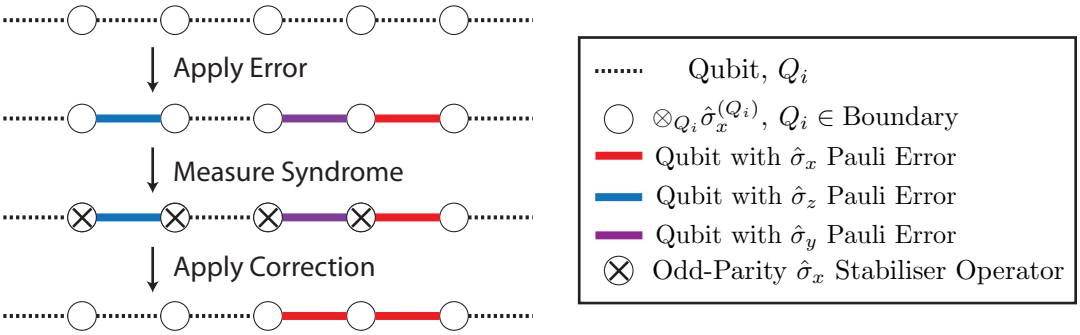

FIGURE 3.2: A graphical representation of the repetition code. Edges represent qubits, while nodes represent $\hat{\sigma}_x^{(i)}\hat{\sigma}_x^{(i+1)}$ parity (stabiliser) operations between adjacent qubits. Errors in a basis orthogonal to the parity operations are detectable.

set of qubit subsystems, ignoring the order of, and trivial elements in, the tensor product in favour of superscript indices.

A single local operation on any bit in the basis protected by the code (the basis orthogonal to the parity check operators) will be detected by measurement of the parity operators and may be corrected so long as the number of such errors is less than half the length of the chain. Measurement errors are incorporated by repeating parity measurements, with the effect of extending the lattice of the code into a second dimension [94,105]. The probability that accumulated error after the total set of such measurement rounds cannot be corrected is called the *logical error rate*. We restrict our attention to the phenomenological error model for the duration of this report; in this model individual qubit and measurement error rates are defined *per round* and associated with lattice edges.

3.2.1 The Impact of Local Variance

The variance in the total weight of a sampled error chain, as its length increases, depends upon the assumed local distribution. It is not the absolute variance that is important, since this will be suppressed for longer chains, but rather the variance relative to the chains' mean weight; the variance must offset the effect of the additional multiplicative factor associated with incrementing the length of the chain.

For the approximate measure of significance defined in Section 3.1, we will look at two distributions: the uniform distribution,

$$U(x \in [a,b]; a, b) = \frac{1}{b-a}, \tag{3.4}$$

and the discrete, balanced, two-component distribution,

$$D(x; a, b) = \frac{\delta(x-a) + \delta(x-b)}{2}. \tag{3.5}$$

We calculate the ratio between the standard deviation of the weight of a chain of length $L/2$ and the difference between the mean probabilities of chains of lengths $L/2$ and $L/2+1$. The resultant product distributions are not normally distributed, so the standard deviation provides only a rough characterisation of the width. Without analytic formulae for the sample-product distributions, we compute the considered ratio numerically via random sampling. The results are shown in Figure 3.3,

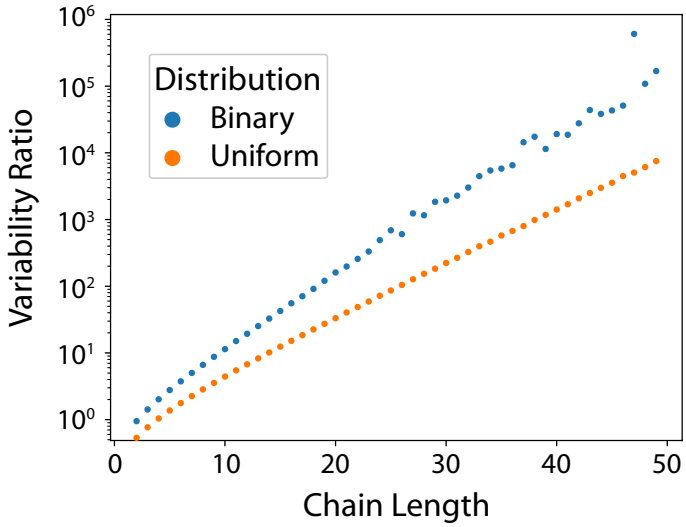

FIGURE 3.3: The ratio between the standard deviation of a product distribution associated with a chain of length L and the mean difference in probabilities between chains of lengths L and $L+1$, plotted as a function of the length L. 10^7 samples are taken for each point, and increasing variability among samples manifests in visibly increasing uncertainty in the ratio as the lengths increase. The ratio is found to increase exponentially with the lengths of the chains. **(Blue)** A discrete, balanced, two-component distribution (Equation (3.5)) with parameters $a = 0.05$ and $b = 0.15$. **(Orange)** A uniform distribution (Equation (3.4)) with the same parameters.

where the ratio is found to increase exponentially with the chain length. Local variability is therefore expected to become more significant as the code distance increases, and this is reflected in the results of our pseudo-threshold simulations, shown in Figure 3.4. This behaviour necessarily results in a slight upward shift in the sample accuracy threshold.

3.3 The Surface Code and Chain Entropy

The surface code is defined by mapping qubits and operations to an $l \times m$ rectangular lattice. Edges of this lattice represent qubits, while faces and vertices represent measurements of parity operators in the Z and X bases respectively (the bases are arbitrary, but must be orthogonal). These measurements are defined by Pauli-operator products acting non-trivially on qubits (edges) adjacent to their respective face or vertex,

$$\hat{S}_Z(f) = \otimes_{e\in\partial f}\hat{\sigma}_z^{(e)} \quad \text{and} \quad \hat{S}_X(v) = \otimes_{e|v\in\partial e}\hat{\sigma}_x^{(e)}, \tag{3.6}$$

as represented graphically in Figure 3.5. Here v are vertices, e are edges, and f are faces of the lattice. Vertices of degree-1 are excluded. The set of these measured operators generates the *stabiliser* group, S [245]. Elements in the stabiliser group commute with all logical operations and therefore preserve the subspace in which the logical qubit is encoded. We require that our system exists in the $+1$ eigenspace of the stabiliser group. By then ensuring that there is exactly one more physical qubit than there are generators of this group, we restrict the total space of our system to a two-dimensional subspace within which we can define a logical qubit.

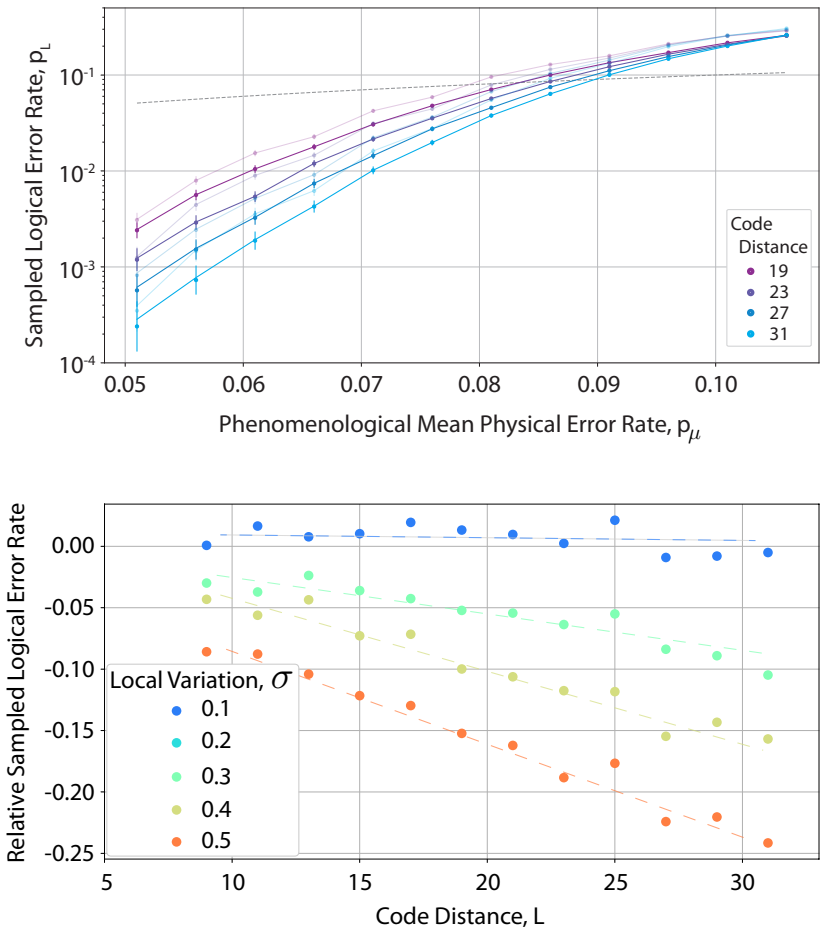

FIGURE 3.4: **(Top)** Sampled logical error rates for the repetition code over the code distances 9, 23, 27, and 31, as a function of the mean physical error rate p_μ. Two sets of series are shown: the error rates when the mean error probability p_μ is used for decoding (light) and those when local variation is incorporated (dark). For the latter series, the relative local width σ is 0.5. Also shown is the line of equality between the two axes (grey, dashed). Error bars denote 3 standard deviations from the mean, calculated according to the *Wilson Score* [242]. **(Bottom)** *Relative* change in the logical error rates when local information is incorporated, at a mean error rate $p_\mu = 0.091$, as a function of code distances between 9 and 31 and for relative widths of local variation σ between 0.1 and 0.5. Dashed lines are added to guide the eye. Each point in either graph is the result of 10^5 trials, decoded using Kolmogorov's *Blossom V* algorithm [243, 244] for minimum-weight perfect matching.

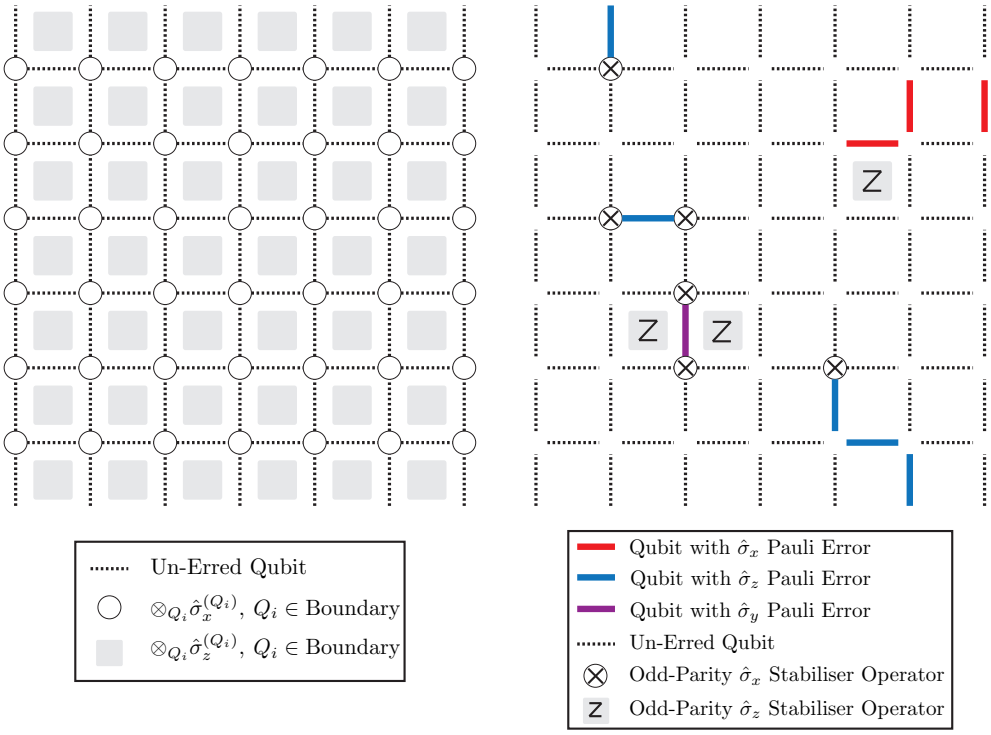

FIGURE 3.5: **a)** A diagram of a surface code of length 7. Dotted edges correspond to qubits in their initial state. An X-basis measurement (at a vertex) detects local σ_z operations and vice versa. Logical $\sigma_x^{(L)}$ operations stretch from the left side of the lattice to the right, while logical $\sigma_z^{(L)}$ operations stretch from the top edge of the lattice to the bottom. **b)** A sample error syndrome, where blue (red, purple) edges correspond to qubits following a local σ_z (σ_x, $i\sigma_y$) operation.

At the boundaries of the surface code, faces and vertices need not have the full complement of four adjacent edges. If a boundary consists of three-edge vertices, it is called *smooth*, while if it consists of three-edge faces, it is called *rough*. For the identification we have chosen, X-basis (Z-basis) operations on vertices (faces), a contiguous chain of Pauli σ_z (σ_x) errors with both end-points at a rough (smooth) boundary will be undetectable. If both ends of the chain meet a single, contiguous such boundary, then the chain is equivalent to the application of a stabilising operation and therefore acts trivially on the logical qubit. On the other hand, if such a chain has its end-points at two non-contiguous such boundaries, then there is no equivalent stabilising operation and the chain is *by definition* a logical operation. A logical operation is only unique up to elements of the stabiliser group, and is in this sense equivalent to any string of single qubit operations stretching between its two boundaries, though canonical representatives are usually defined as

$$\hat{\sigma}_x^{(L)} = \left(\otimes_{i=1}^{l} \sigma_x^{(i,1)}\right), \text{ and} \tag{3.7}$$

$$\hat{\sigma}_z^{(L)} = \left(\otimes_{j=1}^{m} \sigma_z^{(1,j)}\right), \tag{3.8}$$

where qubits are designated on the lattice by the two dimensional indices (i, j).

A surface code on an $L \times L$ lattice is a $[[L^2 + (L-1)^2, 1, L]]$ code: it requires $L^2 + (L-1)^2$ physical qubits, encodes at most 1 logical qubit, and has a *code distance* of L. The code distance indicates that states in the code space are topologically separated by L local qubit operations. As in Section 3.2, parity measurements are repeated to account for faulty measurements, extending the code into a third *time* dimension.

3.3.1 Lattice Dimension

The discussion in Section 3.2 assumed a simple, one-dimensional repetition code. With the surface code as a point of comparison, we can now discuss the effect of local variation in higher dimensions. Since we are assuming that physical errors occur at a constant rate, the impact of variation will be affected by the fraction of links in a given error chain corresponding to measurement error. Increasing the dimension of the code will decrease this fraction. However, extending the lattice along an additional dimension also increases the number of qubits as well as the multiplicity of equivalent error chains: the effect of moving to higher dimensions is not trivially apparent.

The number of direct paths connecting two vertices in an m-dimensional lattice, when these points are separated by an equal number of links, n, along each dimension, is $(mn)!/(n!)^m$. More generally, when points are separated by a number of steps d_i in dimension i, the number of direct paths is $(\sum_i d_i)!/\prod_i (d_i!)$; here we assume an average symmetry on the grounds of equal mean error rates p_μ. The assumption that the most likely error *chain* can be used as a proxy for the most likely error *class* relies on the condition that the exponential suppression in likelihood with length overcomes the additional entropic contribution from the increase in the number of chains. Approximating this as

$$\frac{(mn)!}{(n!)^m} p^{mn} \geq \frac{(m(n+1))!}{((n+1)!)^m} p^{m(n+1)}, \tag{3.9}$$

and using the further Stirling's approximation $n! \approx \sqrt{2\pi n}(\frac{n}{e})^n$ we can derive that

$$\frac{(mn)!}{(n!)^m} p^{mn} \approx \frac{(2\pi mn)^{1/2}}{(2\pi n)^{m/2}} \frac{\left(\frac{mn}{e}\right)^{mn}}{\left(\frac{n}{e}\right)^{mn}} p^{mn} \tag{3.10}$$

$$= \frac{\sqrt{m}}{(2\pi n)^{\frac{m-1}{2}}} (mp)^{mn}. \tag{3.11}$$

Restating the condition in Equation (3.9) then, we have

$$\frac{\sqrt{m}}{(2\pi n)^{\frac{m-1}{2}}} (mp)^{mn} \geq \frac{\sqrt{m}}{(2\pi(n+1))^{\frac{m-1}{2}}} (mp)^{m(n+1)} \tag{3.12}$$

or

$$p \leq \frac{1}{m} \left(\frac{n+1}{n}\right)^{\frac{m-1}{2m}}. \tag{3.13}$$

This approaches the finite value $p_{\text{Critical}} = 1/m$ as n increases, and remains larger than the accuracy thresholds of the surface code variants known at low dimensions.

The accuracy threshold of the code p_{th} indicates the regime in which it is likely to operate, at least in the near-term. Taking the ratio between the accuracy threshold of the code p_{th} and this critical probability p_{Critical} gives us a measure indicating the relative importance of the length or probability of a chain as against its multiplicity. For the repetition code of Section 3.2 we find that $p_{th}/p_{\text{Critical}} \approx 0.2$, while for the surface code we have $p_{th}/p_{\text{Critical}} \approx 0.09$. We conjecture that the approximate factor of 2 separating these ratios represents the relative significance of variation in the probability of a single error chain; this would be consistent with the approximate factor of 2 between the relative improvements found for the sampled results shown in Figures 3.4 and 3.6.

3.4 Discussion

In this work we have performed pseudo-threshold simulations using minimum-weight perfect matching and Kolmogorov's *Blossom V* algorithm [243,244], and have introduced two intuitive but approximate measures of qualitative, predictive utility. Our results show that accounting for local variability in measurement errors can reduce logical error rates by factors of order 30%, and also show evidence that this reduction increases for higher code distances and dimensions, under the minimum-weight perfect matching decoder.

The minimum-weight perfect matching decoder may run into difficulties at higher code distances when the weight of each chain is allowed to vary. The increase in the variance relative to the weight of the chain that we observed in Figure 3.3 indicates that the most likely single chain becomes less representative of its entire class as the length increases. At the same time, the variance of the entire class will itself increase; individual error chains will become less significant but variability in the set of such chains should become more useful. However, the number of chains in a set increases exponentially with the length — see Equation (3.11); when the distance between syndrome points is large, the inefficiency in classical processing required to account for the full class becomes prohibitive. A direct, online consideration of local variability therefore seems practically applicable only in small- to mid-level applications.

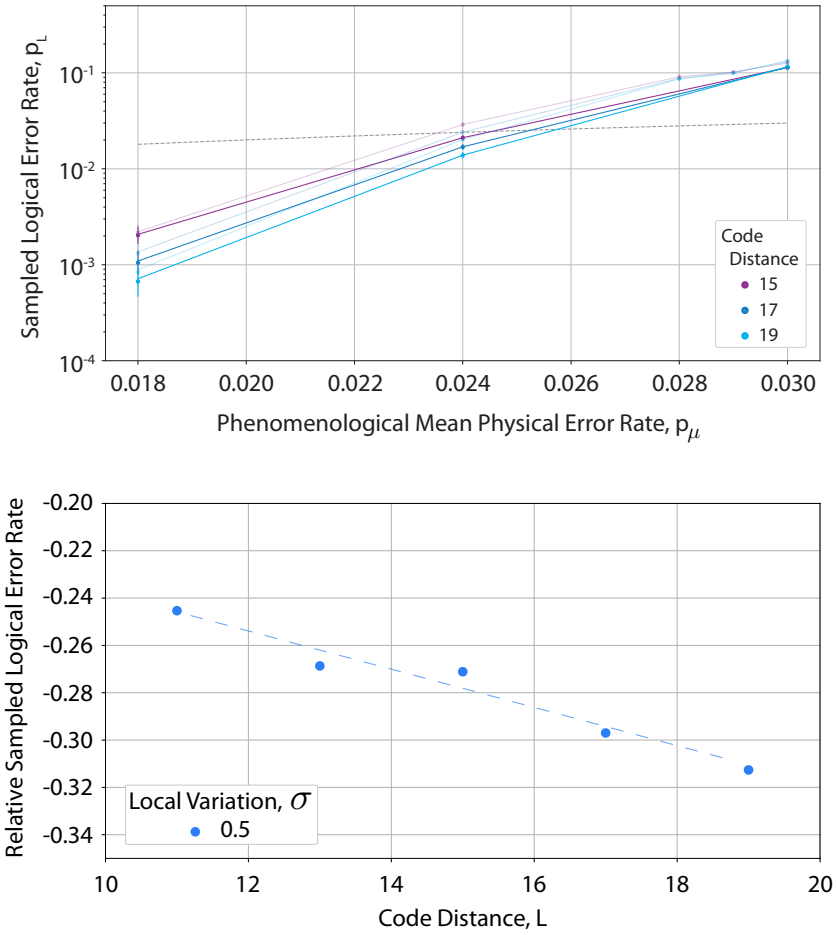

FIGURE 3.6: **(Top)** Sampled logical error rates for the surface code over the code distances 15, 17, and 19, as a function of the mean physical error rate p_μ. Two sets of series are shown: the error rates when the mean error probability p_μ is used for decoding (light) and those when local variation is incorporated (dark). For the latter series, the relative local width σ is 0.5. Also shown is the line of equality between the two axes (grey, dashed). Error bars denote 3 standard deviations from the mean, calculated according to the *Wilson Score* [242]. **(Bottom)** *Relative* change in the logical error rates when local information is incorporated, at a mean error rate $p_\mu = 0.024$, as a function of code distances between 11 and 19 and for a relative width of local variation $\sigma = 0.5$. The dashed line is added to guide the eye. Each point in either graph is the result of 10^5 trials, decoded using Kolmogorov's *Blossom V* algorithm [243, 244] for minimum-weight perfect matching.

Beyond small- to mid-level codes, the computational cost of the minimum-weight perfect matching decoder motivates the use of alternative decoding schemes. One popular alternative, the renormalisation group decoder of Cianci et al. [246–248], relies on pre-computed local tables. While this decoder is important because it allows us to parallelise the classical processing involved in decoding, it does not allow real-time local feedback. However, as the probability over the links of an error chain is multiplicative, the appropriate mean is geometric: the mean probability of a chain of fixed length should *decrease* as the variance of individual links increases. The prior distribution, though its variance, therefore has a direct macroscopic impact on the logical error rate and can be accounted for even in alternative decoding schemes using pre-computed tables. Additionally, we could consider qubit rotations subject to random analogue rotation errors, without the local feedback provided by many measurements.

We expect the local variability considered in this section to provide a large effective reduction in resource requirements for a given logical error rate, as near-term resources are severely limited and gate error rates for many systems remain at or near the accuracy threshold for the surface code of $\sim 1\%$. For two specific systems, the nitrogen– and silicon–vacancy centers in diamond, we consider several quantum gates exhibiting the local variation discussed above and their operational fidelities in Part II.

Part II

Physical Platform: Defect Centers in Diamond

Chapter 4

High-Fidelity Spin Measurement on the Nitrogen–Vacancy Center

Negatively charged nitrogen–vacancy (NV) centers in diamond are versatile candidates for many quantum information processing tasks, ranging from quantum imaging and sensing to quantum communication and fault-tolerant quantum computers. Critical to almost every potential application is an efficient mechanism for the high fidelity readout of the state of the electronic and nuclear spins. Typically such readout has been achieved through an optically resonant fluorescence measurement, but the presence of decay through a meta-stable state will limit its efficiency to the order of 99%. While this is good enough for many applications, it is insufficient for large scale quantum networks and fault-tolerant computational tasks. Here we explore an alternative approach based on dipole induced transparency (state-dependent reflection) in an NV center cavity QED system, using the most recent knowledge of the NV center's parameters to determine its feasibility, including the decay channels through the meta-stable subspace and photon ionization. We find that single-shot measurements above fault-tolerant thresholds should be available in the strong coupling regime for a wide range of cavity–center cooperativities, using a majority voting approach utilizing single photon detection. Furthermore, extremely high fidelity measurements are possible using weak optical pulses.

4.1 Introduction

The negatively charged nitrogen–vacancy center in diamond is an interesting candidate system for quantum technologies, with potential applications ranging from quantum metrology [249–256] to quantum communication [257–259], as well as simulation and computation [166, 259–265]. The NV^- center contains electronic and nuclear spin components, with both optical and microwave transitions, and remains stable even at room temperature [266]. Electronic spin coherence times can be achieved on the order of 1–100 milliseconds [267–269]. If the NV center is going to be used for tasks related to communication or computation, it needs to perform four core tasks:

- Coherent manipulation of electronic and nuclear spins,
- Entanglement generation between remote electronic spins,
- Entanglement swapping between the electronic and nuclear spin states within an NV center, enabling the storage of remote entanglement in the nuclear spins,
- Measurement of the electronic and nuclear spin states.

Though local operations (the coherent manipulation) of single centers has been performed with fidelities exceeding 0.999952(6) [178], sample fabrication and high fidelity measurements are technological challenges yet to be overcome [270, 271].

The typical measurement scheme for an NV^- center is based on a cycling transition between the $m_s = 0$ levels in the ground and excited state manifolds. The presence of decay channels from the optically excited manifold through a meta-stable state is expected to limit the efficiency of this scheme to order 99%. The efficiency is therefore likely to be below the threshold required for larger-scale communication and computational tasks, though recent work utilizing repeated initialization of the electronic state between measurement trials [272] may prove to circumvent this limitation in cases not related to the generation of entanglement. Cavity-enhanced transitions have been exploited in Purcell-enhanced fluorescence measurement schemes [273–275] and in emission-based entanglement schemes [276–278].

Recently an alternative approach based on dipole-induced transparency has been proposed [279–283] wherein the state of the NV center changes the resonance properties of an optical cavity. More specifically, if the electronic spin in its $|0\rangle_{m_s}$ state, an incident photon is reflected from the cavity, while for the $|+1\rangle_{m_s}$ electronic spin state the photon enters the cavity where it is scattered but not absorbed by the NV center. Detection of the reflected photon is thus a definite signature that the electronic spin was in the $|0\rangle_{m_s}$ state, though the photon need not interact directly with the state of the NV center. In this work, we build upon the analysis of [282] and make use of recent improvements in the understanding of the NV's low-temperature optical characteristics [284] to refine the quantification of the scheme's potential.

To summarise, high fidelity measurements are an outstanding requirement of a universal quantum primitive using the NV center. They are directly linked to entanglement generation between centers. Typical measurements involve luminescence detection, but direct optical excitation leaves the state vulnerable to unwanted decay and instability. A reflection-based scheme without excitation has been proposed, but this scheme has not been assessed for the NV center at low temperatures with a complete dynamical model. With these points in mind, we would like to answer the following question: For a complete modern description of NV center dynamics, are we able to achieve measurement satisfying the typical fault-tolerant performance threshold of 99.9%?

This section is structured as follows: Section 4.2 begins with an overview of the main properties of the nitrogen–vacancy center, followed in Section 4.3 by a description of the CQED system and the measurement scheme. Section 4.4 analyzes the measurement process in detail and estimates its performance, while Section 4.5 considers the effect of replacing the single photon source with weak coherent laser pulses. Finally, Section 4.6 summarizes the main conclusions of our analysis and briefly discusses some areas with the potential for improvement.

4.2 The Nitrogen–Vacancy Center

The negatively charged nitrogen–vacancy center in diamond consists of the nearest-neighbor pair of a subsitutional nitrogen atom with a lattice vacancy (green and red respectively in Figure 4.1). Three dangling bonds from carbon atoms adjacent to the vacancy, two dangling bonds from the Nitrogen atom and an additional electron form the electronic structure of the center. Isotopes of both nitrogen (14,15) and carbon (12,13) allow us to tailor the number and properties of the nuclear spins. ^{14}N has a spin-1 nuclear spin while that of ^{15}N is spin 1/2. Similarly, ^{12}C has no

nuclear spin while that of ^{13}C is spin 1/2. With isotopic engineering an NV center can be fabricated as one requires. For this article we consider an NV center with the ^{15}N isotope and no nearby ^{13}C carbon atoms. This leads to the simplest NV center consisting of a spin-1/2 nucleus and an electronic structure (see Figure 4.1) that is broadly classified by symmetry and/or multiplicity into three groups. These groups are the ground state manifold (GSM) $^3A_2$ (three non-degenerate states with a 180^o-rotation symmetry about the principle axis), the optically excited state manifold (ESM) ^{3}E (three doubly-degenerate states), and the meta-stable manifold (MSM) containing the singlets $^1A_1$, one non-degenerate state with both 180^o-rotation and reflection symmetries, and ^{1}E, one doubly-degenerate state. The ground and optically excited states can be decomposed into two three-level subsystems. The ground states we refer to as the 'electron spin' S, with quantum number m_s (and the nuclear spin I, with quantum number m_n). This will distinguish it from optical excitation, which we refer to as a change in the 'orbital angular momentum' L, with quantum number m_l.

The structure of this center can be described, under minor approximations [1], by the Hamiltonian [266]

$$H_{NV} = H_{GSM} \otimes |0\rangle \langle 0|_{m_l} + H_{ESM} \tag{4.1}$$

where H_{GSM} gives the structure of the ground state manifold and can be expressed as

$$\begin{aligned} H_{GSM} &= \hbar D_{GSM} \left(S_z^2 - \frac{2}{3} \right) + \mu_B g_{GSM}^{||} S_z B_z \\ &\quad + \mu_N g_n^{||} I_z^{(n)} B_z. \end{aligned} \tag{4.2}$$

Here S and I representing the usual electronic spin-1 and nuclear spin $\frac{1}{2}$ operators (with S_z and I_z being their respective z-components). The first term in H_{GSM} represents an electronic spin zero field splitting of $D_{GSM}/2\pi = 2.88$ GHz, while the second (third) represents a magnetic field B_z splitting of the electronic spin $|\pm 1\rangle_{m_s}$ (nuclear spin $\left|\pm\frac{1}{2}\right\rangle_{m_n}$) states with the Bohr magneton (nuclear magneton) given by $\mu_B/2\pi\hbar = 14$ GHzT^{-1} ($\mu_N/2\pi\hbar = 7.63$ MHzT^{-1}). The g-factors are $g_{GSM}^{||} = 2.01$ and $g_n^{||} = -0.566$ respectively.

[1] We ignore the axial hyperfine interaction in our Hamiltonian because it does not significantly change optical transition detunings and because its relative phase does not affect the fidelity of measurement in the spin basis. We have also removed cross-terms from the ground state Hamiltonian on the basis of their strength. These terms are the hyperfine spin-flip interaction, $A_\perp = 3.65$ MHz [285, 286] and the transverse strain field, $\delta_x \approx 1$ MHz [287]. The energy gap, GHz, between the spin states they connect diminishes their effect. Moving to the dispersive-regime, the respective evolution terms can be approximated by $A_\perp^2 t/(\text{GHz})$ and $\delta_x^2 t/(\text{GHz})$. Measurement pulses are separated on timescales of the order 100 ns; over the course of a single such pulse these quantities are expected to change state amplitudes to order $(10^6)^2 10^{-7}/10^9 = 10^{-4}$ and probabilities to order 10^{-8}, which we can neglect

[2] Lifetimes and decay percentages through the meta-stable subspace are estimated from the 0 mT values using the energy level mixing ratios. For the low-temperature excited-state Hamiltonian we are using parameters averaged between those of [288, 289].

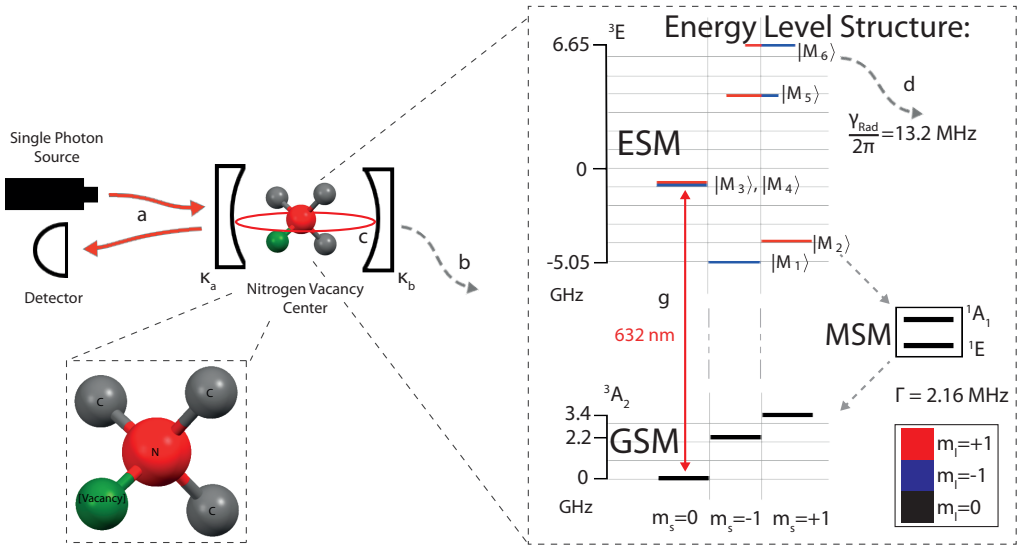

FIGURE 4.1: **(Left)** Schematic illustration for single-photon measurement of the NV^- electron spin state based on dipole-induced transparency. The CQED system is driven by a single-photon source while detection in the reflected mode is used to infer information about the state of the NV^- center. The NV center is composed of an adjacent nitrogen atom (red) and lattice vacancy (green) in a tetrahedral carbon lattice (gray). **(Right)** The electronic energy level structure of the NV^- center, at low temperature under a $B_z = 20$ mT external magnetic field set along the NV axis. The energy levels are represented by bold horizontal lines and grouped into three subspaces: *ground state manifold (GSM)*, *excited state manifold (ESM)* and *meta-stable state manifold (MSM)*. Allowed radiative transitions between the ground and optically excited states are horizontally segmented, with overlap indicating relative spin composition of the energy eigenstates. The optically excited states contain non-zero orbital angular momentum components $+1$ (red) and -1 (blue). Dashed arrows represent decay paths not resulting in reflection of a photon incident on the cavity (they represent transmission into the cavity mode, *c*, through the second cavity mirror (into *b*), spontaneous emission into the free field (*d*) and decay to a meta-stable state). The solid double-sided arrow represents a possible zero-phonon line transition in resonance with the optical cavity.

TABLE 4.1: Relative energy levels E (and low temperature free lifetimes τ [284, 291]) of the optically excited states, showing the polarization of dominant transitions at both zero and 20 mT external fields. Small mixing of spin states (below 1%) is not shown here. The 20 mT segment of this table is consistent with the energy level diagram in Figure 4.1. We also indicate the proportion of the spontaneous decay through a meta-stable (MS) state.[2]

0 mT	E_2	E_1	E_x	E_y	A_1	A_2
E (GHz)	-4.46	-4.46	-0.796	-0.796	3.98	6.53
τ (ns)	7.5	7.5	12.1	12.1	5.1	12.1
MS decay	38%	38%	$0-1\%$	$0-1\%$	54%	$0-1\%$
$m_s=-1$	σ_-				σ_+	σ_+
$m_s=0$			$\sigma_+ + \sigma_-$	$\sigma_+ - \sigma_-$		
$m_s=+1$		σ_+			σ_-	$-\sigma_-$
20 mT	M_1	M_2	M_3	M_4	M_5	M_6
E (GHz)	-5.05	-3.87	-0.82	-0.77	3.87	6.64
τ (ns)	7.5	7.5	12.1	12.1	5.2	11.5
MS decay	38%	38%	$0-1\%$	$0-1\%$	52%	$2-3\%$
$m_s=-1$	σ_-				$0.83\sigma_+$	$0.56\sigma_+$
$m_s=0$			σ_-	σ_+		
$m_s=+1$		σ_+			$0.56\sigma_-$	$-0.83\sigma_-$

The structure of the excited state manifold is determined by the component H_{ESM}, where

$$\begin{aligned} H_{ESM} &= \hbar D_{ESM}^{||}\left(S_z^2-\frac{2}{3}\right)L_z^2 - \hbar\lambda_{ESM}^{||}S_zL_z \\ &+ \frac{\hbar}{2}D_{ESM}^{\perp}\left(S_y^2-S_x^2\right)\left(L_x^2-L_y^2\right) \\ &- \frac{\hbar}{2}D_{ESM}^{\perp}\left(S_yS_x+S_xS_y\right)\left(L_xL_y+L_yL_x\right) \\ &+ \frac{\hbar}{2}\lambda_{ESM}^{\perp}\left(S_xS_z+S_zS_x\right)\left(L_x^2-L_y^2\right) \\ &- \frac{\hbar}{2}\lambda_{ESM}^{\perp}\left(S_yS_z+S_zS_y\right)\left(L_xL_y+L_yL_x\right) \\ &+ \mu_B\left(l_{ESM}^{||}L_z+g_{ESM}^{||}S_zL_z^2\right)B_z. \end{aligned} \tag{4.3}$$

Here $D_{ESM}^{||}/2\pi = 1.21$ GHz denotes the zero-field splitting, $D_{ESM}^{\perp}/2\pi = 0.6375$ GHz, $\lambda_{ESM}^{||}/2\pi = 4.85$ GHz, and $\lambda_{ESM}^{\perp}/2\pi = 0.141$ GHz are spin-orbit interaction terms and $g_{ESM}^{||}, g_{ESM}^{\perp} = 2.01$ ($l_{ESM}^{||} = 0.1$) are the electronic spin (orbital angular momentum) g-factors respectively. At cryogenic temperatures ($4-8$ K) the non-zero orbital angular momentum components are distinct [288, 289] and determine photon polarization selection rules on allowed optical transitions [290]. These are enumerated in Table 4.1 (along with free transition lifetimes [284, 291]) for the zero-field and 20 mT external magnetic field cases [3]. The zero-phonon line between the $|0\rangle_{m_s}$ intrinsic spin ground state and the optically excited states at zero field is 637nm.

[3] We have assumed ideal control over the electric and magnetic fields; we expect, though the effects are not investigated here, that a transition to the large magnetic field regime would suppress variation in the electric field (or due to strain). As noted by Childress et al. [257], for weak driving, fluctuations

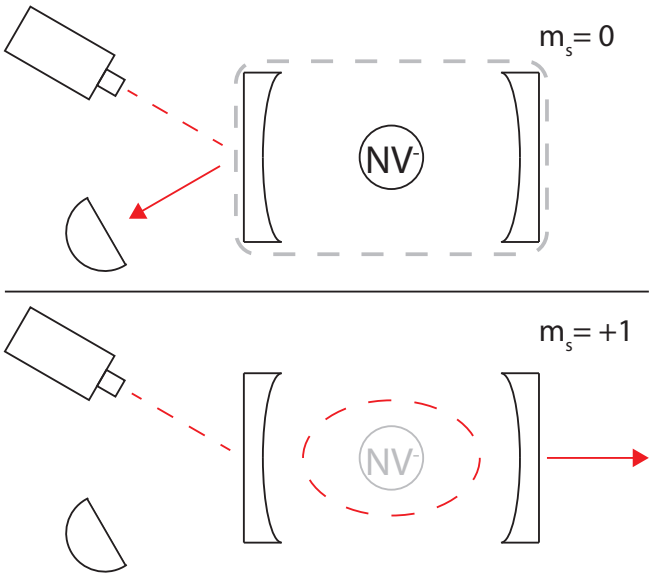

FIGURE 4.2: When the nitrogen–vacancy center is in the $m_s = 0$ ground state, resonant coupling with the optical cavity causes the composite system to form dressed states detuned from the frequency of the incident photon — the photon does not enter the cavity, and is reflected. When the nitrogen–vacancy center is in the $m_s = +1$ state, there is no optical transition close enough in energy to be able to couple with the cavity mode — the photon *sees* an empty cavity, enters, and is transmitted. In such ideal cases, no interaction occurs between the incident photon and the nitrogen–vacancy center, preserving the center's state.

As the nitrogen–vacancy center decays, emission into the phonon side-band collectively exceeds emission at the zero-phonon line [292–294]. Elastic scattering occurs approximately 3–5% of the time [295–299], linearly degrading the cooperativity of a coupled cavity.

Next (as seen in Figure 4.1), a decay channel couples the optically excited states to a meta-stable subspace. These decay rates (shown in Table 4.1) can have a significant effect on the measurement fidelity as decay through a meta-stable state removes phase information and introduce a bit-flip error rate of 67–81% from the $m_s = +1$ state, and 38–65% from the $m_s = 0$ state [300, 301]. Here we assume a polarizing sample with a bit-flip rate 81% from the $m_s = +1$ state, and 38% from the $m_s = 0$ state. The longer-lived ^{1}E meta-stable state has a lifetime of 462 ns at 4.4 K, while the shorter-lived ^{1}A$_1$ state (separated by a 1042 nm energy gap from its ^{1}E counterpart) has a lifetime of less than 1 ns [302]. Transitions to and from the meta-stable subspace do not conserve the intrinsic electron spin [284], they therefore degrade the measurement fidelity.

4.3 Photonic Readout of the Nitrogen–Vacancy Center State

The optically accessible transitions in an NV center provide a natural way to measure it, given the excellent frequency separation of allowed transitions from the $m_s = 0$ state relative to those of the $m_s = \pm 1$ states (Table 4.1). The absence of hyperfine

in the transition energies over time have the effect of broadening the transition, combining with the decay rate to reduce the cooperativity.

interactions [4] and the smaller decay rates from the $m_s = 0$ ESM levels to the meta-stable subspace leads to the selection of the $|0\rangle_{m_s} \leftrightarrow |M_{3,4}\rangle_{m_s}$ transitions for the optical readout. The presence of decay through a meta-stable state, however, limits that measurement efficiency after a certain number of light pulses, as the excited states $|M_{3,4}\rangle_{m_s}$ will decay into the MSM ($< 1\%$ of the time). Dipole-induced transparency (giant Faraday rotation) [280–283, 303] provides an elegant way to mitigate this effect, as we can use strong coupling between our NV center and an optical cavity to modify the resonance properties of that cavity. In this strong coupling regime, a σ_+ polarized photon near resonance with the empty cavity and with the $|0\rangle_{m_s} \leftrightarrow |M_4\rangle_{m_s}$ transition would be reflected when the NV center is in the $|0\rangle_{m_s}$ state [5]. This means the photon is not absorbed by the NV center, mitigating the effect of decay through the meta-stable state and providing, in the ideal case, an interaction-free measurement. On the other hand, the photon will be transmitted through the cavity (and not absorbed or scattered) if the NV center is in its $|\pm 1\rangle_{m_s}$ states as it is far off resonance with the $|\pm 1\rangle_{m_s} \leftrightarrow |M_{1,2,5,6}\rangle_{m_s}$ transitions. Measurement of the presence or absence of the reflected photon (or series of photons) thus allows us to infer the state of the NV's electron spin. How well this works required a detailed analysis of the entire measurement scheme.

Coupling between the cavity, external field modes and electron spin can be represented as shown in Figure 4.1 and by the Hamiltonian

$$\begin{aligned} H_{\text{coupling}} &= \hbar\left[c\left(\sqrt{\frac{\kappa_a}{\pi}}a^\dagger + \sqrt{\frac{\kappa_b}{\pi}}b^\dagger\right) + \sqrt{2}gcL_x\right] \\ &+ \hbar\sum_{i=1}^{6}\sqrt{\frac{2\gamma_i}{\pi}}d|M_i\rangle\langle M_i|L_x + \text{h.c}, \end{aligned} \tag{4.4}$$

where a, b, c, d ($a^\dagger, b^\dagger, c^\dagger, d^\dagger$) are the annihilation (creation) operators of the reflected, transmitted, cavity and scattering (spontaneous emission) operators. Next, L_x is the angular spin-1 X operator while g is the vacuum-Rabi coupling rate. Further, κ_a and κ_b are the left and right mirror cavity decay rates, which we assume are equal giving us a total decay rate $\kappa = \kappa_a + \kappa_b$. Finally, γ_i is half the spontaneous decay rate of the ith optically excited state [6]. These three parameters allow us to define the cooperativity $C_i = g^2/2\kappa\gamma_i$, a dimensionless measure of coherent coupling [304].

The Hamiltonians in Equations (4.2), (4.3) and (4.4) incorporate spin-1 operators $S_{x,y,z}$ and $L_{x,y,z}$. Explicitly, for the m_s subsystem these are

$$S_z = \begin{bmatrix} 1 & 0 & 0 \\ 0 & 0 & 0 \\ 0 & 0 & -1 \end{bmatrix}, \quad S_x = \frac{1}{\sqrt{2}}\begin{bmatrix} 0 & 1 & 0 \\ 1 & 0 & 1 \\ 0 & 1 & 0 \end{bmatrix}, \quad S_y = \frac{1}{\sqrt{2}}\begin{bmatrix} 0 & -i & 0 \\ i & 0 & -i \\ 0 & i & 0 \end{bmatrix} \tag{4.5}$$

so that the raising and lowering operators are given by

$$S_+ = \sqrt{2}\begin{bmatrix} 0 & 1 & 0 \\ 0 & 0 & 1 \\ 0 & 0 & 0 \end{bmatrix}, \qquad S_- = \sqrt{2}\begin{bmatrix} 0 & 0 & 0 \\ 1 & 0 & 0 \\ 0 & 1 & 0 \end{bmatrix}. \tag{4.6}$$

Matrices for the m_l subsystem are identical.

[4] The hyperfine interaction is effectively turned off for the $m_s = 0$ levels, while there is a difference in hyperfine coupling constants between the ESM and GSM $m_s = \pm 1$ levels. The spontaneous nature of the decay from the ESM will lead to a small random phase shift in this case.

[5] The use of a σ_+ polarized photon means that photon can not be resonant with the $|0\rangle_{m_s} - |M3\rangle$ transition.

[6] These have not be measured at 20 mT but their values can be estimated roughly by appropriate mixing of the zero-field values.

On resonance, the coupling is related to the spontaneous decay rate by

$$g = \sqrt{\rho_\omega \frac{\pi^2 c^3}{\hbar \omega^3} \frac{\gamma_{Rad}}{2\pi} f}, \tag{4.7}$$

where f is the Huang-Rhys quantum efficiency of the transition ($0.03 - 0.05$ for the nitrogen–vacancy center), γ_{Rad} is the radiative component of the spontaneous decay rate ($2\pi \times 13.2$ MHz), ω is the angular frequency of the transition, c is the speed of light, and ρ_ω denotes the energy density of the cavity-field per unit angular frequency [305].

With the NV and coupling Hamiltonians we can derive Langevin equations of motion for the various field and spin operators. These are nonlinear in nature due to coupling terms between the field and spin operators, which makes them difficult to solve in general. Two alternative approaches can be taken to simplify this situation: the first assumes that NV center is always in the GSM while the second is to work in a single excitation subspace [306] where the field probing the NV center contains no more than one photon (both approaches lead to the same answer). We take the second route and will use probe fields with at most one photon.

The Hamiltonian, in Equations 4.2, 4.3 and 4.4, is first expanded to distinguish between photon polarizations (σ_+ and σ_-), so as to preserve orbital angular momentum and enforce polarization selection rules:

$$cL_x \rightarrow c_{\sigma_+} L_+ + c_{\sigma_-} L_- \tag{4.8}$$

$$c\left(a^\dagger + b^\dagger\right) \rightarrow c_{\sigma_+}\left(a^\dagger_{\sigma_+} + b^\dagger_{\sigma_+}\right) + c_{\sigma_-}\left(a^\dagger_{\sigma_-} + b^\dagger_{\sigma_-}\right) \tag{4.9}$$

Next, exploiting conservation of energy to bind us within the single-excitation subspace, we define composite operators fully characterising the spin and angular momentum states of the system, such that the equations of motion are linear in these operators. Two examples are lowering operators we will arbitrarily call $\hat{C}$ and $\hat{E}$ (for *Cavity*-mode and *Excitation*), corresponding respectively to $c^\dagger_{\sigma_+} c_{\sigma_+} = 1, m_s = +1, m_l = 0$ and to $m_s = +1, m_l = +1$.

$$\hat{C} = c_{\sigma_+} S_- \left(S_z^2 + S_z\right)/2 \tag{4.10}$$

$$\hat{E} = L_- S_- \left(L_z^2 + L_z\right)\left(S_z^2 + S_z\right)/4. \tag{4.11}$$

The mean values for $\hat{C}$, $\hat{E}$, and their equivalents for the orthogonal polarization and when $m_s \neq +1$ are important because they are directly related to output scattering rates. Finally, we derive Langevin equations for these composite operators of the form

$$\frac{\partial \hat{C}(t)}{\partial t} = -i\left[\left(\omega_c + D^{||}_{gs} + \frac{\mu_B}{\hbar} g^{||}_{gs} B_z - i\frac{\kappa}{2}\right)\hat{C}(t) + \alpha_{\hat{C}}\sqrt{\frac{\kappa}{2\pi}} e^{-ikt} + g\hat{E}(t)\right]. \tag{4.12}$$

Here $\alpha_{\hat{C}}$ is the amplitude of driving into the σ_+–polarized cavity mode, k is the frequency of this driving, ω_c is the cavity mode frequency, t is the time-dependence of the operators, and other parameters are obtained from the aforementioned Hamiltonians. Performing a Fourier transform gives us a set of linear equations, which can then be solved using the standard methods of numerical linear algebra to obtain the scattering matrix.

This approximation results in a set of linear Langevin equations that are straightforward but tedious to solve. The solutions are those for the cavity mode and excited states and not what we measure. However by using input–output relations [307]

$$a_{\text{out}}(t) = a_{\text{in}}(t) - i\sqrt{\kappa}c(t), \tag{4.13}$$

we can express our output field $a_{\text{out}}(t)$ in terms of the cavity field $c(t)$ and the cavity input field $a_{\text{in}}(t)$. This then enables us to calculate the mean photon number $\langle a^{\dagger}_{\text{out}}(t)a_{\text{out}}(t)\rangle$ over time and so determine whether an incident photon was reflected or not.

Source and detection efficiencies, as well as losses and imperfections, mean that one single-photon measurement will not be sufficient to determine the NV state with the accuracy we require. Instead our measurement here consists of a series of temporally spaced single-photon pulses which we individually attempt to detect. The time between photon pulses is chosen to be ~ 165 ns, from the axial hyperfine Rabi period. By matching gate times to this period, the effect of electron dephasing on the nuclear state can be minimized. Though it is not possible to restrict pulse times exactly to a periodic point, it has been shown that error associated with decay channels following optical excitation can be reduced by centering the pulse on such a point [308]. This is much larger than the excited state lifetime of the $|M_4\rangle$ state (12.1 ns) [284], but significantly shorter than the GSM decoherence times.

The outcome at the detector of each measurement pulse is dependent on its initial state distribution and thus successive outcomes are dependent on the detection history preceding them. After n pulses therefore there are 2^n possible measurement paths. Not all branches in the outcome tree will be full-length, however, as outcome branches that are successful early in the procedure can be truncated. In particular, reflection from the $|+1\rangle_{m_s}$ state can be suppressed by polarization and detuning, so that a detection event very strongly indicates the $|0\rangle_{m_s}$ state and will terminate an outcome branch (especially as dark count probabilities can be exceptionally low [309–311]).

4.4 Simulation of the Measurement Process

Along with our description of the NV^- center's photonic readout, let us now turn our attention to simulating it. Our model has a large number of parameters, but with the external magnetic (electric) fields set at 20 mT (0 V/m), our primary focus will be restricted to four experimentally relevant parameters: the cooperativity C, single photon source and detection efficiencies and the $m_s = 0$ decay rates through the meta-stable subspace. Figure 4.3 shows example transmission and reflection spectra.

It is useful to begin by considering the situation with perfect single photon sources and detectors but with finite cooperativity C and transitions through the meta-stable subspace (in the range 0–1% for the target transition, as indicated in Table 4.1). When the electronic spin is in its $|0\rangle_{m_s}$ state, an incoming photon is reflected with a probability $P_R \approx 4C^2/(2C+1)^2$, so that if we send n photons, the probability of detecting one or more photons is $p_s = 1-(1-P_R)^n$ (equivalently we need $n = \log(1-p_s)/\log(1-P_R)$ trials to have at least one photon detected with success probability p_s). There are two n's of interest here, n_{ave} and n_{ft}. n_{ave} is associated with the average number of single photon trials to get a measurement 'click' while n_{ft} is the number that guarantees at least one measurement click with probability above the fault tolerance threshold we set of 99.9%. For an initial state $|+1\rangle_{m_s}$ we have to perform n_{ft} trials (we call this trial limit number the *stop-limit*) with no clicks to infer

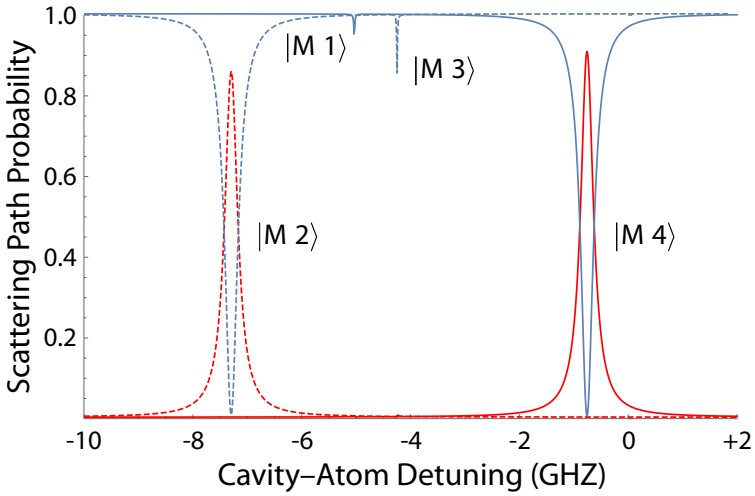

FIGURE 4.3: Reflection (red) and transmission (blue) spectra, over a range of cavity-atom detunings relative to the energies depicted in Figure 4.1, when the nitrogen–vacancy center is in the $|0\rangle_{m_s}$ (solid line) and $|+1\rangle_{m_s}$ (dashed line) states. σ_+ photon polarization has removed several other possible transitions. The cooperativity is taken at $C = 10$. The presence of additional decay paths prevents these lines from summing to one. Alternative decay pathways include spontaneous decay outside of the cavity mode, phonon-line decay, and non-radiative decay to the meta-stable states.

it was this state (with error probability $1 - p_s$). Figure 4.4 shows the effect of the cooperativity on both n_{ave}, n_{ft} and the measurement fidelities $F_{i\in\{0,+1\}} = \langle i|\rho|i\rangle_{m_s}$ (where ρ is the state of the system after the n trials) for varying decay rates to the meta-stable subspace. As the cooperativity, and therefore also the reflection probability, increases, the number of trials required to achieve p_s decreases in integer steps. These steps manifest as negative discontinuous jumps in the measurement fidelity.

When we start with a general superposition state, each measurement pulse will introduce some error and so the reflection probability will not remain static as was assumed in Figure 4.4. Instead, the contrast between the initial $|0\rangle_{m_s}$ and $|+1\rangle_{m_s}$ states will degrade as the number of pulses increases, thereby increasing n_{ft}. Rather than initially specifying a maximum number of trials, we can look at the performance over a range of such numbers to identify an optimum number of measurement trials and the sensitivity of the measurement performance to changes in this number. In Figure 4.5 we plot the measurement fidelity for the initial state

$$\left(|0\rangle_{m_s}\left|-\frac{1}{2}\right\rangle_{m_n} + |+1\rangle_{m_s}\left|+\frac{1}{2}\right\rangle_{m_n}\right)/\sqrt{2}. \tag{4.14}$$

For the ideal case we observe that the 99.9% threshold is met even at cooperativities as low as $C = 2$, and that the dependence of the measurement fidelity on the pulse number, while sensitive at low cooperativities, is as low as order 0.0001 for cooperativities greater than 5.

Now including the effects of source and detection efficiency into our analysis, we show in Figure 4.6 the behavior of the measurement fidelity as a function of source and detection efficiencies. We observe that the performance depends slightly more sensitively on the detector than the source, but that the performance is robust for extraction rates ~ 0.9.

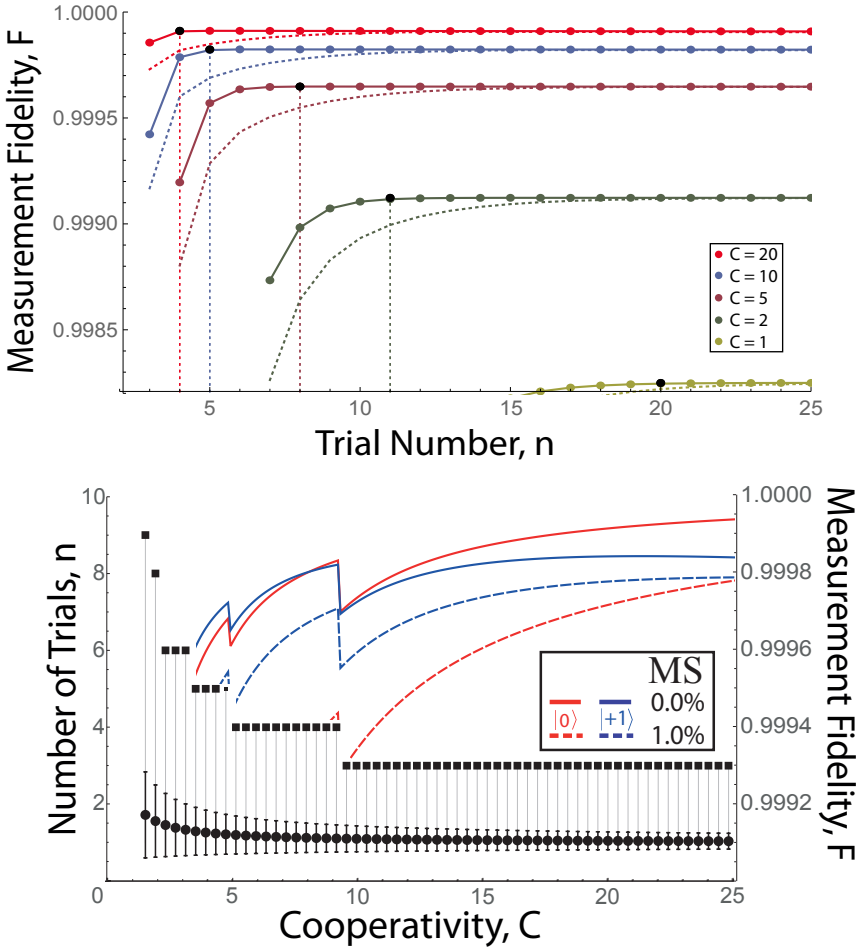

FIGURE 4.4: **(Top)** The measurement fidelity as a function of the number of measurement trials performed, displayed for a set of cooperativity values from 1 to 20. Peak numbers are indicated by black dots and with dashed lines. Dotted lines indicate the performance when the $m_s = 0$ decay to the metastable subspace is 1%. **(Bottom, Left Axis)** The number of trials n to obtain a positive measurement result (a reflected photon or 'click') for an electronic spin prepared in the $|0\rangle_{m_s}$ state, as a function of the cooperativity. Depicted are the mean number n_{ave} (solid circles) with one standard deviation error bars and n_{ft}, the number of trials needed for a single photon to be reflected with probability $p_s \geq 0.999$ (solid squares), rounded up to the nearest integer value. Numbers are calculated based on the reflection probability of an initial pure state. **(Bottom, Right Axis)** The measurement fidelities F_0 (red curve) and F_{+1} (blue curve) for varying $m_s = 0$ transition rates through the meta-stable subspace (expressed as a percentage of the total spontaneous decay rate). The discrete drops in the measurement fidelities are due to the integer nature of the number of trials required which drops as the cooperativity increases. Results are truncated at low cooperativities to avoid obfuscation with data on the left axis.

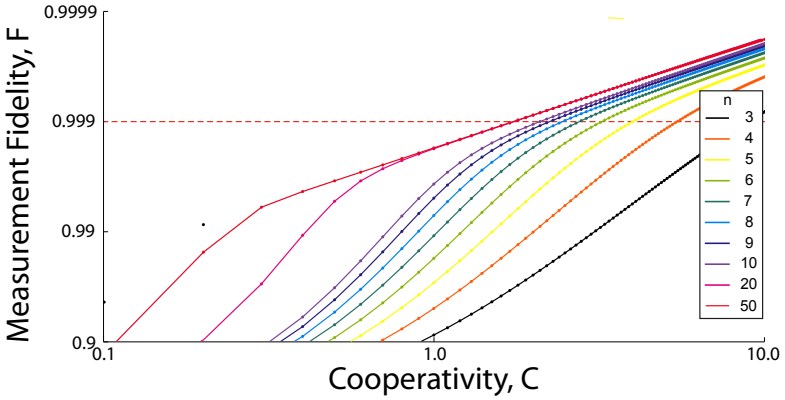

FIGURE 4.5: Measurement fidelity, F, as function of the cooperativity, C, for an ideal single-photon source and detector, over a range of measurement pulses, n. The $m_s = 0$ decay rate to the meta-stable subspace is 1%. While the optimal number of pulses decreases with increasing cooperativity, the error associated with moving away from this optimum is very small (~ 0.0001) for cooperativities above 5.

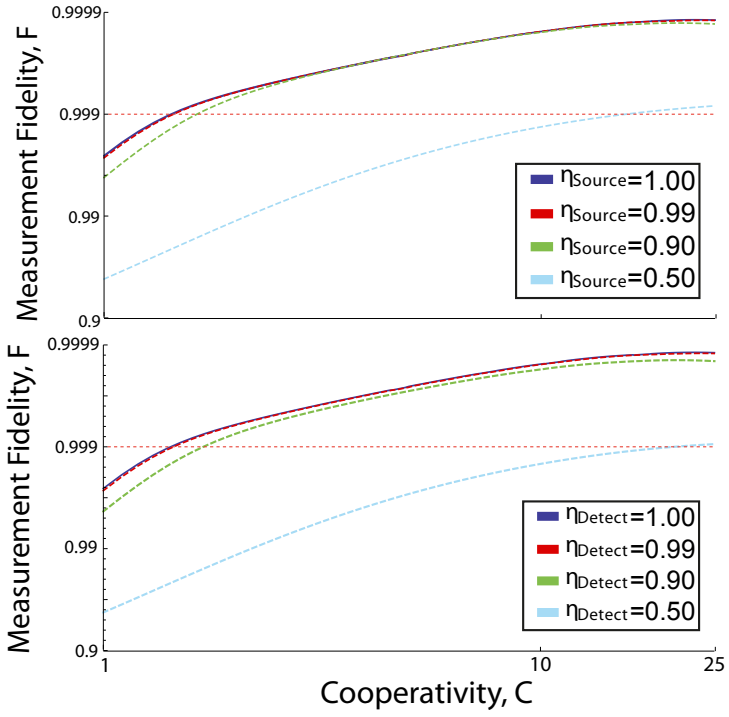

FIGURE 4.6: Loss of measurement fidelity, F, for a maximum of 10 photon pulses and a system initialized in the electronic and nuclear spin state $\left(|0\rangle_{m_s}\left|-\frac{1}{2}\right\rangle_{m_n} + |+1\rangle_{m_s}\left|+\frac{1}{2}\right\rangle_{m_n}\right)/\sqrt{2}$, as a function of the cooperativity, C, and **(Top)** single-photon source efficiency, η_{Source}, and **(Bottom)** single-photon detection efficiency, η_{Detect}. The $m_s = 0$ decay rate to the meta-stable subspace is taken to be 1%.

4.4.1 Realistic Performance Estimate

A natural question to ask is what our expected measurement fidelity would be with current technology. To this end let us specify a cooperativity of 0.2 [312], a single-photon source probability of 60% [7], a single-photon detection efficiency of 92% [310, 311, 315–318], and $m_s = 0$ decay rates to the meta-stable subspace of 1% [284]. Our model then predicts a maximum measurement fidelity of $F = 0.992$ occurring (within rounding error) after 145 single photon pulses. The total time for the measurement is then $\sim 150 \times 165$ ns $\approx 25\,\mu$s. During this time we would expect an electron spin dephasing error between 1%–0.01% for coherence times in the region 1–100 ms. The upper range would have a consequential effect on remote entangling operations, though dephasing should not effect the nuclear spin measurements. Limiting the maximum number of pulses to 10 reduces the measurement fidelity to $F = 0.686$. In Table 4.2 for contrast we outline similar numbers for $C \in \{0.5, 1, 2, 5, 10\}$ and $\eta_{Source}, \eta_{Detect} \in \{0.2, 0.6\}$. For a low source efficiency, it is apparent that high measurement fidelities can be maintained at the cost of greatly increasing the number of pulses.

TABLE 4.2: Measurement fidelities, F, and pulse numbers, n, when the $m_s = 0$ decay rate to the meta-stable subspace is 1%, varying the cooperativity and the single-photon source and detection efficiencies, η_{Source} and η_{Detect}.

C	η_{Source}	η_{Detect}	F	n
0.5	0.2	1.0	0.9965	290
1	0.2	1.0	0.9982	159
2	0.2	1.0	0.9992	80
5	0.2	1.0	0.9997	66
10	0.2	1.0	0.9998	57
0.5	0.6	1.0	0.9965	93
1	0.6	1.0	0.9985	42
2	0.6	1.0	0.9992	27
5	0.6	1.0	0.9997	19
10	0.6	1.0	0.9998	15
0.5	1.0	0.2	0.9830	255
1	1.0	0.2	0.9914	141
2	1.0	0.2	0.9962	73
5	1.0	0.2	0.9983	57
10	1.0	0.2	0.9990	49
0.5	1.0	0.6	0.9950	72
1	1.0	0.6	0.9975	41
2	1.0	0.6	0.9987	24
5	1.0	0.6	0.9995	18
10	1.0	0.6	0.9997	15

[7] PPLN sources can be purchased with 60% heralding efficiency [313], which may be multiplexed at a low individual extraction rate to suppress multi-photon components. Recent genuine single-photon sources have also been built based on quantum dots [314] that have achieved extraction efficiencies of 65%, though unpolarized and at a different frequency than the one we require

4.4.2 Single Photon Pulses

In any realistic model we also need to consider the bandwidth of our atomic resonances compared to those of the photon. Here we are working in the regime where the photon bandwidth is much less than the transform limited linewidth of the NV center's zero-phonon optical transitions. Our single photon pulses are 165 ns apart implying a bandwidth at least of order $\Gamma_P/2\pi \sim 1/2$ MHz (HWHM). The reflection spectrum from $|0\rangle_{m_s}$ is not sensitive at those scales but reflection from $|+1\rangle_{m_s}$ sits in the trough of a narrow resonance ($\Gamma_R \sim \kappa = 2\pi \times 50$ MHz), necessitating further consideration. We assume a Gaussian pulse shape,

$$\frac{1}{\sqrt{2\sigma_t^2\pi}} e^{\frac{-(t-165/2)^2}{2\sigma_t^2}}, \tag{4.15}$$

and set the standard deviation to $\sigma_t = 165/6$ ns so that the width of the pulse is much less than the time between pulses (at three standard deviations the area truncated in the tails is 0.3%). By the time–bandwith product, $\sigma_t^2\sigma_P^2 = 1/4$, the standard deviation in the frequency then becomes $\sigma_P/2\pi = 2.9$ MHz. By integrating over the probability-weighted reflection spectrum we can estimate the realistic reflection probability to be

$$\begin{aligned} P_{ave\ R} &\sim 1 - \sqrt{\pi}\,(\sigma_t\kappa)\,\mathrm{erfcx}\,(\sigma_t\kappa) \\ &= 0.66\% \end{aligned} \tag{4.16}$$

The reflection here is a direct result of the relative magnitudes of the photon and cavity linewidths, and is not influenced by the nitrogen–vacancy center. Since the width of the reflection trough is set by κ, it also governs the transmission and scattering peaks, which are each reduced to 99.34% of their maximum values. A 0.66% reflection probability from the $|+1\rangle_{m_s}$ state, when we want to suppress our error to within 0.1%, means that detection is no longer a strongly-classifying event.

Let us assume our initial state is predetermined and restricted to the $\{|0\rangle_{m_s}$ and $|+1\rangle_{m_s}\}$ subspace, but that the fidelity decays exponentially in the number of photon pulses. The probability of each state after n pulses is then given by Bayes' theorem and a binomial distribution (similar to the treatment of a Poisson-distribution in [283]). The probability of a detection event from $|0\rangle_{m_s}$ and $|+1\rangle_{m_s}$ will be p_0 and p_{+1} respectively. With single-photon source efficiency, detection efficiency and cooperativity of 60%, 92% and 10 respectively, the photon bandwidth detection probabilities are $p_0 = 0.50$ and $p_{+1} = 0.00364$. We can estimate the error rates per pulse, as $\eta_0 = 1.5 \times 10^{-4}$ ($\eta_0 = 3.5 \times 10^{-4}$) for the $m_s = 0$ decay to the meta-stable subspace of 0% (1%) respectively with $\eta_{+1} = 1.2 \times 10^{-5}$. This means we can achieve an expected measurement fidelity of $F = 99.9\%$ ($F = 99.8\%$) using 13 (12) single photon pulses. Using more pulses than this decreases the resulting fidelity but at the levels indicated here we are right at the border of our 99.9% requirement.

At what pulse times does the error associated with false-positive detection events become significant? We can obtain a quick estimate by determining the error and the average number of additional trials that would need to be performed to distinguish between the two rates of reflection, assuming once more that the error follows an exponential decay. As above, the cooperativity is assumed to be 10, the source and detection probabilities are 60% and 92% respectively, and the $m_s = 0$ metastable decay rate is 1%. In the point-frequency case this approximation predicts a fidelity of 0.99775 after 11 trials (this is a more conservative estimate than the numerical

calculations represented in previous sections). Errors differing from this by 10^{-5}, 10^{-4}, and 10^{-3} occur when the pulse times reach 455 ns (requiring 11 trials), 115 ns (requiring 12 trials), and 24 ns (requiring 19 trials) respectively.

Understanding that the above is a conservative approximation, we can also ask what values for κ or for σ_t we would require to suppress reflection (rather than error) from the $|+1\rangle_{m_s}$ so that it is below our threshold of 0.1%. We find that either $\kappa = 2\pi \times 129$ MHz for the current pulse-time or $\sigma_t = 71$ ns for the current cavity decay rate (so that either is 2.58 times larger than its original value) satisfy this condition. Due to dephasing, for application to projective entanglement generation there is a fundamental tradeoff to be made between longer pulse times, related directly to σ_t, and the number of such pulses required, as influenced by κ through the cooperativity.

4.5 Weak Coherent Pulses

Our previous considerations (and in [282]) assumed the use of single-photon sources that are technologically challenging to realize and were found to be a key limiting factor in achieving higher measurement fidelities. Weak coherent laser pulses are a natural alternative [319] and offer a number of potential advantages including:

- Ready availability at the appropriate wavelengths,
- Easy tailoring of their mean photon number,
- Ready pulse shaping to customize the state dependent reflection/absorption from the cavity.

Allowing more than one photon to be reflected from the cavity dramatically improves our detection efficiency, potentially turning this into a single-shot (pulse) measurement. There is however a potential issue here associated with ionization of the NV center, which can occur when the electronic state absorbs more than one 637 nm photon. Ionization converts the NV^- center to the charge neutral NV^0 center (which is spin-0). Little applicable information is known about photo-induced ionization at this wavelength and temperature apart from the fact it must be a two-photon process [320–322].

Our situation here is different as we are working with an NV in a CQED configuration at low temperatures, which will enhance the light–center interaction. We do however know that the probability of photons being reflected from the cavity mirror on resonance is $P_R \approx 4C^2/(2C+1)^2$ and for a weak coherent laser pulse $|\alpha\rangle$ the mean number of photons in that pulse entering the cavity is $|\alpha|^2(1-P_R)$. We can then estimate that over time of the entire pulse τ_p, the probability P_{2+} of having two or more photons within the cavity's line-width $1/\kappa$ should be

$$P_{2+} \sim |\alpha|^4(1-P_R)^2\frac{\kappa\tau_p}{2} \sim 10^{-3} \tag{4.17}$$

for our typical parameters with $|\alpha|^2 \sim 3$. It is critical to remember that having two photons in the cavity does not that mean both are simultaneously absorbed and cause ionization. We can go a step further and calculate the probability that the NV center is in its ESM and that simultaneously at least one photon is in the cavity mode. The results of our master equation simulation are shown in Figure 4.7 and we immediately observe that this joint probability is nearly an order of magnitude lower than P_{2+}. Unfortunately we do not know the coupling rate between the ESM

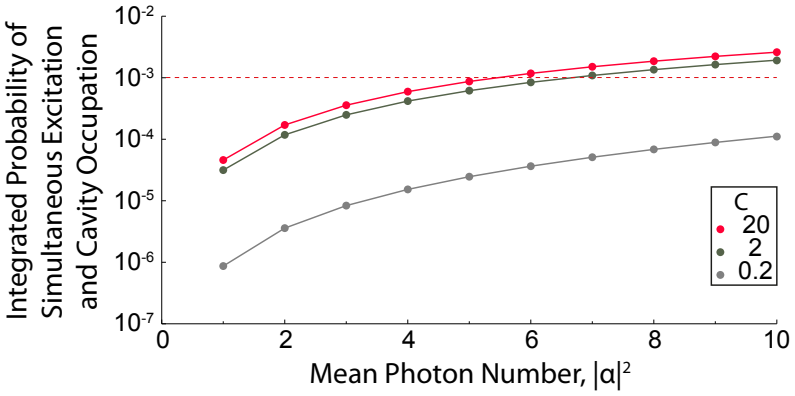

FIGURE 4.7: Plot of the joint probability of the NV center being in the excited $|M_4\rangle$ state with one or more photons present in the cavity, integrated over the time of a single pulse, as a function of the mean photon number of that coherent pulse. This probability will serve as an upper bound on the ionization rate of the center. Shown for cooperativity values C of 0.2, 2 and 20. As the cooperativity increases, the proportion of the cavity–center optical decay time for which the center is excited is increased.

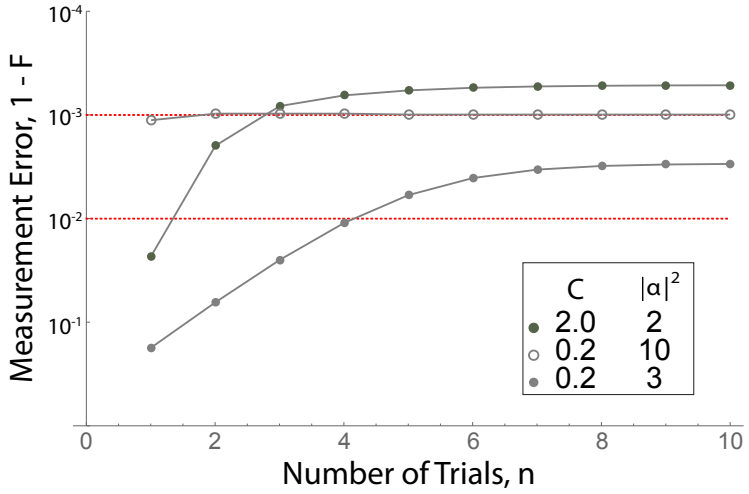

FIGURE 4.8: Loss of measurement fidelity, F, as function of the cooperativity, C, for a coherent light source and ideal detection, over a range of measurement pulses, n. The $m_s = 0$ decay rate to the meta-stable subspace is taken to be 1%. Three cases are shown: $C = 0.2, |\alpha|^2 = 3$ (light gray, dots), $C = 0.2, |\alpha|^2 = 10$ (light gray, circles), $C = 2.0, |\alpha|^2 = 2$ (dark gray, dots).

and the conduction band. However, based on these preliminary estimates, for reasonable values of C and $|\alpha|^2$ we expect that the ionization probability will be less than 10^{-3}, and that therefore weak coherent laser pulses should be ideal for initial measurement experiments. Performance estimates for several cases are shown in Figure 4.8. In addition to increasing the ionization rate, a higher photon number also increases the coupling between the cavity and center, as well as the effective detection efficiency. In fact, with $|\alpha|^2 \sim 3$, cooperativities in the strong coupling regime and current detection efficiencies we should be able to achieve a single-shot measurement. This measurement cannot be used for entanglement generation, however, due to the likely presence of additional scattered photons.

4.6 Discussion

The scheme investigated here uses a dipole-induced transparency to entangle the path of a photon with the spin state of a single nitrogen–vacancy center at cryogenic temperatures. This provides, through subsequent detection of such a photon, a projective measurement on the spin state of the center. The fidelity of this projective measurement forms the key figure of merit in our results. Typically, analyses of these approaches have used significant approximations (e.g. limiting the state space and assuming memoryless scattering distributions) to argue the initial case for their competitiveness, but it is important, before these devices are realized for scalable systems, to determine just how scalable they are. This requires a more in-depth and complete model. In our work here:

- The model of the energy level structure of the nitrogen–vacancy center incorporates all ground and optically excited states.
- Errors arising from evolution among optically excited states are considered, as well as the ability of the decay path through a meta-stable state to feed back into the correct subspace, when accounting for multiple single-photon pulses.
- We characterize the impact of external photon loss and variation in the decay rate to the meta-stable subspace.
- With the exception of Subsection 4.4.2, scattering probabilities are dependent on the outcomes of preceding measurement pulses.

Incorporating these effects allows us to begin to make statements about the applicability of this approach to real, large-scale systems.

Accounting for these additional factors, we expect that the two primary hurdles to the implementation of this scheme are the construction of high-fidelity, narrow-bandwidth ($\sigma_t \kappa >> 1$) single-photon sources and a cooperativity in the strong-coupling regime (recent work [312] reported a cooperativity $C \approx 0.2$). The preliminary use of few-photon, weak coherent pulses may circumvent the issue of the single-photon sources, and increases the effective cooperativity by increasing the electric field density. However, larger scale applications and projective entanglement generation between multiple color centres will require single-photon sources:

For the larger applications, charge-state switching and its correction will cause temporal inhomogeneous broadening [323], while for entanglement generation, the possibility of stray photons, avoidable only with large cooperativities and high detection efficiencies, degrades the resultant entanglement fidelity. Contemporary difficulties in mind, however, with continuing development we do expect the parameters assumed here for cooperativity (10), and source (60%) and detection (92%) efficiencies to be experimentally achievable in the near future; we intend our characterization of the impact of individual error sources to assist experimental efforts to engineer high-fidelity projective operations with this system.

To summarize our view for the immediate future, setting aside the challenges of large-scale applications and projective entanglement generation between nitrogen–vacancy center devices, we envisage that the preliminary use of weak coherent states should allow high-fidelity spin measurements in smaller-scale, contemporary settings. We have estimated an upper bound on the rate of charge-state switching for moderate photon-numbers on the order of 10^{-3}. This bound, along with the fidelities depicted in Figure 4.5, suggests that the measurement scheme considered here sees an error rate improvement of, in principle, an order of magnitude over the traditional method of luminescence-detection. While our estimates could be improved with a finer characterization of the ionization rate and the $m_s = 0$ decay rate through the meta-stable subspace, our results therefore suggest that dipole-induced transparency should provide high fidelity measurement of the spin state of the nitrogen–vacancy center.

Recent interest has also been generated around the *silicon*–vacancy center in diamond; this system has several apparent optical advantages, such as the strength of its zero-phonon line, over the nitrogen–vacancy center. We consider the silicon–vacancy center, comparing it with the above results for the nitrogen–vacancy center, in Chapter 5.

Chapter 5

Operations on the Negative Silicon–Vacancy Center in Diamond

The silicon–vacancy center in diamond has recently attracted significant attention as a candidate for quantum information processing as it overcomes many of the optical problems of the nitrogen–vacancy center. Historically it has been hampered by short dephasing times, however high-purity samples at low temperatures resolve this issue. Here we investigate the potential of the silicon–vacancy center to achieve optically two operations required for quantum information processing: projective measurement and population transfer.

5.1 Introduction

The silicon–vacancy center defect in diamond has been seen by many as a successor to the optically problematic nitrogen–vacancy center [324]. This center consists of a single silicon atom at the center of a split-vacancy, in the space left by the removal of two adjacent carbon atoms in the diamond lattice. The measured $\mathrm{O}(10-100\ \mathrm{ns})$ coherence times of the spin states of silicon–vacancy centers at cryogenic temperatures [325–327] were previously comparable to the period of the hyperfine interaction between the electronic and nuclear spin states in the ^{29}Si isotope ($\mathrm{O}(10-100\ \mathrm{ns})$ [325]). It was thus supposed that the silicon–vacancy center would not be a reliable system in which to store the state of a qubit; it was proposed as a source of single photons [328] due to its narrow, stable, optical transitions and strong zero-phonon line, though non-radiative decay is a dominant process reducing the quantum efficiency of optical transitions. More recently, however, investigations [329] have suggested that the coherence time of the silicon–vacancy center can be increased under conditions of low temperature ($10-100$ mK) with Sukachev et al. [330] reporting a T_2 time of 13 ms and a T_1 time exceeding 1 s.

Such findings cause us to reconsider the potential of the silicon–vacancy center for the encoding, processing, and measurement of qubit information. If information can, in fact, survive long enough to be reliably stored in the nuclear spin state of the ^{29}Si isotope, could the silicon–vacancy center provide a path around the optical complications of the nitrogen–vacancy center [295–298, 300, 301]? The apparent advantages of the silicon–vacancy center over the nitrogen–vacancy center relate to optical transitions; the potential to exploit these optical transitions for spin population transfer and measurement has been our immediate concern. Specifically, we investigate theoretically the fidelity of spin measurement mediated by cavity reflection

[8, 279–283] and of single-qubit manipulation using STIRAP [331] pulses through intermediate states in the optically excited subspace.

To summarise, the SiV center is known to bypass several optical complications of the NV center. Uncertainties remain in the centers dynamics, however, and the best implementations of quantum logic gates with this center remain unknown, though several approaches have been tried. The potential of the center for quantum information processing therefore remains uncertain. With these points in mind, we would like to answer the following question: Under optimistic assumptions, are optical gates with the SiV center likely to allow it to supersede the NV center?

This chapter is organised as follows: In Section 5.2 we begin with an overview of the properties of the silicon–vacancy center and the assumptions we make for our model. In Section 5.3 we explain our selection of external fields and the qubit subspace. Sections 5.4 and 5.5 respectively describe cavity-mediated measurement of the spin state and population transfer via optical STIRAP. Finally, in Section 5.6 we summarise our understanding of the potential of the silicon–vacancy center relative to the well-known nitrogen–vacancy center.

5.2 The Silicon–Vacancy Center

The model we use for the electronic energy level structure of the SiV^- center consists of four *optically excited states* (ES) and four lower-energy *ground states* (GS). These subspaces are respectively composed of two, two-level subsystems, associated with the spin and orbital angular momentum electronic states [325,332]. This energy level structure is displayed in Figure 5.1, where the GS and ES subspaces respectively are governed by the Hamiltonians

$$\begin{aligned}\hat{H}/\hbar = {} & \lambda^{(GS/ES)}\hat{S}_Z^{(o)}\hat{S}_Z^{(e)} + f\mu_B B_Z \hat{S}_Z^{(o)} \\ & + 2.0\mu_B \sum_{i\in\{X,Y,Z\}} B_i \hat{S}_i^{(e)} \\ & + \epsilon_I^{(GS/ES)}\hat{S}_Z^{(o)2} + \sum_{i\in\{X,Y\}} \epsilon_i^{(GS/ES)}\hat{S}_i^{(o)},\end{aligned} \tag{5.1}$$

and where $\hat{S}_{X/Y/Z}^{(o/e)}$ are spin-1/2 operators for the orbital (o) and spin (e) subsystems with the orbital operators containing an extra factor of 2 [327, 332]. Here $\lambda^{(GS)} = 2\pi \times 51.5$ GHz ($\lambda^{(ES)} = 2\pi \times 257$ GHz) denotes spin–orbit coupling, while $f = 0.1$ reflects an expected suppression of the magnetic field's influence on the orbital component due to a dynamic Jahn–Teller effect. $\mu_B = 2\pi \times 14.0\,\text{GHz}\,\text{T}^{-1}$ is the Bohr magneton, while $B_{X/Y/Z}$ are applied magnetic fields along each of the principal axes. Finally, $\epsilon_{I/X/Z}^{(GS/ES)}$ represent strain fields.

The ES lifetimes, appearing to be independent of the particular spin or angular momentum states, are set at 1.8 ns [333]. Optical transitions are divided by the symmetry of the center into axially polarised on the one hand, and circularly polarised components orthogonal to the principal axis of the center on the other. Orthogonally polarised photons flip the orbital angular momentum state in the transfer between the GS and ES subspaces, while axially polarised photons leave the orbital angular momentum state unchanged and are coupled twice as strongly [325,332].

There appear to be at least three primary sources of decoherence in the ground state subspace: thermal phonons, spin-spin interaction with impurities such as ^{13}C, and at least one other, unknown source [326, 329, 330, 334]. At temperatures on the

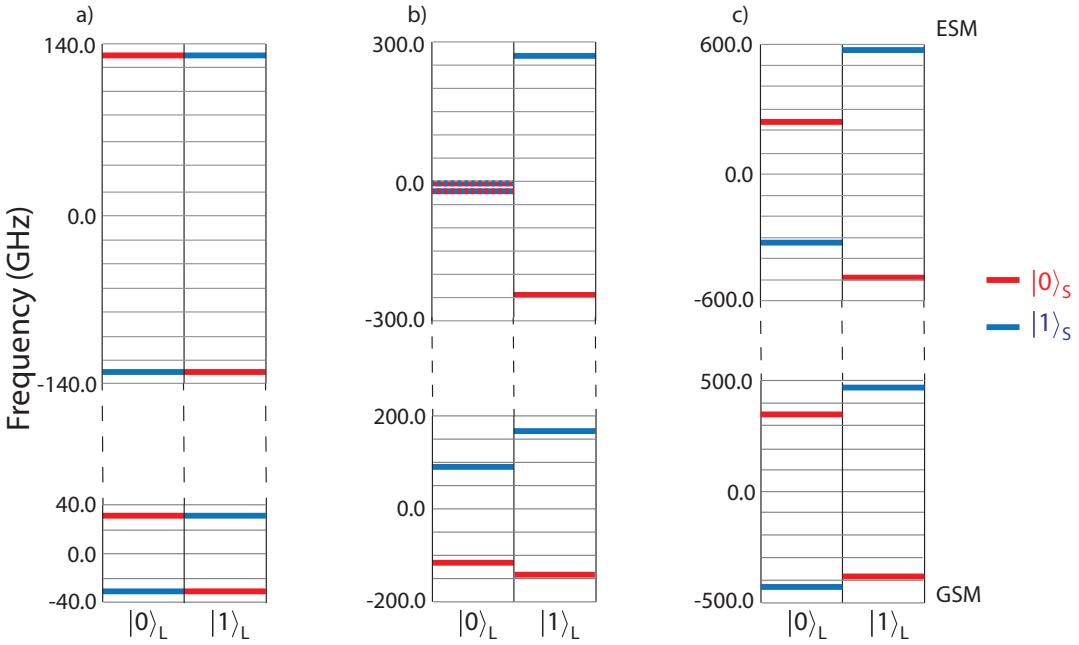

FIGURE 5.1: The energy level structure of the negatively charged silicon–vacancy center under the assumptions described in Section 5.2, for **(a)** zero magnetic field, **(b)** a magnetic field with $B_Z = 9.179$ T and $B_X = 0.6$ T, and **(c)** a magnetic field with $B_Z = 29.179$ T. The zero-phonon line of the negative silicon–vacancy center is 1.682 eV. All optical transitions preserve the spin state ($|\psi\rangle_S$, denoted by color), while Z-polarized optical transitions additionally preserve the orbital state ($|\psi\rangle_L$, denoted by column).

scale of the ground state splitting and above, decoherence is dominated by an Orbach process [327]. This process is limited by the excitation rate of the orbital component, and subsequent relaxation from the upper branch of the ground states appears to occur in the orbital and spin components respectively at a ratio of 100 : 1. The zero-temperature orbital and spin relaxation rates from the upper branch we infer [327, 329] to be 66 ns and 6.6 μs respectively. In what follows we will assume a regime in which the mean thermal photon number at the characteristic energy of the ground state splitting is much less than one ($T \leq 100$ mK). At such low temperatures, and for a high-purity diamond sample, the limiting decoherence rate at zero field is thought to be due to spin-spin coupling to impurities with T_2^* of order 10 μs [330].

We begin with a qualification: Not enough is yet known about the silicon–vacancy center to provide performance estimates at the level of precision required for scalable quantum information processing tasks. Here we deliberately take an optimistic view where we encounter uncertainty in the properties of the center, to clarify known limitations while leaving open the potential for fortunate refinement in the future. Specifically, our assumptions are: No static Jahn-Teller terms (these are wrapped into strain); no fluctuation, nor statistical uncertainty, in the dynamical parameters; no non-radiative decay from the optically excited states; no native decay terms with decay times greater than O(10 μs), which we justify by expected operation times; no nuclear (hyperfine) sublevels; and no additional energy levels around the optically excited states [325, 335, 336].

5.3 Qubit Subspace and External Fields

Before any claims about operational fidelity have meaning they must be related to a specific encoded qubit subspace within the energy level structure of the center. We have the following requirements for the selection of such a subspace:

1. Our two qubit states are long-lived;

2. transition energies between our two qubit states and respective optically excited states (where the transition polarisation is equal) are sufficiently distinct as to allow selective excitation from one state to another, both for cavity-mediated projective measurement and for population transfer mediated by these excited states;

3. the energies of the qubit states themselves must be sufficiently distinct from their equal-spin counterparts in the inverse orbital subspace to avoid overlap with single-qubit rotations mediated by the excited states and/or this inverse subspace.

To satisfy the first condition, long qubit lifetimes, we must first consider the dominant noise processes of the SiV^- center. The dominant decoherence process at low temperatures is a downward (emissive) relaxation of the orbital subspace. As noted in Section 5.2, we expect this process to have a decay time of 66 ns. The next dominant process is downward (emissive) spin relaxation, for which we expect a decay time of order $(100 \times 66\ \text{ns}) = 6.6\ \mu$s. Our first preference, then, is the lowest-energy orbital component associated with each spin component. If possible, we would also like to satisfy the inverse: that our qubit is encoded in the lowest-energy spin component of each orbital subspace.

We break the energy-level structure into three classes according to magnetic field magnitude:

- At small fields ($B_Z < 1.8$ T) the coherence times reach $T_2^* = 10$ μs and $T_2 = 10$ ms [330]. Population transitions in this regime are two-photon processes relying upon perturbative differences in spin composition between the qubit subspace and either the higher-energy pair of ground states or the lower-energy pair of optically excited states. See Figure 5.1 (a).

- At fields above approximately $B_Z \approx 1.8$ T, the two central ground states cross, so that the two most stable states become the first and third ground states in order of ascending energy. This has the effect of reducing the qubit lifetime to the emissive spin lifetime (6.6 μs). At an axial magnetic field of 9.179 T the central optically excited states can be brought together; while population transfer between qubit states remains a two-photon process, the creation of $|+\rangle$ and $|-\rangle$ spin configurations in the central excited states via the application of a small transverse magnetic field suggests the potential in this regime for single-qubit rotations via Stimulated Raman Adiabatic Passage (STIRAP). The appeal of a STIRAP approach is that it avoids optical excitation of the center, and therefore avoids the error channels associated with spontaneous optical decay (and also of non-radiative decay and unknown variation in the hyperfine coupling magnitude in the presence of a ^{29}Si nuclear spin). See Figure 5.1 (b).

- At fields of approximately 30 T and above, the two most stable states take on the same orbital degree of freedom (differing only in their spin component). In this regime population transfer therefore becomes a direct, one-photon process. The expected qubit lifetime, as for regime (2), is limited by the spin relaxation time to 6.6 μs. While this regime appears promising, the required constant magnetic field of order 30 T is, as far as we are aware, beyond normal experimental capabilities. See Figure 5.1 (c).

Excluding regime (3) because of its impracticable magnetic field magnitude, we next consider the relative strengths and weaknesses of regimes (1) and (2).

At zero-field, due to strong spin–orbit coupling, the requirements for a long qubit lifetime as described above are satisfied by the lowest-energy eigenstates:

$$|01\rangle_{L,S}\,; \quad |10\rangle_{L,S}\,. \tag{5.2}$$

Single-qubit rotations through the optically excited states via STIRAP additionally requires the ability to couple the two qubit states to the same excited state (or the same set of excited states). Engineering photon polarization can enable us to drive transitions toward the same orbital component. However, optical transitions are spin-conserving and the spin components remain distinct in the optically excited states due to strong spin–orbit coupling; at zero-field, population transfer through these states relies upon a relative perturbative mixing of the spin in the ground states. For STIRAP transfer, such perturbative mixing is insufficient; when overlap between the qubit states and the intermediate states are not equal, applying the Stokes' and pump pulses in the usual counterintuitive order is unable to suppress population transfer into the intermediate states. Population transfer into the intermediate states is a source of error because of the rapid and weakly-selective nature of optical decay. Spin mixing must be caused by a magnetic field orthogonal to the axis of the SiV^- center, because the strain field affects only the orbital components

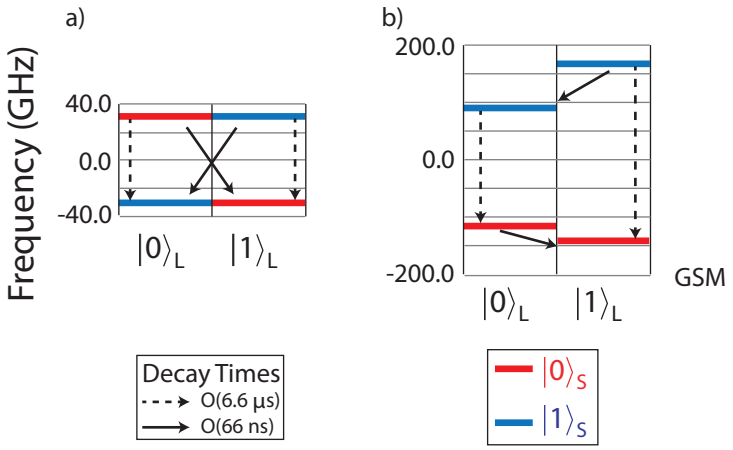

FIGURE 5.2: Relaxation processes affecting the negatively charged silicon–vacancy center, for the cases of **(a)** zero magnetic field, and **(b)** a magnetic field with $B_Z = 9.179$ T and $B_X = 0.6$ T. While the qubit lifetime in the zero-field case is limited by the slower rate of orbital excitation, for axial magnetic fields greater than $B_Z \approx 1.84$ T it is limited by the faster spin relaxation time.

[327]. We therefore seek to apply external magnetic fields to induce a relative mixing of the spin component in either the ground states or the excited states. Relative differences between the excited and ground states must be due to prior energy gaps between spin components in the same orbital subspace, as the magnetic susceptibility is the same for the excited and ground subspaces. Since strain does not affect the spin subsystem, these energy gaps will be caused by a combination of the natural spin–orbit coupling and a magnetic field aligned with the SiV^- axis.

Controlling this component of the magnetic field allows us to mix the relative spin components either by bringing two of the ground states together, at $B_Z \approx \pm 1.84$ T, or two of the excited states together at $B_Z \approx \pm 9.179$ T. Bringing the central ground states together forces us to encode the qubit in a high-energy orbital component, reducing the lifetime of the qubit to around 66 ns through orbital relaxation. Bringing the central excited states together inverts the order of the two central ground states, leaving the qubit with a lifetime limited to order 6.6 μs due to spin relaxation. We justify the latter, applying a magnetic field of $B_Z = 9.179$ T, $B_X = 0.6$ T, by the $O(10\,\text{ns})$ timescale of operations performed on the center necessary in the presence of a ^{29}Si nuclear spin qubit. The decoherence per operation is then $\leq 1\%$: smaller than the error otherwise associated with optical excitation and subsequent decay. These operations will be described in the sections to follow.

One immediate question is the potential role of strain terms in the Hamiltonian. When the strain terms are comparable to the spin-orbit splitting of the ground states, the orbital components of the two qubit states are no longer orthogonal. In such a case a direct transition can be driven between the states of the spin component, though this comes at the expense of a direct relaxation process between the two qubit states, decreasing the coherence time. This regime was investigated experimentally by Sukachev et al. [330] to achieve dynamical decoupling. A high-strain environment such as is explored in [327] might be used to manipulate optical transition detunings, in addition to raising the operating temperature. We have decided to leave these terms at zero. Strain terms strong enough to preserve the symmetry in transition overlap between the ground and excited states desired for the fast STIRAP pulses we are investigating would require a magnetic field two orders of magnitude

larger than the current figure (9.179 T). Such strong fields are not believed to be experimentally feasible at the current time.

5.4 Measurement and Initialisation of the Electronic Spin State

The most common means of measuring the spin state of the center has been by resonance fluorescence [325, 326, 329, 330, 334, 337, 338]. However, factors such as non-radiative decay and excited state hyperfine coupling make us hesitant to rely on pumped fluorescence as the primary means of measurement, due to its direct population of the excited states. Strong Purcell-enhancement can be used to mitigate population of the excited states by targeting even-order processes. However, using orthogonal transitions (as in the Purcell-enhancement of pumped fluorescence measurements) necessarily removes us from the qubit subspace. This primarily results in dephasing, which is not a problem where we are interested in spin measurement, but which prevents the application of such a scheme to projective entanglement generation. The alternative, achieving second order with the inverse transition, has the advantages of requiring lower driving powers (since both single-order components are enhanced by the resonator) and of maintaining population in the qubit subspace. Additionally, shelving does not occur in the higher orbital ground state, which is relevant when pulses occur on the timescale of the orbital decay time, $\mathrm{O}(66\,\mathrm{ns})$ or below.

For the SiV^- center, we can choose to target either an axially-polarised transition or a transition with circular, orthogonal polarisation. The axially-polarised transition has the advantage of a higher ratio of coupling to spontaneous decay by a factor of 2, and of probable return to the initial state on spontaneous decay at a ratio of $2/3$ [332]. We therefore discuss here only the axially-polarised case.

Unlike the nitrogen–vacancy center, the blinking that characterises charge-state switching is not typically observed for the SiV^- center on optical driving. This implies that we are free — for the purpose of spin measurement, though not for projective entanglement generation — to use coherent light sources. Coherent light sources allow us to account for inward-coupling photon loss, to tune the light near to resonance, to maintain longer pulse times (reducing photon bandwidth), and to increase the *effective* cooperativity of the atom–cavity system by increasing the electric field density.

We have established minimum pulse times according to other decay terms. Assuming a Gaussian pulse, a z-score of -2.5 covers 0.49% of the pulse area, so that 99% of the pulse lies within a width of 5.16σ. We will call this the *width* of the pulse. The pulse time is limited by the lifetime of the center and the minimum energy gap between optical transitions. In our particular case, there exist two levels either side of the target that appear to interfere destructively; shown in Figure 5.3 are example reflection probabilities from the target (red) and secondary (blue) qubit states. For the example in this figure, the target state achieves a maximum reflection probability of O(99%), the limit fidelity of a single-shot, single-photon measurement. The error channel due to scattering is relatively insensitive to the bandwidth of the pulse, so as a rough bound on the frequency-bandwidth we take the minimum width at which the transmission or reflection probabilities diverge from their extremal order. With the aim of maximising the reflection contrast between the two qubit states, we therefore take $2\pi \times 0.71$ GHz as the rough upper bound on the total frequency width of

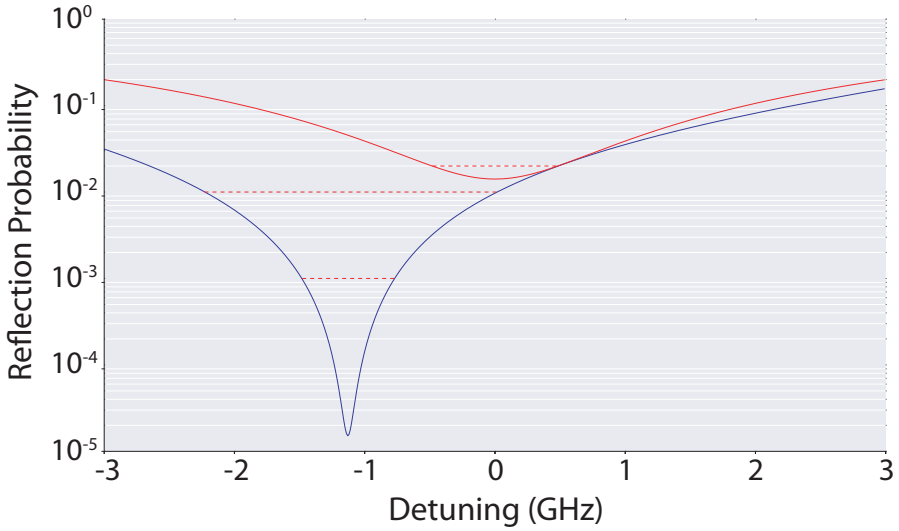

FIGURE 5.3: Example complement of the single-photon reflection probability curve from the target (red) state and the reflection probability for the secondary (blue) qubit state as functions of the center–cavity detuning. For this figure only, the incident field and cavity mode are resonant, the cavity mirrors are balanced, and the center–cavity cooperativity is 70. The peaks from the secondary qubit state appear to interfere destructively to suppress reflection close to the target transition. Units are expressed in pure frequencies.

the pulse, obtaining

$$\sigma_f \leq \frac{2\pi \times 0.71\ \text{GHz}}{5.16} = 2\pi \times 0.13\ \text{GHz} \tag{5.3}$$

$$\sigma_t \geq \frac{1}{2\sigma_f} = 0.58\ \text{ns}. \tag{5.4}$$

If the time of a pulse is $5.16\sigma_t$, we then have a rough lower bound on this time of $T_{Pulse} = 5.16\sigma_t \geq 2.98$ ns.

When it comes to using cavity-enhanced detection for projective entanglement generation, the greater the mean photon number at the input, the lower the final state fidelity due to the possibility of the loss of stray entangled photons. For this reason, sources with narrow photon number distributions and high-efficiency optical channels and detectors will be necessary. We now turn from a single, multi-photon coherent pulse to look at multiple single-photon pulses. Setting the initial state to a 50–50 mixture between qubit states, we have calculated the operational fidelity of a reflective cavity-assisted measurement of the spin state of the SiV^- center.

We have used a scattering approach as in Section 4.3. This relies two main assumptions: photon populations from pulses in succession do not interfere with one another and the bandwidth of the driving field is small. For decay on the order of the optical lifetime, 1.8 ns, 0.67% of the population will remain for an inter-pulse time of 10 ns and 4.5×10^{-3}% for an inter-pulse time of 20 ns. We have chosen 20 ns, bounding the maximum number of probe pulses to O(10) through the error associated with the spin relaxation time. That the inter-pulse time is an order of magnitude larger than the minimum width of 2.98 ns derived above justifies the assumption of a small bandwidth.

TABLE 5.1: Measurement fidelity with varying cooperativity, C, and the single-photon source and detection efficiencies, η_{Source} and η_{Detect}, as well as the number n of pulses. The pulse number is chosen to maximise the fidelity.

C	η_{Source}	η_{Detect}	n	F
1000.0	1.0	1.0	1	0.9645
100.0	1.0	1.0	1	0.9899
10.0	1.0	1.0	2	0.9785
2.0	1.0	1.0	4	0.9224
1.0	1.0	1.0	6	0.8687
1000.0	1.0	0.5	4	0.8533
100.0	1.0	0.5	6	0.9611
10.0	1.0	0.5	8	0.9526
2.0	1.0	0.5	9	0.8628
1.0	1.0	0.5	9	0.7912
1000.0	0.5	1.0	5	0.9061
100.0	0.5	1.0	7	0.9730
10.0	0.5	1.0	8	0.9679
2.0	0.5	1.0	11	0.9117
1.0	0.5	1.0	13	0.8573

Results are displayed in Table 5.1 and in Figure 5.4. The chief limitation discovered was scattering to alternate states; this caused temporary leakage to higher-energy ground states. Such leakage results in significant dephasing, which is not an issue for spin measurement, but also a non-negligible probability of spin-flip transitions. Maximum measurement fidelities of order 99% are found for a cavity cooperativity of order $50 - 100$ when ideal sources and detectors are assumed. When photon loss is allowed to affect these devices, the fidelity drops to order 96% with an increased number of single photon pulses.

5.5 Population Transfer between Spin States

Beginning with population concentrated in the lowest-energy ground state, we would like to create a coherent superposition between the two qubit states using optical or microwave pulses. Optical and microwave pulses may be applied in the resonant regime, or may be far detuned. The former, a resonant transition, leads simply to Rabi oscillations at a frequency determined by the area of the pulse. However, as the encoded qubit states differ both in spin and orbital angular momentum components, this transition must be a second-order (two-photon) process. The latter case, using far-detuned pulses, gives rise to Raman-type schemes, which make use of a combination of independently detuned pulses to achieve resonant beat frequencies. These detuned schemes require unpopulated intermediate states. Such intermediate states may be chosen from either the ground or optically excited subspaces, so long as the appropriate transitions between the intermediate and target states are allowed.

We simulate coherent population transfer via STIRAP by numerical integration of the master equation, where Linblad terms include O(1.8 ns) optical decay, O(66 ns) ground state orbital decay, and O(6.6 μs) ground state spin decay. Following [339], Stokes and pump pulses are Gaussian, have the same width and magnitude, and

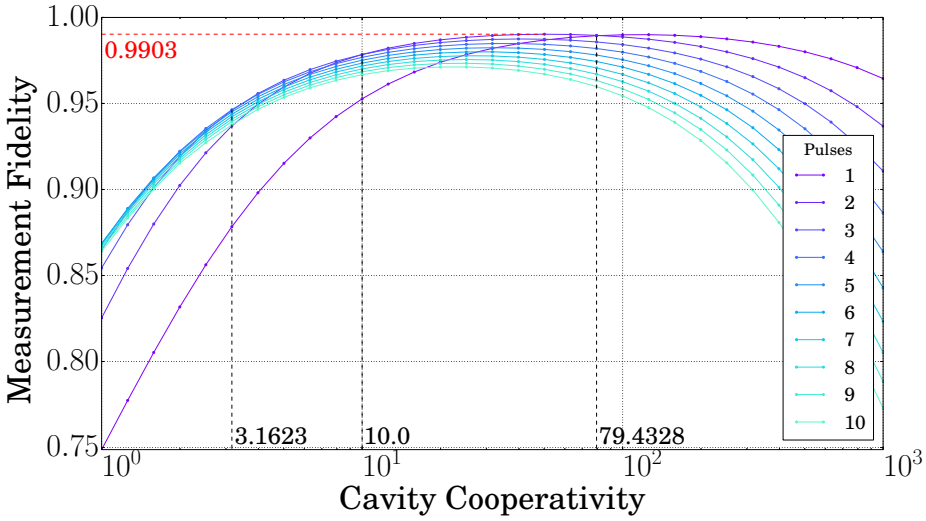

FIGURE 5.4: Measurement fidelity as a function of the cooperativity and the number of single-photon pulses. Identified in red is the maximum observed fidelity, 0.9903. Also identified, with black dashed lines, are the cooperativities where 1 pulse exceeds 2 at 79.43, 2 exceeds 3 at 10.0, and 3 exceeds 4 at 3.16.

are separated by one standard deviation. Frequencies and polarizations are chosen resonant with the target transitions.

Because the spin state of the center does not change under optical excitation, transfer between the qubit states must be involve a set of at least two intermediary states composed of a coherent spin superposition. One principal limitation of population transfer via STIRAP is therefore the separation between these two (symmetric and anti-symmetric) intermediary states; this separation, along with the requirement that the applied pulses match their amplitudes to the relative amplitudes of the spin components in each state, defines an upper limit on the characteristic timescale of the transfer. Above this limit, which is of order $2\pi \times 10$ GHz, the overlap between pulse widths begins to induce rapid oscillations in the transfer curve; destructive interference caused by overlap of the first pulse with the second reduces the population transfer and therefore the fidelity.

Further, in the specific case of the SiV^- center, as the driving amplitude increases or as the total time of the pulse decreases the Stokes' pulse begins to overlap with a transition from the initial qubit state. This transition populates the lowest-energy optically excited state, resulting in rapid optical decay that causes dephasing and lowers the rate of transfer. We find the best performance with a maximum pulse amplitude (Ω_{max}) at approximately 1% of the detuning between the pulse energy and the energy of this undesirable transition. The population dynamics for this STIRAP approach are shown in Figure 5.5. The degree of transfer is limited to order 90% by population transfer to excited states, and subsequent rapid spontaneous decay to the ground states. Further increasing Ω_{max} increases this transfer to the excited states, while decreasing Ω_{max} lowers the population transfered to the final qubit ground state.

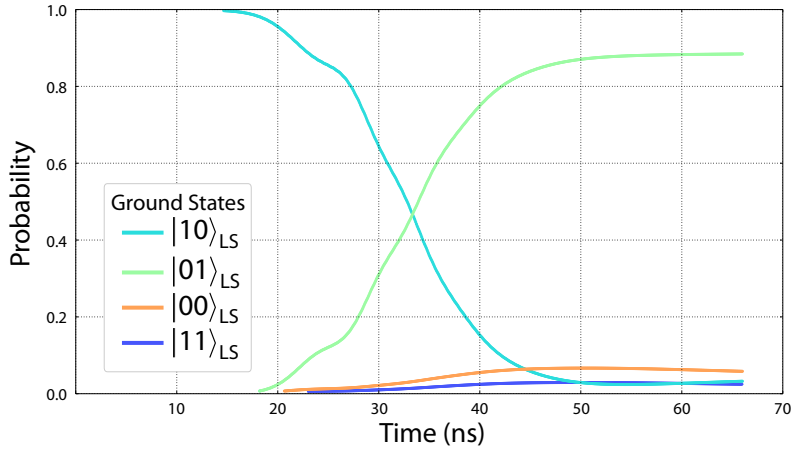

FIGURE 5.5: State populations as a function of time under STIRAP tranfer via the two central optically excited states. Initial (light blue) and target (green) states have been labelled by orbital and spin components. Erroneous transfer to the excited states results in population of the non-qubit ground states (orange and dark blue). The fidelity of the final state is of order 90%. The pulse time, t_{max}, was chosen at 66 ns to limit spin relaxation to $\leq 1\%$, and the maximum pulse amplitude, Ω_{max}, was set to approximately 1% of the detuning between the pulse energy and the energy of the two erroneous optical transitions (*approximate* because the detunings for the two pulse components differ slightly).

5.6 Discussion

Having considered optical spin measurement and population transfer with the silicon–vacancy center in diamond, we conclude with three points: There is a trade-off between the lifetime of the qubit and the rate and fidelity of STIRAP population transfer; cavity-mediated measurement can be performed in $O(20)$ ns with an error rate of order 1%; and population transfer between encoded qubit states can, in principle, be achieved in $O(66)$ ns, with a fidelity of order 90%.

It might be asked whether the spin measurement of Section 5.4 could be improved if the magnetic field were not tuned to allow for the STIRAP pulse of Section 5.5. The spin measurement was found to be limited by relative transition detunings and by rapid decay to non-qubit ground states. Because the magnetic susceptibility of the spin is equal for the ground and excited states, and because the magnetic field is not thought to change excited state lifetimes, these limiting factors too remain unchanged.

Having simulated estimates for the fidelity of coherent population transfer via optical STIRAP and of spin measurement mediated by cavity reflection statistics, we find that these fidelities do not surpass those of the nitrogen–vacancy center [8, 340]. Nonetheless, the speed with which projective measurements can be performed — roughly an order of magnitude faster than equivalent measurements with the nitrogen–vacancy center — suggests that the silicon–vacancy center might yet be usefully applied to efforts in quantum communication, where the strict error rate requirements of fault tolerant quantum computation need not necessarily apply. How such a module might operate, we consider using the example of the nitrogen–vacancy center in Chapter 6.

Chapter 6

A Universal Quantum Module for Quantum Communication, Computation and Metrology

In this section we describe a simple module that could be ubiquitous for quantum information based applications. The basic module is comprised of a single NV^- center in diamond embedded in an optical cavity, where the cavity mediates interactions between photons and the electron spin (enabling entanglement distribution and efficient readout), while the nuclear spin constitutes a long-lived quantum memory capable of storing and processing quantum information. We discuss how a network of connected modules can be used for distributed metrology, communication and computation applications.

6.1 Introduction

There are a wide range of candidate systems/technologies competing to implement quantum information processing tasks. They can be broadly compared according to operational control fidelities, coherence times divided by average operation times (where these are characteristic times for a specific problem considered), operating temperatures, fabrication reliability (scaled by time and repetition cost), connectivity with other device components (perhaps telecom fiber or the more general scaling and complexity of large systems), and finally fabrication suitability to the task at hand (including robustness to perturbation, size and symmetry). Some of these candidates include quantum dots, trapped atoms and ions, or defect centers in silicon and diamond. The module we propose here as the basis for distributed quantum technologies consists of a single, negatively-charged nitrogen–vacancy center in diamond (with ^{15}N isotope) embedded in an optical cavity. Here we discuss the potential in the near future of such a module for many quantum information processing tasks.

To summarise, the NV center in an optical cavity has previously been proposed as a universal primitive quantum structure. Here, our measurement performance estimates from Chapter 4 can be readily adapted to projective entanglement generation. Noting this, we would like to answer the following question: What can such an adapted entanglement generation rate tell us about the potential of an NV photonic module for near-term targets of memory-assisted quantum communication and sensing, and about the longer-term goal of large cluster state generation?

This chapter is structured as follows: In Section 6.2 we describe the basic operation of the module and some important parameters, while in Section 6.3 we describe

why we chose NV centers for the analysis in this chapter, in contrast to the silicon–vacancy centers of Chapter 5 or the related germanium–vacancy centers. In Section 6.4, we will describe an immediate application of the proposed NV–cavity device for quantum repeaters in a quantum communication system. Following this we will in Section 6.5 discuss those aspects of quantum metrology to which we expect the device to be applicable, and provide a ball-park estimate of the performance. Finally in Section 6.6 we discuss the benefits of distributed schemes to quantum computing architectures, and estimate what we might require of the center to reliably construct cluster states as the basis for quantum error correction codes or full measurement-based computation. The discussion will center heavily on the success rate of probabilistic entanglement generation, an important quantity for distributed quantum information processing.

6.2 The NV–Cavity Module

The nitrogen–vacancy center consists of a single nitrogen impurity adjacent to a vacant site in a diamond lattice. When an additional electron is absorbed, the center is stable with 11 known accessible levels as shown in Figure 4.1. While fabrication procedures for diamond have not reached the maturity of those for silicon-based devices, advances in isotropic purification and atom implantation enable the fabrication of such single centers in bulk diamond with a surrounding ^{13}C impurity density of only 0.3% [267] of atoms in the surrounding lattice and sample lattice strains with an energetic impact on the ground state of only $2\pi \times 1$ MHz [287]. Coherence times of the electronic state on the order of $10 - 100$ ms are possible [267,341]. Meanwhile, as mentioned in Chapter 4, local operations on the electronic state of the NV center have been achieved with fidelities as high as 0.99995 [178], and rotation of the electronic state can be performed in times on the order of 5 ns. For the ^{15}N isotope, a long lived spin-1/2 nuclear system is also present, with coherence times on the order of 1–10 s [268]. For the nuclear state we expect fidelities of general local operations of order 0.99 to be possible in times of order 1 μs. Importantly however, a CPhase gate with the electron spin is expected to be achievable with a fidelity greater than 0.999 on the order of 100 ns [340].

When the nitrogen–vacancy center is aligned at the focal point of an optical cavity, and that cavity is tuned to be resonant with the transitions between the $m_s = 0$ ground state and the E_X, E_Y excited states, the NV–cavity system may form dressed states that change the reflectivity properties of the composite system. We investigated the utility of this system in Chapter 4 for projective electronic spin measurement, and expect the measurement of the electronic state of the nitrogen–vacancy center to be possible with operational fidelities on the order of $F = 0.999$ in times on the order of 100 ns.

The correlation between the photon's path and the NV center state also allows projective entanglement generation using beam splitters to erase which-path information following a photon's interaction with either of two NV–cavity systems. For long communications channels, photon loss is expected to be the dominant source of error. As described in Chapter 4, loss between a single-photon source and an NV-cavity system, and between an NV–cavity system and a single-photon detector (including coupling losses) are two potential sources of loss. For long communications channels, we also expect loss events to occur as we up-convert the frequency of the transmitted photon to telecommunications wavelengths, and as the photon traverses the channel. We expect the performance of this projective entanglement

generation can there be very roughly estimated by the approximate probability of success

$$P_{ent} \approx \frac{1}{8} P_R(C) P_{Detect} P_{Source} P_{Up-Convert} e^{-\frac{L}{L_0}} \approx 0.03 e^{-\frac{L}{L_0}} \tag{6.1}$$

where $P_R(C = 2.0) \approx 0.64$ is the reflection probability of a photon from the NV–cavity system when the NV center is in the $m_s = 0$ state, $P_{Detect} \approx 0.9$ is the detection efficiency, and $P_{Source} \approx 0.6$ is the single-photon extraction rate of the source. These parameters are as assumed in Chapter 4. In addition, we assume $P_{Up-Convert} \approx 0.7$ is the conversion efficiency to the resonant frequency of the center, while the factor of 8 is unavoidable in the scheme we consider and arises from post-selection on the center state and photon path. Finally, the term $e^{-\frac{L}{L_0}}$ accounts for exponential photon attenuation along the length of the communication line, where $L_0 \approx 25$ km for optical fibre and photons at telecommunications wavelength.

The fidelity of this resultant entanglement is affected by the dark-count rate, decoherence of the NV centers while photons propagate through the channel and while awaiting necessary classical signaling, as well as the operational fidelities of initialization and electron rotation. The limiting factor is expected to be initialization, which shares the operational fidelity of measurement of 0.999, resulting in very high fidelity entangled states when the correct outcome is heralded. The time to reinitialize the electron state after each entanglement attempt takes on the order of 100 ns, the time to perform a projective spin measurement as described in Chapter 4 (the single-qubit rotation required to exclude the $|-1\rangle_{m_s}$ spin state is expected to take much less time [340]), so that the expected time to create one entangled pair is on the order of

$$E\left[T_{ent}\right] \approx 3 \times e^{\frac{L}{L_0}} \, \mu\text{s}. \tag{6.2}$$

With these estimates, we will now turn our attention to the use of the module in quantum communication tasks.

6.3 Silicon– and Germanium–Vacancy Centers

Not as much is known about the silicon–vacancy (SiV) and germanium–vacancy (GeV) centers in diamond as about the NV center. Nonetheless, we can use the information that is available to make educated guesses about the utility of such systems for quantum technologies. These centers have a much simpler energy level structure than the NV center, with much larger energy gaps. With the exception of a reversal in the order of the optically excited state energies, the SiV and GeV centers are expected to be very similar; we therefore address only the SiV center, previously considered in Chapter 5, below.

From the perspective of optical manipulation, we identify two major differences between the SiV center and the NV center:

- the first is that every optical transition of the SiV center forms part of a lambda-like structure, in that any optically excited state can be reached from more than one ground state, depending on the polarisation of the exciting photon.
- the second is that the zero-phonon line is much stronger for the SiV center ($\approx$ 70% of radiative decay) than for the NV center ($\approx$ 4%), though the non-radiative component of the decay is less certain.

The relation between the vaccum-Rabi coupling to a cavity mode and the radiative spontaneous decay rate is given by

$$g \propto \sqrt{\gamma f}, \tag{6.3}$$

where f is the proportion of spontaneous decay to the resonant zero-phonon line, and γ is the total spontaneous decay rate. At the low temperatures required to use SiV centers with reasonable coherence times ($\approx$ 100 mK [329]), the non-radiative decay rate is not known precisely, but certain estimates have not been able to distinguish it from zero [329,342], so that it is likely samples exist where the non-radiative decay rate is between zero and the order of the decay rate of the zero-phonon line. We therefore take $f \approx 0.5$, and estimate that the cavity-cooperativity, $C \propto g^2/\gamma$ (where γ is the total spontaneous decay rate), will be roughly 10 times larger for the SiV center than for the NV center. Purcell enhancements on the same order have already been achieved [312, 342]. However, the pervasive lambda structures and small excited state lifetimes together indicate that any cycling optical transition will be weaker for the SiV center, requiring Purcell enhancement of the resonant transition exceeding the alternative radiative decay path by several orders of magnitude. We expect that high fidelity optical operations, such as measurement, could therefore be difficult to perform. This suspicion is consistent with the results of Chapter 5. With a view to longer term developments, we restrict the remainder of this chapter to a consideration of the NV center photonic module.

6.4 Quantum Communication

Quantum communication involves the distribution of information with coherent (quantum) correlations between multiple spatially separated parties. The number of such parties is usually restricted to two, known colloquially as *Alice* (A) and *Bob* (B). Quantum teleportation further allows us to reduce the general problem of information transmission to the generation of entangled states (most commonly Bell-pairs). Whether we require these Bell-pairs to be generated with high fidelity, at a very high rate, or both depends on our specific application. In general, however, the performance can be separated into either those parameters corresponding to the method of distribution or those parameters corresponding to the physical construction. Assuming the use of frequency conversion to translate between the frequency of the optical zero-phonon line of the NV center and photons of telecommunications wavelength before transmission, only the physical construction is directly determined by the NV–cavity device. Here, we therefore consider the device's performance only when the method of distribution is restricted to a single-node heralded scheme proposed in the context of memory-assisted measurement-device independent quantum key distribution [343]. Importantly, the mechanism for projective entanglement generation that we assume [282] differs from that of the proposal in [343] and results in an error model dominated by dephasing when dark counts are low. This scheme is shown schematically in Figure 6.1.

The protocol for the single-node heralded scheme we consider, the circuit for which is shown in Figure 6.2, may be divided into "chunks" consisting of contiguous deterministic operation sets. The key rate will be restricted by the time of the largest of these chunks, when errors are negligible. The wait times are the operating times of: initialization, photon-atom interaction, and measurement. Initialization may be governed by a combination of measurement and pi-pulse times, or it may be subject

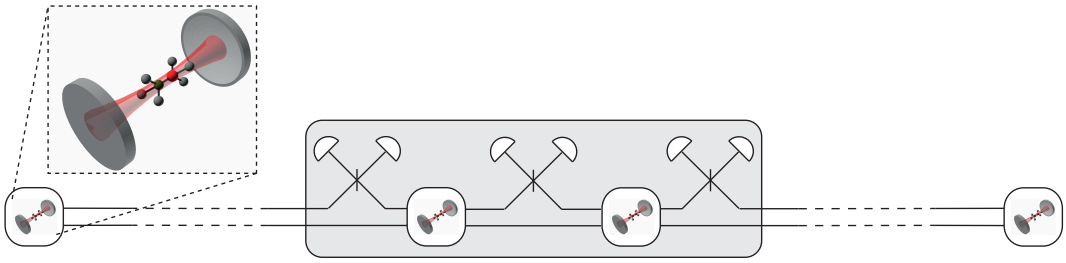

FIGURE 6.1: Schematic diagram of the single-node, heralded, memory assisted quantum communication scheme [343] we consider in Section 6.4. Single-photons are sent from the nodes at the left and right, possibly entangled with long-lived qubits at those sites. The central, composite node consists of two long lived qubit devices and three optical circuits for performing Bell measurements. The outer Bell measurements herald the *loading* (or equivalently, entanglement) of the two central qubits with the incoming signals. Once both qubits are loaded, a final central Bell measurement (or entanglement swapping operation) is performed between them, and the result reported to the external parties.

to a "polarization time" (i.e. the time to reach a pointer state, under continuous driving).

A natural first application is quantum key distribution where the *secret key rate* expressed in the form

$$\begin{aligned} \text{Secret Key Rate} &= (\text{Distribution Success Rate}) \qquad (6.4)\\ &\quad \times (\text{Bits of Information Remaining After the Channel}) \\ &\approx \frac{\prod_{i\in\text{Probabilistic Operations}} P_{\text{success},i}}{T_{\text{Slowest Operation}}} \times (1 - H(\text{Total Error Rate})) \qquad (6.5) \end{aligned}$$

determines the device's performance. Here T is the time of the slowest operation in the circuit, P_i the success probabilities of probabilistic operations, and $H(\cdot)$ the binary entropy function. This performance is initially dominated by the distribution success rate, which may be further decomposed and attributed to a bottleneck repetition rate (for some limiting deterministic operation) and the cumulative success rates of trailing probabilistic operations. The bottleneck repetition rate as a function of the channel length is subject to an initial offset attributable to local gate times, but is subsequently determined by exponential attenuation in the optical fibre that increases the average time-to-connection. For finite coherence times, at even larger distances this attenuation is dominated by decoherence, reducing the bits of information remaining in the signal, which typically factors into the equation in double-exponential form.

As we know that the attenuation rate will scale more slowly for a repeater-based scheme than for direct transmission, we want to identify the distance at which the decoherence effect becomes comparable to the effect of attenuation in the optical fiber. This *critical distance* is the channel length at which the rate of change of the key rate (Equation (6.5)), with respect to decoherence, approaches the same order of magnitude as the decay rate due to the signal attenuation term. The attenuation length is same regardless of the particular device technology. We identify the probabilities in the numerator of Equation (6.5) with the probability of entanglement

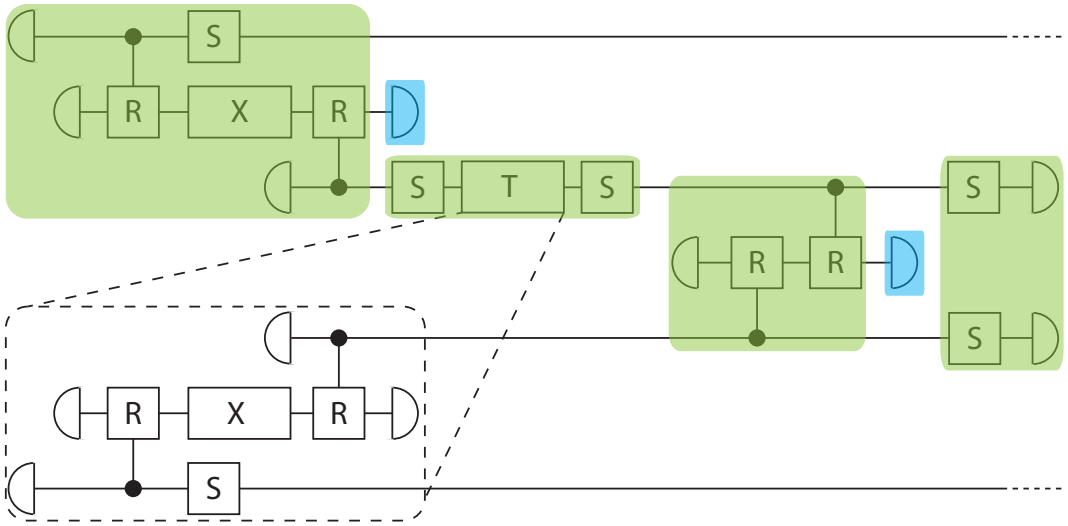

FIGURE 6.2: The protocol for the quantum communication scheme we consider in Section 6.4, divided into deterministic "chunks" (green) and probabilistic operations (blue). Operation labels denote: Left semicircle, state initialization; S, the swap operation between electron and nuclear spins in a single NV–cavity module; R, the conditional reflection of a photon from an NV–cavity module; X, the transfer of a photon to the central node (see Figure 6.1); T, storage in one memory at the central node while waiting for the other to be loaded; right semicircle, measurement (in the Z-basis for NV–cavity modules). The most time consuming operation is the wait for the second memory to be loaded. Here the upper (lower) rail corresponds to the NV center system of the first (last) party, either Alice *or* Bob, to achieve entanglement with a central memory. The third and fifth rails correspond to the NV center systems of the central memories closest to the first and last parties to achieve entanglement respectively. The second, fourth and fifth rails correspond to the photon modes in the optical fibre that become entangled with the NV center systems following conditional reflection.

generation found above and appearing in two locations in the circuit of Figure 6.2, and the slowest operation with entanglement generation between the second party and the second central memory. Under the assumption that dark count rates are low and therefore dephasing dominates the error term in Equation (6.5), we then take the derivatives of Equation (6.5) with respect to decoherence and attenuation respectively. Requiring that these two rates of change are approximately equal, we find the resultant condition to be

$$\frac{-1}{L_0} \approx \frac{-\log_2\left(\frac{e_z}{1-e_z}\right)\frac{e^{-\tau/\tau_c}}{2\tau_c}\frac{\tau}{L_0}}{(1-H(e_z))}, \tag{6.6}$$

where $e_z := \frac{1-e^{-\tau/\tau_c}}{2}$ quantifies decoherence due to dephasing, τ is the time taken for the entanglement distribution, and τ_c is the dephasing time. We estimate the $L = 0$ offset in the key rate to be on the order of 2000 bits per second, accounting for the expected times of both entanglement distribution and swap operations between electronic and nuclear spins. A total parameter of interest, which we can use to directly compare the key rates under different conditions on a semi-log scale, then becomes the difference between this circuit offset and the product between the attenuation rate and the critical distance defined by Equation (6.6).

For direct transmission, we assume a 50 MHz source. Here we simply assume that an NV center photonic module is used as the single-photon source, to keep the compared devices consistent and for proof-of-principle applications, and allow 200 ns for transmission and reinitialisation. In a comparison of direct transmission with the single-node scheme based on the secret key Equation (6.5), depicted in Figure 6.3, initially the direct transmission is better, but we find a crossover between the rates of the two options at approximately 508 km. When the nuclear spin coherence time is 1 s, the critical distance for the single node scheme is 596 km, and for a 10 s time it is 712 km. In the intervening region the possibility exists to demonstrate a secret key rate advantage by including a central repeater node. These points are only indicative, not exact, due to the approximations we have made to the circuit time and error rate.

As described in the preface, quantum key distribution is a potential near-term stepping stone motivating the development of single-photon sources and detectors, but for more general applications we would like the distribution of entangled states. Noting that the Bell-State measurement in the center of the scheme is an entanglement swapping operation, we can modify the key-rate formula to obtain a rough estimate for the rate of creation of entangled pairs. This is done by decreasing the effective coherence time to account for state components stored by Alice and Bob at the end nodes. While the density matrix remains diagonal in the Bell-state basis, the component of Equation (6.5) quantifying the remaining bits of information corresponds to an upper bound on the distillable entanglement [344]. The *secret key rate* then estimates the distillable entanglement generated per unit time, and the resultant pairs can be purified. In this case, rather than a 50 MHz source, the direct rate depends upon entangling remote NV centers, and is therefore limited by the time-to-connection (Equation (6.2)). This new rate ($\approx$ 0.3 MHz) reduces the crossover point to 256 km. The offset does not change, but the critical distance is decreased; for a nuclear coherence time of 1 s the critical distance becomes 562 km and for 10 s it becomes 678 km. These relationships are depicted in black in Figure 6.3.

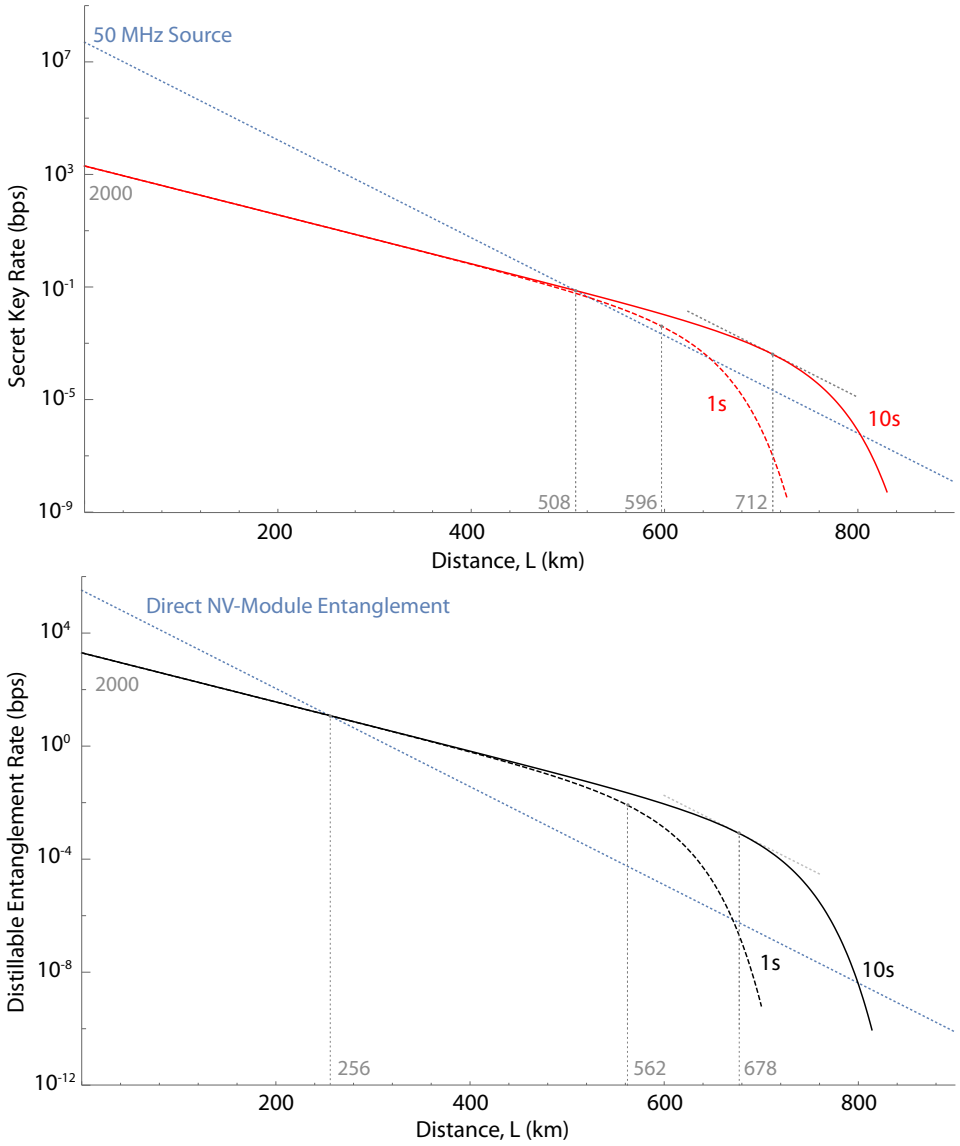

FIGURE 6.3: The approximate secret key (top, red) and distillable entanglement (bottom, black) rates derived from Equation (6.5), next to the estimated rate for direct transmision (blue, dotted). Nuclear spin coherence times of 1 s (dashed) and 10 s (solid) are shown. The *critical distances* for each curve are identified by gray dotted lines approaching the axis, at 562, 596, 678, and 712 km, and the *crossover* points at 508 km and 256 km. The *offset* point is also labelled at approximately 2000 bits per second. Gray dotted line segments follow the slope of direct transmission through the critical points at 678 km 712 km, to guide the eye and emphasize the matching gradient. Plots are kept distinct to avoid confusing overlap between the similar, but distinct, rates of key distribution and entanglement generation using the memory-assisted scheme.

6.5 Quantum Metrology

The use of devices amenable to quantum coherent control to enhance the precision of measurements is broadly called quantum metrology. The problem of quantum metrology can be divided into two facets, relating to the two types of advantages offered. The first is the potential to manipulate the rules of quantum mechanics to achieve single-trial sensitivities beyond those attainable with classical probes. This includes squeezing and entanglement-based improvements as discussed in Chapter 2. The second is a decrease in the size and increase in the sensitivity of the probes used (atomic scales). The size and sensitivity question, for example, is the primary driver in applications of quantum metrology in a biological setting. We do not expect the NV–cavity module we propose to be useful in this latter class of problems. The reasons are several: the temperatures required, often up to room temperature, are larger than our restriction of operating at cryogenic temperatures; the size of the cavity is likely to be on the order of micrometers or even millimeters, which is much larger than the nano-scale frontiers of this problem; finally, in certainz perturbative settings such as biological environments, the cavity structure and the target optical transitions of the nitrogen–vacancy center will not be rotationally symmetric and are unlikely to have stable frequencies. With these issues in mind, we turn to the latter type of target for quantum metrology: preparation of non-classical states. For us this means entanglement generation between separated modules and the application of quantum error correction, and we restrict the discussion to field sensing under the circuit depicted in Figure 6.4.

When the time available to perform repeated measurements is long, as is typically assumed, and in the presence of Markovian noise, entanglement does not provide any advantage with respect to parameter estimation (see Subsection 2.2.2). However, when the time available to perform a measurement is short, as when characterising a periodic process with high-frequency components, using an entangled state can reduce the sampling time and thus increase the Nyquist frequency of the measurement.

$$\frac{\left(|0\rangle^{\otimes N} + |1\rangle^{\otimes N}\right)}{\sqrt{2}} \rightarrow \frac{\left(|0\rangle^{\otimes N} + e^{i\left(\sum_{i=1}^{N} B_z^i\right)t}\,|1\rangle^{\otimes N}\right)}{\sqrt{2}} \tag{6.7}$$

Additionally, using entangled states in a distributed fashion allows us to directly measure spatial averages. Such averages over a distributed region could help to suppress or at least stabilise the impact of spatially-local noise. The suppression of local noise relates to the multiplication by N of a single random process versus the sum of N independent processes. For Gaussian noise, the former scales the x-axis (and thus σ) by N, while the latter scales the variance by N for a square-root improvement:

$$\sigma_{X+Y}^2 = \sigma_X^2 + \sigma_Y^2 + 2\rho\sigma_X\sigma_Y, \quad \rho\text{: Correlation} \tag{6.8}$$

The ability of our proposed module to perform these tasks is governed by the operational fidelities and times of GHZ state initialization and measurement, and by the coherence time of the GHZ state. GHZ states can be prepared in a distributed fashion by following the procedure for projective entanglement generation mentioned in Section 6.2 and distributing such states to the desired subsystem (or location) by the process of direct quantum communication mentioned in Section 6.4. The distances involved should be short enough that coherence times will not become an

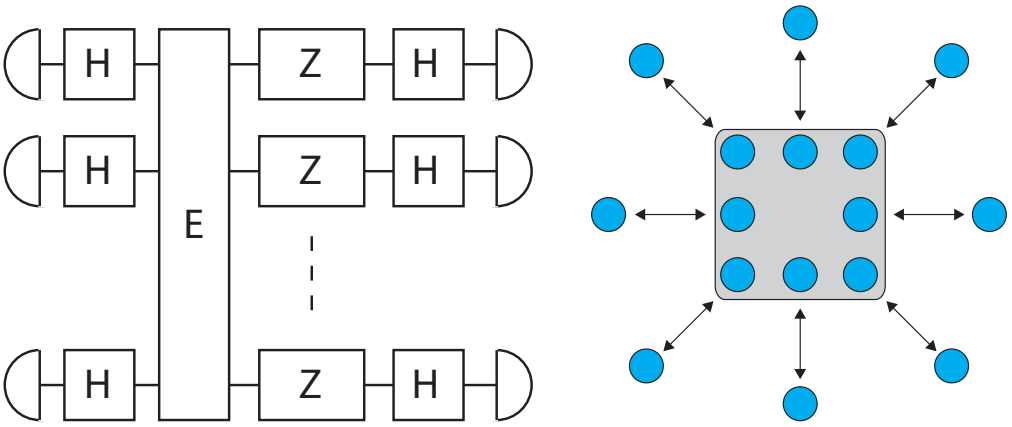

FIGURE 6.4: **(Left)** The circuit corresponding to the sensing operation assumed in Section 6.5. The operations in this circuit are: Left semicircle, state initialization in the Z-basis via measurement (initialisation via cooling or optical pumping could also be used but may require greater time); H, Hadamard operation on the electron spin; E, (projective) entanglement generation between modules; Z, interaction with a magnetic field in the Z-direction; right semicircle, measurement of the electron spin in the Z-basis. The general protocol for performing sensing in quantum metrology consists of a number of repeated applications of such a circuit. The number of repetitions is optimised over a total available measurement time, such that the interaction time is restricted in a single run, which takes a time T. **(Right)** Schematic diagram of the star graph of NV–cavity modules (blue, circles) proposed for the problem of distributed metrology, with redundant qubits at the central node (gray, square) to speed probabilistic state preparation.

issue over the time taken to prepare the initial state. Limited sensing time makes the probabilistic operations the key performance factor. We therefore propose to structure a network of centers according to a *star graph* as shown in Figure 6.4, such that the number of probabilistic operations is minimised. It is known that the entanglement of a GHZ state and of a star graph are equivalent, so that the two states are interchangeable via local operations.

For the purpose of minimising probabilistic operations during potential sensing time, in the central node of the graph we imagine maintaining more qubits than necessary (equal to the number of outer nodes), in an asymmetric approximation to the device multiplexing proposed for quantum communication [109]. During a single round of sensing for the outer nodes, these central qubits are connected in preparation in their own GHZ state. Subsequent initialization then generates the GHZ state with only a single round of probabilistic operations followed by the removal via measurement of the central qubits (or an optimised number, trading the size of the generated state off against the time available for initialization). Outer nodes that are unable to be connected during the initialization time can be partially compensated by leaving central qubits in the GHZ state. We envisage simply avoiding the entanglement-swapping operations that remove these middle nodes from the graph. The failed outer nodes can then be connected, with the redundant central qubits, in advance of the following round. A thorough analysis of the sensing performance would need to take into account the overlapping sensing periods associated with each subsystem, incorporating the effects of the field during initialization. We do

not go into that level of detail here.

If the optimal sensing time per round is T, then the number of nodes is upper bounded by the size of the star graph that can be created in this time, and lower-bounded by the minimum acceptable size of the entangled state. For a high connection probability, the limiting factor may be the fraction of these nodes that are able to form a successful connection in a single round. For a low connection probability, however, the initialization procedure will be dominated by graph state construction during the sensing time, so that we have two alternating subsystems with long times for (what is essentially deterministic) initialization. Assuming attenuation is small over the distances between nodes, the average time for a connection from a single pair is estimated by Equation (6.2) as 3 μs. For a minimum GHZ state of size M and a chain-like structure, we approximate the time required to achieve a GHZ state of this size by $\approx 6\ln(M/2)$ μs, where $\ln(M/2)$ is itself an approximation to the harmonic number $H_{M/2}$, so that $M \leq 2e^{T\times 10^5}$.

6.6 Quantum Computation

Quantum computation is the last, most general, and most difficult goal for quantum information technology. Recently, high fidelity operations and relatively long lifetimes have been achieved in several physical systems, so that how one might go about designing the architecture for such a system has become a serious area of consideration. Any design that depends on having physical qubits close to one another runs into a packing problem not only with the control wires but also with qubits themselves — the mean distance between any two qubits will scale with the diameter of the total region, while the total number of qubits will scale with the volume (or in 2D the area) of the region. For direct interactions, or for schemes requiring the physical movement of the qubits so that they may be brought close to one another, the mean distance between qubits will affect the interaction time as well as the operation fidelity. The complexity of control pulses used to isolate pair-wise interactions will also increase with the size of the system.

A similar architectural problem arises naturally in the structure of quantum error correction codes, both within a logical qubit and between such qubits. Concatenated codes become less local with each layer, the number of qubits to interact with each ancilla scaling as MN^{d-1}, where d is the number of layers of concatenation, N is the multiplicative factor with which the number of qubits increases at each layer, and M is the number of qubits involved in the measurement of a stabiliser operator. Shor's code, for example, consists of $d = 2$ layers of the repetition code, where the number of qubits is multiplied by $N = 3$ at each layer and the number of qubits involved in each stabiliser operation is $M = 2$. In total then, a single ancilla in one layer of Shor's code must interact with a maximum of six physical qubits. Quantum error correction codes with local stabiliser operations, on the other hand, either require multiple *layers* of physical qubits, with each corresponding to a logical qubit, as for the surface code, or require additional time to shift defects around a lattice, as for cluster state quantum computing. Finally, because quantum error correction codes do not allow a universal set of transversal operations, other methods like magic state distillation must be used in general. Connecting all the additional ancillae such that the distilled state can be connected to the appropriate physical qubit in the encoded state is then likely to be highly non-local. Shifting to a distributed scheme offers non-local interactions via photon-mediated probabilistic operations. Key rates for quantum key distribution, which we used in Section 6.4 as indicators of the ability

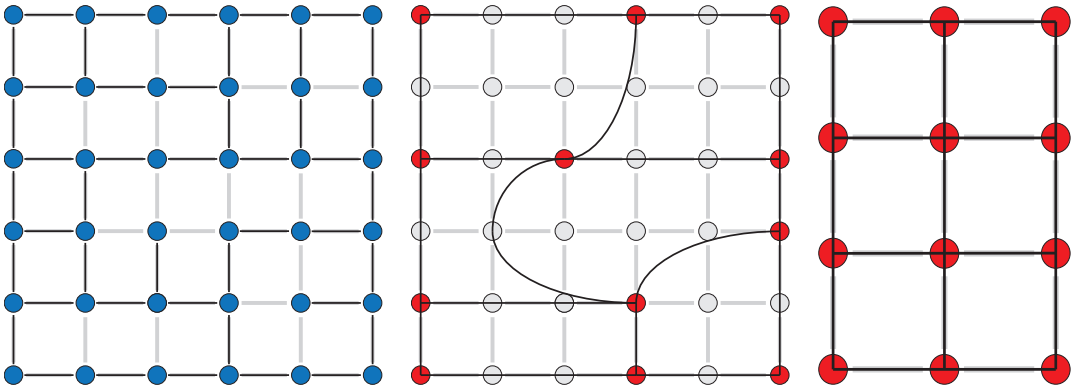

FIGURE 6.5: **(Left)** Entangled links (black) are generated probabilistically between modules (blue) arranged regularly on a 2D square lattice. Not every attempt is successful, and there are defects in the subsequent entanglement graph. **(Middle)** On identifying and measuring the qubits of redundant modules (gray) in the X-basis to remove them from the entangled graph, what remains is a collection of entangled modules (red) in a graph without defects. **(Right)** While the remaining modules may not be arranged regularly in space, the entangled state is homologically identical to a rectangular 2D cluster state. Such states can be extracted from sufficiently large original lattices [345] so long as the probability of each entangled link is greater than the bond percolation threshold of the 2D square lattice, 0.5.

to rapidly create Bell states, are very high for distances as small as the expected mechanical size of a quantum computer, O(meters). In a distributed approach, each qubit is an extension of a repeater module, endowed with the additional requirements that each node contain a logical qubit encoded for quantum error correction, and that it be able to manipulate this qubit with a universal set of quantum gates.

The first step toward independent modules for quantum computation is to construct an encoded logical qubit [282]. Taking the distributed approach also with respect to each node's internal architecture, we can estimate the time to create an entangled state suitable for the surface code of quantum error correction by further altering the analysis in Section 6.5. Instead of the star graph of that section, we now assume a 2D square lattice and estimate the probability that each link in this lattice will be successfully connected. These link probabilities can then be applied to discussions of percolation theory and cluster state generation [345], and we can determine a minimum initialization time such that the threshold for efficiently constructing a 2D cluster state from a larger lattice of modules is satisfied. The concept behind this process is depicted in Figure 6.5. The bond percolation threshold for a 2D square lattice is 0.5, so that the expectation value for the time-to-connection in Equation (6.2), 3 μs, gives the minimum initialization time required. This is well below the coherence time of the nuclear spin in the nitrogen–vacancy center, which is at least of order seconds. This excess allows for entangled states involving on the order of 300 qubits to be included before the collective coherence time is reduced to 10 ms, and error from decoherence due to the initialization time of the state becomes significant on the scale relevant to ongoing quantum error correction ($\approx 0.1\%$).

6.7 Discussion

Through the approximate rates and bounds derived above, we have attempted to show:

1. that the proposed NV–cavity system has the potential to generate entangled links between distant nodes (Sections 6.2 and 6.4),

2. that this entanglement could allow initial demonstrations of the advantages of quantum repeater modules (Section 6.4), which, extended simultaneously to several such devices, could find preliminary application in parameter estimation problems (Section 6.5),

3. and, finally, that once many of these devices are able to be fabricated and connected, the potential exists to generate cluster states applicable to large-scale quantum computation (Section 6.6).

As fabrication and control procedures continue to be refined, we expect that our estimates will prove conservative, and the potential of this system will increase. These points together paint a picture of the NV–cavity module as a candidate for the development of quantum technologies right across the technological development map outlined in the introduction of Section 6.1. We conclude this report with a discussion of this broader developmental picture, and of the challenges that remain ahead, in Chapter 7.

Chapter 7

Conclusions and Future Work

After a brief history of quantum information processing from the perspective of a proponent of distributed, topological cluster state quantum computing, this report has covered five subjects:

1. The use of strong-coupling to engineer a spin-network state with a long coherence time, and its application to quantum sensing.

2. The exploitation of local variance in measurement error rates in the decoding of topological quantum error correction codes, for the reduction of logical error rates or physical qubit numbers.

3. The expected fidelities of cavity-enhanced spin measurement on the negatively charged nitrogen–vacancy center in diamond, incorporating loss, coupling rates, and photon bandwidth.

4. The expected fidelities with the negatively charged silicon–vacancy center in diamond of both

   (a) cavity-enhanced spin measurement, and

   (b) single-qubit rotations via optical STIRAP.

5. Broad rate and performance estimates for the application of the nitrogen–vacancy center photonic module to memory-assisted QKD and entanglement distribution, to distributed quantum sensing, and to cluster state generation.

It will have become apparent to the reader that there is an expected technological progression underlying and tying together the otherwise potentially disparate strands of this report. I have intended for the results outlined in this report to contribute to those levels of computational abstraction relevant to the generation and maintenance of large cluster states. Part I considered the protection of an arbitrary system against local, one-dimensional noise. I focussed here first at the level of fabrication, with strong coupling for passive state protection, and then moved upward to the very lowest layer of what may be considered a *software* or *active* approach to state protection, knowingly (see Sections 2.6 and 3.3) focussing on small-scale effects. At the fundamental physical level, in Part II, I described and analysed low level physical operations in specific physical systems necessary to perform the one- and two-qubit Clifford-group operations of entanglement distribution.

Why do this? Large-scale quantum error correction codes operate successfully and efficiently only once a minimum reliability, expressed through their respective accuracy thresholds, has been attained. For classical computation this is only a concern in a few select areas; usually fundamental operations are reliable enough that

active data protection can be performed explicitly at the software layer in a system-agnostic fashion. Quantum machines, however, have not yet attained this level of reliability; it is not yet possible to separate the *software* and *hardware* elements of this process. Nonetheless, it is not necessary to keep these layers bound to one another in their entirety.

Many systems are limited primarily by error in a single basis — usually dephasing. Highly biased concatenated schemes have been proposed in the past to reduce and equalise error rates prior to the application of higher-level codes for full state protection, with the advantage that resources, either in time or in qubit number, have been saved [24, 226]. It has been my intention with this report to exploit small-scale idiosyncrasies to effect a separation between error protection at the *hardware* and *software* layers, to extend the definition of the quantum *module* to incorporate small-scale error protection measures. In this sense, and with the exception of the universality of the required operations, the definition of the quantum module expands to resemble the quantum repeater.

Two-qubit gates are the most fundamental contributors to error in a typical quantum error correction circuit [234]. As I endeavoured to show in Chapter 6, the implementation of these entanglement-generating gates shares many practical challenges with the fields of quantum sensing and quantum communication. It is in these fields that I see the near-term justification for the necessary but gradual development of larger-scale quantum information processing technologies.

A number of challenges remain ahead. As mentioned in Chapter 4, the fabrication of single photon sources and detectors, as well as the refinement of optical cavities with a diamond interface, remain necessary for high-fidelity projective entanglement generation as proposed. Nor have the two requirements of Chapter 2, strong coupling and T_1-limited coherence through dynamical decoupling, been demonstrated *concurrently* for the superconducting flux qubits taken there as our example. On the theoretical side, while we have shown the benefit of local information for the repetition and surface codes, there is no reason in the near-term nor for enacting the hardware–software separation discussed above why we must use these particular codes; in the small-scale regime and for the distributed approach considered in Chapter 6, the cited advantages of topological codes are not unarguable. For single-basis noise processes any classical code will suffice; the repetition code is only the simplest example. As a final point, we have been speaking in Part II as if the source and detector inefficiencies were strictly problems of experiment and hardware engineering. This assumption is valid under the short-range, small-scale applications envisaged in the near-term, but provides only an incomplete picture when considering the potential long-range interactions of a large-scale, distributed quantum information processing device: when the primary loss channel is long-range transmission, photons (or other carrying media) can be encoded with quantum error correction codes designed to mitigate losses. While there have been a number of developments in this area, it is likely that the optimal code will depend upon the hardware available at each end of the channel for encoding and decoding; this hardware dependence introduces many new details that to the best of our knowledge have not previously been considered in the comparative analysis of these loss codes.

Appendix A

Numerical Methods

Throughout this thesis I have performed several numerical calculations. It is the purpose of this appendix to briefly describe their implementation.

A.1 Dynamical Evolution

The evolution of a physical system under a given Hamiltonian and decay processes was simulated in Chapters 2 and 5. These simulations were performed in the Python programming language, making use of the ordinary differential equation (`ode`) module of the `scipy` library [346]. The Dormand–Prince $8-5-3$ high-order Runge-Kutta method [347] (*'dop853'*) was used, with absolute and relative tolerances of 10^{-14} and 10^{-6} respectively. Linblad terms were incorporated and complex arithmetic handled in the derivative function passed to this solver. The steps per unit time were chosen to allow at least 2 timesteps in the shortest period of oscillation of any of the energy eigenstates.

A.2 Scattered Light

Chapters 4 and 5 used a scattering treatment to determine the reflection statistics of an optical cavity coupled to a negatively charged nitrogen–vacancy center and a negatively charged silicon–vacancy center respectively. This treatment amounts to finding the steady state solution of the system under the evolution of the Hamiltonians described in these respective chapters, with complex frequencies added to account for decay processes as shown in the example Langevin Equation (4.12). To do this, we need only solve a set of linear equations. To this end, the problem was constructed in the Python programming language using the linear algebra (`linalg`) module of the `scipy` library [346]. Ground states and other metastable states of these systems, with lifetimes long by comparison with the optical decay times of the centers and cavities, were then treated between scattering rounds by discrete decay processes according to the chosen time between optical pulses. For mixed states, the density matrix was first diagonalised with the `eigh` function and the scattering treatment applied to each pure state component. The relative frequencies between the modes of the cavity, center, and input field, as well as the relative decay rates of the two cavity mirrors, were optimised locally via gradient descent using the Nelder–Mead algorithm [348] from the `minimize` function from the `optimize` module of the `scipy` library. The initial condition for these relative parameters was equality.

A.3 Decoding Random Error Configurations

Chapter 3 used a Monte Carlo simulation to investigate the logical error rates of the repetition and surface codes for a partcular decoding scheme. This simulation was performed in the C++ programming language.

The SFMT variant of the Mersenne Twister pseudo-random number generator [349] was used to sample both local logical error rates and errors themselves from uniformly distributed pseudo-random numbers provided by the `sfmt_genrand_real2` function. Multiple instances of the simulation were run in parallel, and to seed these instances and control their generation, a control script written in the Python programming language was used. The seeds passed to the pseudo-random number generators of each instance were themselves generated randomly by this control script, using the `random` module of the `scipy` library [346]. This library itself uses the Mersenne Twister pseudo-random number generator and was seeded with a combination of the current time and the process ID of the control script.

The Boost graph library [350] was used for convenience to provide a data structure allowing quick identification of affected stabiliser measurements (treated as graph nodes) for qubit and measurement errors (treated as graph edges). The logarithm of local error rates and the presence of error were incorporated as double-precision floating-point and integer edge properties respectively, while the detection of an odd-parity stabiliser measurement was treated as an integer node property. A further convenience of the Boost graph library was the quick solution of error chain weights via the `johnson_all_pairs_shortest_paths` function.

Following the application of qubit and measurement error in each trial, odd-parity stabiliser measurements (nodes) and the pair-wise distances between them were passed to the minimum-weight perfect matching *Blossom V* library of Kolmogorov [243]. A dummy node was connected to all boundaries of the main graph, at zero distance, to allow matching between stabiliser nodes through the lattice boundaries if this should be the most likely configuration. In cases where an odd number of odd-parity nodes were present (due to measurement error) the additional dummy node was also passed to the matching algorithm.

Bibliography

[1] Feynman, R. P. (1982). Simulating physics with computers. International journal of theoretical physics, 21(6-7), 467-488.

[2] Wiesner, S. (1983). Conjugate coding. ACM Sigact News, 15(1), 78-88.

[3] Deutsch, D. (1985). Quantum theory, the ChurchTuring principle and the universal quantum computer. Proc. R. Soc. Lond. A, 400(1818), 97-117.

[4] Deutsch, D. E. (1989). Quantum computational networks. Proc. R. Soc. Lond. A, 425(1868), 73-90.

[5] Preskill, J. (2018). Quantum Computing in the NISQ era and beyond. arXiv preprint arXiv:1801.00862.

[6] Preskill, J. (2012). Quantum computing and the entanglement frontier. arXiv preprint arXiv:1203.5813.

[7] Dooley, S., Hanks, M., Nakayama, S., Munro, W. J., & Nemoto, K. (2018). Robust quantum sensing with strongly interacting probe systems. npj Quantum Information, 4(1), 24.

[8] Hanks, M., Trupke, M., Schmiedmayer, J., Munro, W. J., & Nemoto, K. (2017). High-fidelity spin measurement on the nitrogen-vacancy center. New Journal of Physics, 19(10), 103002.

[9] Hanks, M., Piparo, N. L., Trupke, M., Schmiedmayer, J., Munro, W. J., & Nemoto, K. (2017, August). A universal quantum module for quantum communication, computation, and metrology. In Quantum Photonic Devices (Vol. 10358, p. 103580K). International Society for Optics and Photonics.

[10] Bennett, C. H., Brassard, G., Breidbart, S., & Wiesner, S. (1984). Eavesdrop-detecting quantum communications channel. IBM Technical Disclosure Bulletin, 26(8), 4363-4366.

[11] Bennett, C. H., & Brassard, G. (1984, August). An update on quantum cryptography. In Workshop on the Theory and Application of Cryptographic Techniques (pp. 475-480). Springer, Berlin, Heidelberg.

[12] Bennett, C. H., & Brassard, G. (2014). Quantum cryptography: Public key distribution and coin tossing. Theor. Comput. Sci., 560(P1), 7-11.

[13] Shor, P. W., & Preskill, J. (2000). Simple proof of security of the BB84 quantum key distribution protocol. Physical review letters, 85(2), 441.

[14] Giovannetti, V., Lloyd, S., & Maccone, L. (2006). Quantum metrology. Physical review letters, 96(1), 010401.

[15] Giovannetti, V., Lloyd, S., & Maccone, L. (2011). Advances in quantum metrology. Nature photonics, 5(4), 222.

[16] Degen, C. L., Reinhard, F., & Cappellaro, P. (2017). Quantum sensing. Reviews of modern physics, 89(3), 035002.

[17] Georgescu, I. M., Ashhab, S., & Nori, F. (2014). Quantum simulation. Reviews of Modern Physics, 86(1), 153.

[18] Shor, P. W. (1994, November). Algorithms for quantum computation: Discrete logarithms and factoring. In Foundations of Computer Science, 1994 Proceedings., 35th Annual Symposium on (pp. 124-134). Ieee.

[19] Grover, L. K. (1996, July). A fast quantum mechanical algorithm for database search. In Proceedings of the twenty-eighth annual ACM symposium on Theory of computing (pp. 212-219). ACM.

[20] Berthiaume, A., Deutsch, D., & Jozsa, R. (1994, November). The stabilisation of quantum computations. In Physics and Computation, 1994. PhysComp'94, Proceedings., Workshop on (pp. 60-62). IEEE.

[21] Barenco, A., Berthiaume, A., Deutsch, D., Ekert, A., Jozsa, R., & Macchiavello, C. (1997). Stabilization of quantum computations by symmetrization. SIAM Journal on Computing, 26(5), 1541-1557.

[22] Bennett, C. H., Brassard, G., Jozsa, R., Mayers, D., Peres, A., Schumacher, B., & Wootters, W. K. (1994). Reduction of quantum entropy by reversible extraction of classical information. Journal of Modern Optics, 41(12), 2307-2314.

[23] Clark, C. R., Metodi, T. S., Gasster, S. D., & Brown, K. R. (2009). Resource requirements for fault-tolerant quantum simulation: The ground state of the transverse Ising model. Physical Review A, 79(6), 062314.

[24] Devitt, S. J., Stephens, A. M., Munro, W. J., & Nemoto, K. (2013). Requirements for fault-tolerant factoring on an atom-optics quantum computer. Nature communications, 4, 2524.

[25] Feynman, R. P. (2012). Theres plenty of room at the bottom: An invitation to enter a new field of physics. In Handbook of Nanoscience, Engineering, and Technology, Third Edition (pp. 26-35). CRC Press.

[26] Moore, G. E. (1998). Cramming more components onto integrated circuits. Proceedings of the IEEE, 86(1), 82-85.

[27] Brillouin, L. (1956). Science and Information Theory. Academic Press Inc., New York.

[28] Landauer, R. (1961). Irreversibility and heat generation in the computing process. IBM Journal of research and development, 5(3), 183-191.

[29] Bennett, C. H. (1973). Logical reversibility of computation. IBM Journal of Research and Development, 17(6), 525-532.

[30] Fredkin, E., & Toffoli, T. (1982). Conservative logic. International Journal of theoretical physics, 21(3-4), 219-253.

[31] Toffoli, T. (1980, July). Reversible computing. In International Colloquium on Automata, Languages, and Programming (pp. 632-644). Springer, Berlin, Heidelberg.

[32] Benioff, P. A. (1980). The computer as a physical system: A microscopic quantum mechanical Hamiltonian model of computers as represented by Turing machines. Journal of statistical physics, 22(5), 563-591.

[33] Benioff, P. A. (1982). Quantum mechanical Hamiltonian models of discrete processes that erase their own histories: Application to Turing machines. International Journal of Theoretical Physics, 21(3-4), 177-201.

[34] Benioff, P. A. (1982). Quantum mechanical Hamiltonian models of Turing machines. Journal of Statistical Physics, 29(3), 515-546.

[35] Benioff, P. A. (1982). Quantum mechanical models of Turing machines that dissipate no energy. Physical Review Letters, 48(23), 1581.

[36] Benioff, P. (1986). Quantum Mechanical Hamiltonian Models of Computers a. Annals of the New York Academy of Sciences, 480(1), 475-486.

[37] Margolus, N. (1984). Physics-like models of computation. Physica D: Nonlinear Phenomena, 10(1-2), 81-95.

[38] Margolus, N. (1986). Quantum Computation a. Annals of the New York Academy of Sciences, 480(1), 487-497.

[39] Margolus, N. H. (1988). Physics and computation (No. MIT/LCS/TR-415). MASSACHUSETTS INST OF TECH CAMBRIDGE LAB FOR COMPUTER SCIENCE.

[40] Milburn, G. J. (1989). Quantum optical Fredkin gate. Physical Review Letters, 62(18), 2124.

[41] Feynman, R. P. (1986). Quantum mechanical computers. Foundations of physics, 16(6), 507-531.

[42] Bell, J. S. (1964). On the einstein podolsky rosen paradox. Physics Physique Fizika, 1(3), 195.

[43] Deutsch, D., & Jozsa, R. (1992). Rapid solution of problems by quantum computation. Proc. R. Soc. Lond. A, 439(1907), 553-558.

[44] Schumacher, B. (1995). Quantum coding. Physical Review A, 51(4), 2738.

[45] Wootters, W. K., & Zurek, W. H. (1982). A single quantum cannot be cloned. Nature, 299(5886), 802-803.

[46] Bernstein, E., & Vazirani, U. (1993, June). Quantum complexity theory. In Proceedings of the twenty-fifth annual ACM symposium on Theory of computing (pp. 11-20). ACM.

[47] Yao, A. C. C. (1993, November). Quantum circuit complexity. In Foundations of Computer Science, 1993. Proceedings., 34th Annual Symposium on (pp. 352-361). IEEE.

[48] Aharonov, D., Kitaev, A., & Nisan, N. (1998, May). Quantum circuits with mixed states. In Proceedings of the thirtieth annual ACM symposium on Theory of computing (pp. 20-30). ACM.

[49] Jozsa, R. (1991). Characterizing classes of functions computable by quantum parallelism. Proc. R. Soc. Lond. A, 435(1895), 563-574.

[50] Cleve, R., Ekert, A., Macchiavello, C., & Mosca, M. (1998, January). Quantum algorithms revisited. In Proceedings of the Royal Society of London A: Mathematical, Physical and Engineering Sciences (Vol. 454, No. 1969, pp. 339-354). The Royal Society.

[51] Berthiaume, A., & Brassard, G. (1992, June). The quantum challenge to structural complexity theory. In Structure in Complexity Theory Conference, 1992., Proceedings of the Seventh Annual (pp. 132-137). IEEE.

[52] Berthiaume, A., & Brassard, G. (1994). Oracle quantum computing. Journal of modern optics, 41(12), 2521-2535.

[53] Simon, D. R. (1994, November). On the power of quantum computation. In Proceedings of the 35th Annual Symposium on Foundations of Computer Science (pp. 116-123). IEEE Computer Society.

[54] NIST (2018, November 5). Quantum Algorithm Zoo. Retrieved from https://math.nist.gov/quantum/zoo/

[55] Finnila, A. B., Gomez, M. A., Sebenik, C., Stenson, C., & Doll, J. D. (1994). Quantum annealing: a new method for minimizing multidimensional functions. Chemical physics letters, 219(5-6), 343-348.

[56] DiVincenzo, D. P. (1995). Two-bit gates are universal for quantum computation. Physical Review A, 51(2), 1015.

[57] Deutsch, D. E., Barenco, A., & Ekert, A. (1995). Universality in quantum computation. Proc. R. Soc. Lond. A, 449(1937), 669-677.

[58] Lloyd, S. (1995). Almost any quantum logic gate is universal. Physical Review Letters, 75(2), 346.

[59] Barenco, A., Bennett, C. H., Cleve, R., DiVincenzo, D. P., Margolus, N., Shor, P., ... & Weinfurter, H. (1995). Elementary gates for quantum computation. Physical review A, 52(5), 3457.

[60] Barenco, A., Deutsch, D., Ekert, A., & Jozsa, R. (1995). Conditional quantum dynamics and logic gates. Physical Review Letters, 74(20), 4083.

[61] Sleator, T., & Weinfurter, H. (1995). Realizable universal quantum logic gates. Physical Review Letters, 74(20), 4087.

[62] DiVincenzo, D. P., & Smolin, J. Results on two-bit gate design for quantum computers. In Proceedings Workshop on Physics and Computation. PhysComp (pp. 14-23). IEEE.

[63] Chau, H. F., & Wilczek, F. (1995). Simple realization of the Fredkin gate using a series of two-body operators. Physical review letters, 75(4), 748.

[64] Smolin, J. A., & DiVincenzo, D. P. (1996). Five two-bit quantum gates are sufficient to implement the quantum Fredkin gate. Physical Review A, 53(4), 2855.

[65] Bennett, C. H., Brassard, G., Crépeau, C., Jozsa, R., Peres, A., & Wootters, W. K. (1993). Teleporting an unknown quantum state via dual classical and Einstein-Podolsky-Rosen channels. Physical review letters, 70(13), 1895.

[66] Gottesman, D., & Chuang, I. L. (1999). Quantum teleportation is a universal computational primitive. arXiv preprint quant-ph/9908010.

[67] Gottesman, D., & Chuang, I. L. (1999). Demonstrating the viability of universal quantum computation using teleportation and single-qubit operations. Nature, 402(6760), 390.

[68] Bravyi, S., & Kitaev, A. (2005). Universal quantum computation with ideal Clifford gates and noisy ancillas. Physical Review A, 71(2), 022316.

[69] Briegel, H. J., Browne, D. E., D ur, W., Raussendorf, R., & Van den Nest, M. (2009). Measurement-based quantum computation. Nature Physics, 5(1), 19.

[70] Landauer, R. (1995). Is quantum mechanics useful?. Phil. Trans. R. Soc. Lond. A, 353(1703), 367-376.

[71] Chuang, I. L., Laflamme, R., Shor, P. W., & Zurek, W. H. (1995). Quantum computers, factoring, and decoherence. Science, 270(5242), 1633-1635.

[72] Unruh, W. G. (1995). Maintaining coherence in quantum computers. Physical Review A, 51(2), 992.

[73] Palma, G. M., Suominen, K. A., & Ekert, A. (1996). Quantum computers and dissipation. Proc. R. Soc. Lond. A, 452(1946), 567-584.

[74] Hamming, R. W. (1950). Error detecting and error correcting codes. Bell System technical journal, 29(2), 147-160.

[75] Von Neumann, J. (1956). Probabilistic logics and the synthesis of reliable organisms from unreliable components. Automata studies, 34, 43-98.

[76] Bennett, C. H., Brassard, G., Popescu, S., Schumacher, B., Smolin, J. A., & Wootters, W. K. (1996). Purification of noisy entanglement and faithful teleportation via noisy channels. Physical review letters, 76(5), 722.

[77] Deutsch, D., Ekert, A., Jozsa, R., Macchiavello, C., Popescu, S., & Sanpera, A. (1996). Quantum privacy amplification and the security of quantum cryptography over noisy channels. Physical review letters, 77(13), 2818.

[78] Misra, B., & Sudarshan, E. G. (1977). The Zenos paradox in quantum theory. Journal of Mathematical Physics, 18(4), 756-763.

[79] Shor, P. W. (1995). Scheme for reducing decoherence in quantum computer memory. Physical review A, 52(4), R2493.

[80] Kimura, G. (2003). The Bloch vector for N-level systems. Physics Letters A, 314(5-6), 339-349.

[81] Calderbank, A. R., & Shor, P. W. (1996). Good quantum error-correcting codes exist. Physical Review A, 54(2), 1098.

[82] Shor, P. W., & Smolin, J. A. (1996). Quantum error-correcting codes need not completely reveal the error syndrome. arXiv preprint quant-ph/9604006.

[83] Steane, A. M. (1996). Error correcting codes in quantum theory. Physical Review Letters, 77(5), 793.

[84] Steane, A. (1996). Multiple-particle interference and quantum error correction. Proc. R. Soc. Lond. A, 452(1954), 2551-2577.

[85] Steane, A. M. (1996). Simple quantum error-correcting codes. Physical Review A, 54(6), 4741.

[86] Ekert, A., & Macchiavello, C. (1996). Error correction in quantum communication. arXiv preprint quant-ph/9602022.

[87] Bennett, C. H., DiVincenzo, D. P., Smolin, J. A., & Wootters, W. K. (1996). Mixed-state entanglement and quantum error correction. Physical Review A, 54(5), 3824.

[88] Gottesman, D. (1996). Class of quantum error-correcting codes saturating the quantum Hamming bound. Physical Review A, 54(3), 1862.

[89] Rains, E. M., Hardin, R. H., Shor, P. W., & Sloane, N. J. A. (1997). A nonadditive quantum code. Physical Review Letters, 79(5), 953.

[90] Knill, E., & Laflamme, R. (1997). Theory of quantum error-correcting codes. Physical Review A, 55(2), 900.

[91] Calderbank, A. R., Rains, E. M., Shor, P. W., & Sloane, N. J. (1997). Quantum error correction and orthogonal geometry. Physical Review Letters, 78(3), 405.

[92] Calderbank, A. R., Rains, E. M., Shor, P. M., & Sloane, N. J. (1998). Quantum error correction via codes over GF (4). IEEE Transactions on Information Theory, 44(4), 1369-1387.

[93] Laflamme, R., Miquel, C., Paz, J. P., & Zurek, W. H. (1996). Perfect quantum error correcting code. Physical Review Letters, 77(1), 198.

[94] Shor, P. W. (1996, October). Fault-tolerant quantum computation. In Foundations of Computer Science, 1996. Proceedings., 37th Annual Symposium on (pp. 56-65). IEEE.

[95] Knill, E., & Laflamme, R. (1996). Concatenated quantum codes. arXiv preprint quant-ph/9608012.

[96] Knill, E., Laflamme, R., & Zurek, W. (1996). Threshold accuracy for quantum computation. arXiv preprint quant-ph/9610011.

[97] Knill, E., Laflamme, R., & Zurek, W. H. (1998). Resilient quantum computation. Science, 279(5349), 342-345.

[98] Knill, E., Laflamme, R., & Zurek, W. H. (1998, January). Resilient quantum computation: error models and thresholds. In Proceedings of the Royal Society of London A: Mathematical, Physical and Engineering Sciences (Vol. 454, No. 1969, pp. 365-384). The Royal Society.

[99] DiVincenzo, D. P., & Shor, P. W. (1996). Fault-tolerant error correction with efficient quantum codes. Physical review letters, 77(15), 3260.

[100] Kitaev, A. Y. (1997). Quantum computations: algorithms and error correction. Russian Mathematical Surveys, 52(6), 1191-1249.

[101] Kitaev, A. Y. (1997). Quantum error correction with imperfect gates. In Quantum Communication, Computing, and Measurement (pp. 181-188). Springer, Boston, MA.

[102] Kitaev, A. Y. (2003). Fault-tolerant quantum computation by anyons. Annals of Physics, 303(1), 2-30.

[103] Bravyi, S. B., & Kitaev, A. Y. (1998). Quantum codes on a lattice with boundary. arXiv preprint quant-ph/9811052.

[104] Freedman, M. H., & Meyer, D. A. (2001). Projective plane and planar quantum codes. Foundations of Computational Mathematics, 1(3), 325-332.

[105] Dennis, E., Kitaev, A., Landahl, A., & Preskill, J. (2002). Topological quantum memory. Journal of Mathematical Physics, 43(9), 4452-4505.

[106] Stephens, A. M. (2014). Fault-tolerant thresholds for quantum error correction with the surface code. Physical Review A, 89(2), 022321.

[107] Ralph, T. C., Hayes, A. J. F., & Gilchrist, A. (2005). Loss-tolerant optical qubits. Physical review letters, 95(10), 100501.

[108] Simon, C., De Riedmatten, H., Afzelius, M., Sangouard, N., Zbinden, H., & Gisin, N. (2007). Quantum repeaters with photon pair sources and multimode memories. Physical review letters, 98(19), 190503.

[109] Munro, W. J., Harrison, K. A., Stephens, A. M., Devitt, S. J., & Nemoto, K. (2010). From quantum multiplexing to high-performance quantum networking. Nature Photonics, 4(11), 792.

[110] Munro, W. J., Stephens, A. M., Devitt, S. J., Harrison, K. A., & Nemoto, K. (2012). Quantum communication without the necessity of quantum memories. Nature Photonics, 6(11), 777.

[111] Raussendorf, R., & Briegel, H. J. (2001). A one-way quantum computer. Physical Review Letters, 86(22), 5188.

[112] Raussendorf, R., Browne, D. E., & Briegel, H. J. (2003). Measurement-based quantum computation on cluster states. Physical review A, 68(2), 022312.

[113] Kribs, D., Laflamme, R., & Poulin, D. (2005). Unified and generalized approach to quantum error correction. Physical review letters, 94(18), 180501.

[114] Kribs, D. W., Laflamme, R., Poulin, D., & Lesosky, M. (2005). Operator quantum error correction. arXiv preprint quant-ph/0504189.

[115] Bombin, H., & Martin-Delgado, M. A. (2006). Topological quantum distillation. Physical review letters, 97(18), 180501.

[116] Bombin, H. (2015). Gauge color codes: optimal transversal gates and gauge fixing in topological stabilizer codes. New Journal of Physics, 17(8), 083002.

[117] Raussendorf, R., Harrington, J., & Goyal, K. (2006). A fault-tolerant one-way quantum computer. Annals of physics, 321(9), 2242-2270.

[118] Fowler, A. G. (2011). Two-dimensional color-code quantum computation. Physical Review A, 83(4), 042310.

[119] Horsman, C., Fowler, A. G., Devitt, S., & Van Meter, R. (2012). Surface code quantum computing by lattice surgery. New Journal of Physics, 14(12), 123011.

[120] Cirac, J. I., & Zoller, P. (1995). Quantum computations with cold trapped ions. Physical review letters, 74(20), 4091.

[121] Wineland, D. J., Monroe, C., Itano, W. M., Leibfried, D., King, B. E., & Meekhof, D. M. (1998). Experimental issues in coherent quantum-state manipulation of trapped atomic ions. Journal of Research of the National Institute of Standards and Technology, 103(3), 259.

[122] Cirac, J. I., & Zoller, P. (2000). A scalable quantum computer with ions in an array of microtraps. Nature, 404(6778), 579.

[123] Kielpinski, D., Monroe, C., & Wineland, D. J. (2002). Architecture for a large-scale ion-trap quantum computer. Nature, 417(6890), 709.

[124] Leibfried, D., Blatt, R., Monroe, C., & Wineland, D. (2003). Quantum dynamics of single trapped ions. Reviews of Modern Physics, 75(1), 281.

[125] Porras, D., & Cirac, J. I. (2004). Effective quantum spin systems with trapped ions. Physical review letters, 92(20), 207901.

[126] Häffner, H., Hänsel, W., Roos, C. F., Benhelm, J., Chwalla, M., Körber, T., ... & Gühne, O. (2005). Scalable multiparticle entanglement of trapped ions. Nature, 438(7068), 643.

[127] Blatt, R., & Wineland, D. (2008). Entangled states of trapped atomic ions. Nature, 453(7198), 1008.

[128] Häffner, H., Roos, C. F., & Blatt, R. (2008). Quantum computing with trapped ions. Physics reports, 469(4), 155-203.

[129] Kim, K., Chang, M. S., Korenblit, S., Islam, R., Edwards, E. E., Freericks, J. K., ... & Monroe, C. (2010). Quantum simulation of frustrated Ising spins with trapped ions. Nature, 465(7298), 590.

[130] Blatt, R., & Roos, C. F. (2012). Quantum simulations with trapped ions. Nature Physics, 8(4), 277.

[131] Blais, A., Huang, R. S., Wallraff, A., Girvin, S. M., & Schoelkopf, R. J. (2004). Cavity quantum electrodynamics for superconducting electrical circuits: An architecture for quantum computation. Physical Review A, 69(6), 062320.

[132] Wallraff, A., Schuster, D. I., Blais, A., Frunzio, L., Huang, R. S., Majer, J., ... & Schoelkopf, R. J. (2004). Strong coupling of a single photon to a superconducting qubit using circuit quantum electrodynamics. Nature, 431(7005), 162.

[133] You, J. Q., & Nori, F. (2005). Superconducting Circuits and Quantum Information. Physics Today, 58(11), 42-47.

[134] Hofheinz, M., Weig, E. M., Ansmann, M., Bialczak, R. C., Lucero, E., Neeley, M., ... & Cleland, A. N. (2008). Generation of Fock states in a superconducting quantum circuit. Nature, 454(7202), 310.

[135] You, J. Q., & Nori, F. (2011). Atomic physics and quantum optics using superconducting circuits. Nature, 474(7353), 589.

[136] Houck, A. A., Türeci, H. E., & Koch, J. (2012). On-chip quantum simulation with superconducting circuits. Nature Physics, 8(4), 292.

[137] Devoret, M. H., & Schoelkopf, R. J. (2013). Superconducting circuits for quantum information: an outlook. Science, 339(6124), 1169-1174.

[138] Xiang, Z. L., Ashhab, S., You, J. Q., & Nori, F. (2013). Hybrid quantum circuits: Superconducting circuits interacting with other quantum systems. Reviews of Modern Physics, 85(2), 623.

[139] Barends, R., Kelly, J., Megrant, A., Veitia, A., Sank, D., Jeffrey, E., ... & Chen, Y. (2014). Superconducting quantum circuits at the surface code threshold for fault tolerance. Nature, 508(7497), 500.

[140] Kelly, J., Barends, R., Fowler, A. G., Megrant, A., Jeffrey, E., White, T. C., ... & Chen, Z. (2015). State preservation by repetitive error detection in a superconducting quantum circuit. Nature, 519(7541), 66.

[141] Loss, D., & DiVincenzo, D. P. (1998). Quantum computation with quantum dots. Physical Review A, 57(1), 120.

[142] Burkard, G., Loss, D., & DiVincenzo, D. P. (1999). Coupled quantum dots as quantum gates. Physical Review B, 59(3), 2070.

[143] Imamoğlu, A., Awschalom, D. D., Burkard, G., DiVincenzo, D. P., Loss, D., Sherwin, M., & Small, A. (1999). Quantum information processing using quantum dot spins and cavity QED. Physical review letters, 83(20), 4204.

[144] Benson, O., Santori, C., Pelton, M., & Yamamoto, Y. (2000). Regulated and entangled photons from a single quantum dot. Physical review letters, 84(11), 2513.

[145] Michler, P., Kiraz, A., Becher, C., Schoenfeld, W. V., Petroff, P. M., Zhang, L., ... & Imamoğlu, A. (2000). A quantum dot single-photon turnstile device. science, 290(5500), 2282-2285.

[146] Petta, J. R., Johnson, A. C., Taylor, J. M., Laird, E. A., Yacoby, A., Lukin, M. D., ... & Gossard, A. C. (2005). Coherent manipulation of coupled electron spins in semiconductor quantum dots. Science, 309(5744), 2180-2184.

[147] Hennessy, K., Badolato, A., Winger, M., Gerace, D., Atatüre, M., Gulde, S., ... & Imamoğlu, A. (2007). Quantum nature of a strongly coupled single quantum dotcavity system. Nature, 445(7130), 896.

[148] Hanson, R., Kouwenhoven, L. P., Petta, J. R., Tarucha, S., & Vandersypen, L. M. (2007). Spins in few-electron quantum dots. Reviews of Modern Physics, 79(4), 1217.

[149] Kairdolf, B. A., Smith, A. M., Stokes, T. H., Wang, M. D., Young, A. N., & Nie, S. (2013). Semiconductor quantum dots for bioimaging and biodiagnostic applications. Annual review of analytical chemistry, 6, 143-162.

[150] Knill, E., Laflamme, R., & Milburn, G. J. (2001). A scheme for efficient quantum computation with linear optics. nature, 409(6816), 46.

[151] Kok, P., Munro, W. J., Nemoto, K., Ralph, T. C., Dowling, J. P., & Milburn, G. J. (2007). Linear optical quantum computing with photonic qubits. Reviews of Modern Physics, 79(1), 135.

[152] O'Brien, J. L. (2007). Optical quantum computing. Science, 318(5856), 1567-1570.

[153] Kane, B. E. (1998). A silicon-based nuclear spin quantum computer. nature, 393(6681), 133.

[154] Vrijen, R., Yablonovitch, E., Wang, K., Jiang, H. W., Balandin, A., Roychowdhury, V., ... & DiVincenzo, D. (2000). Electron-spin-resonance transistors for quantum computing in silicon-germanium heterostructures. Physical Review A, 62(1), 012306.

[155] Morton, J. J., Tyryshkin, A. M., Brown, R. M., Shankar, S., Lovett, B. W., Ardavan, A., ... & Lyon, S. A. (2008). Solid-state quantum memory using the 31 P nuclear spin. Nature, 455(7216), 1085.

[156] Pla, J. J., Tan, K. Y., Dehollain, J. P., Lim, W. H., Morton, J. J., Jamieson, D. N., ... & Morello, A. (2012). A single-atom electron spin qubit in silicon. Nature, 489(7417), 541.

[157] Tyryshkin, A. M., Tojo, S., Morton, J. J., Riemann, H., Abrosimov, N. V., Becker, P., ... & Lyon, S. A. (2012). Electron spin coherence exceeding seconds in high-purity silicon. Nature materials, 11(2), 143.

[158] Steger, M., Saeedi, K., Thewalt, M. L. W., Morton, J. J. L., Riemann, H., Abrosimov, N. V., ... & Pohl, H. J. (2012). Quantum information storage for over 180 s using donor spins in a 28Si semiconductor vacuum. Science, 336(6086), 1280-1283.

[159] Pla, J. J., Tan, K. Y., Dehollain, J. P., Lim, W. H., Morton, J. J., Zwanenburg, F. A., ... & Morello, A. (2013). High-fidelity readout and control of a nuclear spin qubit in silicon. Nature, 496(7445), 334.

[160] Zwanenburg, F. A., Dzurak, A. S., Morello, A., Simmons, M. Y., Hollenberg, L. C., Klimeck, G., ... & Eriksson, M. A. (2013). Silicon quantum electronics. Reviews of modern physics, 85(3), 961.

[161] Gordon, L., Weber, J. R., Varley, J. B., Janotti, A., Awschalom, D. D., & Van de Walle, C. G. (2013). Quantum computing with defects. Mrs Bulletin, 38(10), 802-807.

[162] Dzurak, A. (2011). Quantum computing: Diamond and silicon converge. Nature, 479(7371), 47.

[163] Aharonovich, I., Greentree, A. D., & Prawer, S. (2011). Diamond photonics. Nature Photonics, 5(7), 397.

[164] Koehl, W. F., Buckley, B. B., Heremans, F. J., Calusine, G., & Awschalom, D. D. (2011). Room temperature coherent control of defect spin qubits in silicon carbide. Nature, 479(7371), 84.

[165] Aharonovich, I., Castelletto, S., Simpson, D. A., Su, C. H., Greentree, A. D., & Prawer, S. (2011). Diamond-based single-photon emitters. Reports on progress in Physics, 74(7), 076501.

[166] Weber, J. R., Koehl, W. F., Varley, J. B., Janotti, A., Buckley, B. B., Van de Walle, C. G., & Awschalom, D. D. (2010). Quantum computing with defects. Proceedings of the National Academy of Sciences, 107(19), 8513-8518.

[167] Greentree, A. D., Fairchild, B. A., Hossain, F. M., & Prawer, S. (2008). Diamond integrated quantum photonics. Materials Today, 11(9), 22-31.

[168] Wrachtrup, J., & Jelezko, F. (2006). Processing quantum information in diamond. Journal of Physics: Condensed Matter, 18(21), S807.

[169] Jelezko, F., & Wrachtrup, J. (2006). Single defect centres in diamond: A review. physica status solidi (a), 203(13), 3207-3225.

[170] Davies, G., Lawson, S. C., Collins, A. T., Mainwood, A., & Sharp, S. J. (1992). Vacancy-related centers in diamond. Physical Review B, 46(20), 13157.

[171] Zaitsev, A. M. (2000). Vibronic spectra of impurity-related optical centers in diamond. Physical Review B, 61(19), 12909.

[172] Brouri, R., Beveratos, A., Poizat, J. P., & Grangier, P. (2000). Photon antibunching in the fluorescence of individual color centers in diamond. Optics letters, 25(17), 1294-1296.

[173] Gaebel, T., Domhan, M., Popa, I., Wittmann, C., Neumann, P., Jelezko, F., ... & Meijer, J. (2006). Room-temperature coherent coupling of single spins in diamond. Nature Physics, 2(6), 408.

[174] Togan, E., Chu, Y., Trifonov, A. S., Jiang, L., Maze, J., Childress, L., ... & Lukin, M. D. (2010). Quantum entanglement between an optical photon and a solid-state spin qubit. Nature, 466(7307), 730.

[175] Robledo, L., Childress, L., Bernien, H., Hensen, B., Alkemade, P. F., & Hanson, R. (2011). High-fidelity projective read-out of a solid-state spin quantum register. Nature, 477(7366), 574.

[176] Maurer, P. C., Kucsko, G., Latta, C., Jiang, L., Yao, N. Y., Bennett, S. D., ... & Twitchen, D. J. (2012). Room-temperature quantum bit memory exceeding one second. Science, 336(6086), 1283-1286.

[177] Zhou, J. W., Wang, P. F., Shi, F. Z., Huang, P., Kong, X., Xu, X. K., ... & Du, J. F. (2014). Quantum information processing and metrology with color centers in diamonds. Frontiers of Physics, 9(5), 587-597.

[178] Rong, X., Geng, J., Shi, F., Liu, Y., Xu, K., Ma, W., ... & Du, J. (2015). Experimental fault-tolerant universal quantum gates with solid-state spins under ambient conditions. Nature communications, 6, 8748.

[179] Kurtsiefer, C., Mayer, S., Zarda, P., & Weinfurter, H. (2000). Stable solid-state source of single photons. Physical review letters, 85(2), 290.

[180] Dutt, M. G., Childress, L., Jiang, L., Togan, E., Maze, J., Jelezko, F., ... & Lukin, M. D. (2007). Quantum register based on individual electronic and nuclear spin qubits in diamond. Science, 316(5829), 1312-1316.

[181] Babinec, T. M., Hausmann, B. J., Khan, M., Zhang, Y., Maze, J. R., Hemmer, P. R., & Lončar, M. (2010). A diamond nanowire single-photon source. Nature nanotechnology, 5(3), 195.

[182] Budker, D., & Romalis, M. (2007). Optical magnetometry. Nature Physics, 3(4), 227.

[183] Rondin, L., Tetienne, J. P., Hingant, T., Roch, J. F., Maletinsky, P., & Jacques, V. (2014). Magnetometry with nitrogen-vacancy defects in diamond. Reports on progress in physics, 77(5), 056503.

[184] Tanaka, T., Knott, P., Matsuzaki, Y., Dooley, S., Yamaguchi, H., Munro, W. J., & Saito, S. (2015). Proposed robust entanglement-based magnetic field sensor beyond the standard quantum limit. Physical review letters, 115(17), 170801.

[185] Ludlow, A. D., Boyd, M. M., Ye, J., Peik, E., & Schmidt, P. O. (2015). Optical atomic clocks. Reviews of Modern Physics, 87(2), 637.

[186] Greenberger, D. M., Horne, M. A., & Zeilinger, A. (1989). Going beyond Bells theorem. In Bells theorem, quantum theory and conceptions of the universe (pp. 69-72). Springer, Dordrecht.

[187] Paz, J. P., & Zurek, W. H. (1998, January). Continuous error correction. In Proceedings of the Royal Society of London A: Mathematical, Physical and Engineering Sciences (Vol. 454, No. 1969, pp. 355-364). The Royal Society.

[188] Ahn, C., Doherty, A. C., & Landahl, A. J. (2002). Continuous quantum error correction via quantum feedback control. Physical Review A, 65(4), 042301.

[189] Sarovar, M., & Milburn, G. J. (2005). Continuous quantum error correction by cooling. Physical Review A, 72(1), 012306.

[190] Ippoliti, M., Mazza, L., Rizzi, M., & Giovannetti, V. (2015). Perturbative approach to continuous-time quantum error correction. Physical Review A, 91(4), 042322.

[191] Pastawski, F., Clemente, L., & Cirac, J. I. (2011). Quantum memories based on engineered dissipation. Physical Review A, 83(1), 012304.

[192] Brown, B. J., Loss, D., Pachos, J. K., Self, C. N., & Wootton, J. R. (2016). Quantum memories at finite temperature. Reviews of Modern Physics, 88(4), 045005.

[193] Reiter, F., Sørensen, A. S., Zoller, P., & Muschik, C. A. (2017). Dissipative quantum error correction and application to quantum sensing with trapped ions. Nature communications, 8(1), 1822.

[194] Leghtas, Z., Kirchmair, G., Vlastakis, B., Schoelkopf, R. J., Devoret, M. H., & Mirrahimi, M. (2013). Hardware-efficient autonomous quantum memory protection. Physical Review Letters, 111(12), 120501.

[195] Cohen, J., & Mirrahimi, M. (2014). Dissipation-induced continuous quantum error correction for superconducting circuits. Physical Review A, 90(6), 062344.

[196] Barnes, J. P., & Warren, W. S. (2000). Automatic quantum error correction. Physical review letters, 85(4), 856.

[197] Kapit, E. (2016). Hardware-efficient and fully autonomous quantum error correction in superconducting circuits. Physical review letters, 116(15), 150501.

[198] Bengtsson, I., & Życzkowski, K. (2017). Geometry of quantum states: an introduction to quantum entanglement. Cambridge university press.

[199] Kullback, S., & Leibler, R. A. (1951). On information and sufficiency. Ann. Math. Stat., 22:79.

[200] Jeffreys, H. (1961). Theory of Probability. Oxford: Clarendom Press.

[201] Shannon, C. E. (1948). A mathematical theory of communication. Bell Sys. Tech J., 27:379, 623.

[202] Sanov, I. N. (1957). On the probability of large deviations of random variables (in Russian). Mat. Sbornik, 42:11.

[203] Cramér, H. (1946). Mathematical methods of statistics.

[204] Rao, C. R. (1945). Information and the accuracy attainable in the estimation of statistical parameters.

[205] Petz, D., & Ghinea, C. (2011). Introduction to quantum Fisher information. In Quantum probability and related topics (pp. 261-281).

[206] Schlosshauer, M. A. (2007). Decoherence: and the quantum-to-classical transition. Springer Science & Business Media.

[207] Dooley, S., Hanks, M., Nakayama, S., Munro, W. J., & Nemoto, K. (2018). SUPPLEMENTARY MATERIAL: Robust quantum sensing with strongly interacting probe systems. npj Quantum Information, 4(1), 24.

[208] Yoshihara, F., Harrabi, K., Niskanen, A. O., Nakamura, Y., & Tsai, J. S. (2006). Decoherence of flux qubits due to 1/f flux noise. Physical review letters, 97(16), 167001.

[209] Bylander, J., Gustavsson, S., Yan, F., Yoshihara, F., Harrabi, K., Fitch, G., ... & Oliver, W. D. (2011). Noise spectroscopy through dynamical decoupling with a superconducting flux qubit. Nature Physics, 7(7), 565.

[210] Yan, F., Gustavsson, S., Kamal, A., Birenbaum, J., Sears, A. P., Hover, D., ... & Yoder, J. L. (2016). The flux qubit revisited to enhance coherence and reproducibility. Nature communications, 7, 12964.

[211] Grajcar, M., Izmalkov, A., Van der Ploeg, S. H. W., Linzen, S., Plecenik, T., Wagner, T., ... & Love, P. J. (2006). Four-qubit device with mixed couplings. Physical review letters, 96(4), 047006.

[212] Harris, R., Lanting, T., Berkley, A. J., Johansson, J., Johnson, M. W., Bunyk, P., ... & Han, S. (2009). Compound Josephson-junction coupler for flux qubits with minimal crosstalk. Physical Review B, 80(5), 052506.

[213] Lanting, T., Przybysz, A. J., Smirnov, A. Y., Spedalieri, F. M., Amin, M. H., Berkley, A. J., ... & Dickson, N. (2014). Entanglement in a quantum annealing processor. Physical Review X, 4(2), 021041.

[214] Arrad, G., Vinkler, Y., Aharonov, D., & Retzker, A. (2014). Increasing sensing resolution with error correction. Physical review letters, 112(15), 150801.

[215] Kessler, E. M., Lovchinsky, I., Sushkov, A. O., & Lukin, M. D. (2014). Quantum error correction for metrology. Physical review letters, 112(15), 150802.

[216] Dür, W., Skotiniotis, M., Froewis, F., & Kraus, B. (2014). Improved quantum metrology using quantum error correction. Physical Review Letters, 112(8), 080801.

[217] Unden, T., Balasubramanian, P., Louzon, D., Vinkler, Y., Plenio, M. B., Markham, M., ... & Lukin, M. D. (2016). Quantum metrology enhanced by repetitive quantum error correction. Physical review letters, 116(23), 230502.

[218] Viola, L., Knill, E., & Lloyd, S. (1999). Dynamical decoupling of open quantum systems. Physical Review Letters, 82(12), 2417.

[219] Matsuzaki, Y., & Benjamin, S. (2017). Magnetic-field sensing with quantum error detection under the effect of energy relaxation. Physical Review A, 95(3), 032303.

[220] Lidar, D. A., & Brun, T. A. (Eds.). (2013). Quantum error correction. Cambridge University Press.

[221] Devitt, S. J., Munro, W. J., & Nemoto, K. (2013). Quantum error correction for beginners. Reports on Progress in Physics, 76(7), 076001.

[222] Terhal, B. M. (2015). Quantum error correction for quantum memories. Reviews of Modern Physics, 87(2), 307.

[223] Vaidman, L., Goldenberg, L., & Wiesner, S. (1996). Error prevention scheme with four particles. Physical Review A, 54(3), R1745.

[224] Aliferis, P., & Preskill, J. (2008). Fault-tolerant quantum computation against biased noise. Physical Review A, 78(5), 052331.

[225] Brooks, P. B. (2013). Quantum error correction with biased noise (Doctoral dissertation, California Institute of Technology).

[226] Stephens, A. M., Munro, W. J., & Nemoto, K. (2013). High-threshold topological quantum error correction against biased noise. Physical Review A, 88(6), 060301.

[227] Stace, T. M., Barrett, S. D., & Doherty, A. C. (2009). Thresholds for topological codes in the presence of loss. Physical review letters, 102(20), 200501.

[228] Stace, T. M., & Barrett, S. D. (2010). Error correction and degeneracy in surface codes suffering loss. Physical Review A, 81(2), 022317.

[229] Barrett, S. D., & Stace, T. M. (2010). Fault tolerant quantum computation with very high threshold for loss errors. Physical review letters, 105(20), 200502.

[230] Ohzeki, M. (2012). Error threshold estimates for surface code with loss of qubits. Physical Review A, 85(6), 060301.

[231] Fujii, K., & Tokunaga, Y. (2012). Error and loss tolerances of surface codes with general lattice structures. Physical Review A, 86(2), 020303.

[232] Tomita, Y., & Svore, K. M. (2014). Low-distance surface codes under realistic quantum noise. Physical Review A, 90(6), 062320.

[233] Darmawan, A. S., & Poulin, D. (2017). Tensor-network simulations of the surface code under realistic noise. Physical review letters, 119(4), 040502.

[234] Wang, D. S., Fowler, A. G., & Hollenberg, L. C. (2011). Surface code quantum computing with error rates over 1%. Physical Review A, 83(2), 020302.

[235] Bombin, H., Andrist, R. S., Ohzeki, M., Katzgraber, H. G., & Martin-Delgado, M. A. (2012). Strong resilience of topological codes to depolarization. Physical Review X, 2(2), 021004.

[236] Jouzdani, P., Novais, E., & Mucciolo, E. R. (2013). Fidelity of the surface code in the presence of a bosonic bath. Physical Review A, 88(1), 012336.

[237] Novais, E., & Mucciolo, E. R. (2013). Surface code threshold in the presence of correlated errors. Physical review letters, 110(1), 010502.

[238] Jouzdani, P., Novais, E., Tupitsyn, I. S., & Mucciolo, E. R. (2014). Fidelity threshold of the surface code beyond single-qubit error models. Physical Review A, 90(4), 042315.

[239] Jouzdani, P., & Mucciolo, E. R. (2014). Numerical evaluation of the fidelity error threshold for the surface code. Physical Review A, 90(1), 012315.

[240] Fowler, A. G. (2013). Coping with qubit leakage in topological codes. Physical Review A, 88(4), 042308.

[241] Suchara, M., Cross, A. W., & Gambetta, J. M. (2015, June). Leakage suppression in the toric code. In Information Theory (ISIT), 2015 IEEE International Symposium on (pp. 1119-1123). IEEE.

[242] Wilson, E. B. (1927). Probable inference, the law of succession, and statistical inference. Journal of the American Statistical Association, 22(158), 209-212.

[243] Kolmogorov, V. (2009). Blossom V: a new implementation of a minimum cost perfect matching algorithm. Mathematical Programming Computation, 1(1), 43-67.

[244] Edmonds, J. (1965). Paths, trees, and flowers. Canadian Journal of mathematics, 17(3), 449-467.

[245] Gottesman, D. (1997). Caltech PhD Thesis. Preprint at http://arxiv.org/abs/quant-ph/9705052.

[246] Duclos-Cianci, G., & Poulin, D. (2010, August). A renormalization group decoding algorithm for topological quantum codes. In Information Theory Workshop (ITW), 2010 IEEE (pp. 1-5). IEEE.

[247] Duclos-Cianci, G., & Poulin, D. (2010). Fast decoders for topological quantum codes. Physical review letters, 104(5), 050504.

[248] Duclos-Cianci, G., & Poulin, D. (2014). Fault-tolerant renormalization group decoder for Abelian topological codes. Quantum Information & Computation, 14(9&10), 721-740.

[249] Taylor, J. M., Cappellaro, P., Childress, L., Jiang, L., Budker, D., Hemmer, P. R., ... & Lukin, M. D. (2008). High-sensitivity diamond magnetometer with nanoscale resolution. Nature Physics, 4(10), 810.

[250] Maze, J. R., Stanwix, P. L., Hodges, J. S., Hong, S., Taylor, J. M., Cappellaro, P., ... & Yacoby, A. (2008). Nanoscale magnetic sensing with an individual electronic spin in diamond. Nature, 455(7213), 644.

[251] Balasubramanian, G., Chan, I. Y., Kolesov, R., Al-Hmoud, M., Tisler, J., Shin, C., ... & Hanke, T. (2008). Nanoscale imaging magnetometry with diamond spins under ambient conditions. Nature, 455(7213), 648.

[252] Acosta, V. M., Bauch, E., Ledbetter, M. P., Santori, C., Fu, K. M., Barclay, P. E., ... & Chemerisov, S. (2009). Diamonds with a high density of nitrogen-vacancy centers for magnetometry applications. Physical Review B, 80(11), 115202.

[253] Pham, L. M., Le Sage, D., Stanwix, P. L., Yeung, T. K., Glenn, D., Trifonov, A., ... & Yacoby, A. (2011). Magnetic field imaging with nitrogen-vacancy ensembles. New Journal of Physics, 13(4), 045021.

[254] Dolde, F., Fedder, H., Doherty, M. W., Nöbauer, T., Rempp, F., Balasubramanian, G., ... & Wrachtrup, J. (2011). Electric-field sensing using single diamond spins. Nature Physics, 7(6), 459.

[255] Maletinsky, P., Hong, S., Grinolds, M. S., Hausmann, B., Lukin, M. D., Walsworth, R. L., ... & Yacoby, A. (2012). A robust scanning diamond sensor for nanoscale imaging with single nitrogen-vacancy centres. Nature nanotechnology, 7(5), 320.

[256] Barry, J. F., Turner, M. J., Schloss, J. M., Glenn, D. R., Song, Y., Lukin, M. D., ... & Walsworth, R. L. (2016). Optical magnetic detection of single-neuron action potentials using quantum defects in diamond. Proceedings of the National Academy of Sciences, 113(49), 14133-14138.

[257] Childress, L., Taylor, J. M., Sørensen, A. S., & Lukin, M. D. (2005). Fault-tolerant quantum repeaters with minimal physical resources and implementations based on single-photon emitters. Physical Review A, 72(5), 052330.

[258] Childress, L., Taylor, J. M., Sørensen, A. S., & Lukin, M. D. (2006). Fault-tolerant quantum communication based on solid-state photon emitters. Physical review letters, 96(7), 070504.

[259] Childress, L., & Hanson, R. (2013). Diamond NV centers for quantum computing and quantum networks. MRS bulletin, 38(2), 134-138.

[260] Wrachtrup, J., Kilin, S. Y., & Nizovtsev, A. P. (2001). Quantum computation using the 13C nuclear spins near the single NV defect center in diamond. Optics and Spectroscopy, 91(3), 429-437.

[261] Nizovtsev, A. P., Kilin, S. Y., Jelezko, F., Gaebal, T., Popa, I., Gruber, A., & Wrachtrup, J. (2005). A quantum computer based on NV centers in diamond: optically detected nutations of single electron and nuclear spins. Optics and spectroscopy, 99(2), 233-244.

[262] Trajkov, E., Jelezko, F., Wrachtrup, J., Prawer, S., & Hemmer, P. (2005, May). Quantum computing with nitrogen-vacancy pairs in diamond. In Fluctuations and Noise in Photonics and Quantum Optics III (Vol. 5842, pp. 272-277). International Society for Optics and Photonics.

[263] Ladd, T. D., Jelezko, F., Laflamme, R., Nakamura, Y., Monroe, C., & OBrien, J. L. (2010). Quantum computers. Nature, 464(7285), 45.

[264] Yang, W. L., Yin, Z. Q., Hu, Y., Feng, M., & Du, J. F. (2011). High-fidelity quantum memory using nitrogen-vacancy center ensemble for hybrid quantum computation. Physical Review A, 84(1), 010301.

[265] Casanova, J., Wang, Z. Y., & Plenio, M. B. (2016). Noise-resilient quantum computing with a nitrogen-vacancy center and nuclear spins. Physical review letters, 117(13), 130502.

[266] Doherty, M. W., Manson, N. B., Delaney, P., Jelezko, F., Wrachtrup, J., & Hollenberg, L. C. (2013). The nitrogen-vacancy colour centre in diamond. Physics Reports, 528(1), 1-45.

[267] Balasubramanian, G., Neumann, P., Twitchen, D., Markham, M., Kolesov, R., Mizuochi, N., ... & Jacques, V. (2009). Ultralong spin coherence time in isotopically engineered diamond. Nature materials, 8(5), 383.

[268] Yang, S., Wang, Y., Rao, D. B., Tran, T. H., Momenzadeh, A. S., Markham, M., ... & Neumann, P. (2016). High-fidelity transfer and storage of photon states in a single nuclear spin. Nature Photonics, 10(8), 507.

[269] McLellan, C. A., Myers, B. A., Kraemer, S., Ohno, K., Awschalom, D. D., & Bleszynski Jayich, A. C. (2016). Patterned formation of highly coherent nitrogen-vacancy centers using a focused electron irradiation technique. Nano letters, 16(4), 2450-2454.

[270] Gupta, A., Hacquebard, L., & Childress, L. (2016). Efficient signal processing for time-resolved fluorescence detection of nitrogen-vacancy spins in diamond. JOSA B, 33(3), B28-B34.

[271] Greentree, A. D., Olivero, P., Draganski, M., Trajkov, E., Rabeau, J. R., Reichart, P., ... & Prawer, S. (2006). Critical components for diamond-based quantum coherent devices. Journal of Physics: Condensed Matter, 18(21), S825.

[272] Jiang, L., Hodges, J. S., Maze, J. R., Maurer, P., Taylor, J. M., Cory, D. G., ... & Lukin, M. D. (2009). Repetitive readout of a single electronic spin via quantum logic with nuclear spin ancillae. Science, 326(5950), 267-272.

[273] Faraon, A., Santori, C., Huang, Z., Acosta, V. M., & Beausoleil, R. G. (2012). Coupling of nitrogen-vacancy centers to photonic crystal cavities in monocrystalline diamond. Physical review letters, 109(3), 033604.

[274] Faraon, A., Barclay, P. E., Santori, C., Fu, K. M. C., & Beausoleil, R. G. (2011). Resonant enhancement of the zero-phonon emission from a colour centre in a diamond cavity. Nature Photonics, 5(5), 301.

[275] Wolters, J., Schell, A. W., Kewes, G., Nüsse, N., Schoengen, M., Döscher, H., ... & Benson, O. (2010). Enhancement of the zero phonon line emission from a single nitrogen vacancy center in a nanodiamond via coupling to a photonic crystal cavity. Applied Physics Letters, 97(14), 141108.

[276] Jiang, L., Taylor, J. M., Sørensen, A. S., & Lukin, M. D. (2007). Distributed quantum computation based on small quantum registers. Physical Review A, 76(6), 062323.

[277] Barrett, S. D., & Kok, P. (2005). Efficient high-fidelity quantum computation using matter qubits and linear optics. Physical Review A, 71(6), 060310.

[278] Lim, Y. L., Beige, A., & Kwek, L. C. (2005). Repeat-until-success linear optics distributed quantum computing. Physical review letters, 95(3), 030505.

[279] Duan, L. M., & Kimble, H. J. (2004). Scalable photonic quantum computation through cavity-assisted interactions. Physical review letters, 92(12), 127902.

[280] Young, A., Hu, C. Y., Marseglia, L., Harrison, J. P., O'Brien, J. L., & Rarity, J. G. (2009). Cavity enhanced spin measurement of the ground state spin of an NV center in diamond. New Journal of Physics, 11(1), 013007.

[281] Koshino, K., & Matsuzaki, Y. (2012). Entangling homogeneously broadened matter qubits in the weak-coupling cavity-QED regime. Physical Review A, 86(2), 020305.

[282] Nemoto, K., Trupke, M., Devitt, S. J., Stephens, A. M., Scharfenberger, B., Buczak, K., ... & Munro, W. J. (2014). Photonic architecture for scalable quantum information processing in diamond. Physical Review X, 4(3), 031022.

[283] Sun, S., & Waks, E. (2016). Single-shot optical readout of a quantum bit using cavity quantum electrodynamics. Physical Review A, 94(1), 012307.

[284] Goldman, M. L., Doherty, M. W., Sipahigil, A., Yao, N. Y., Bennett, S. D., Manson, N. B., ... & Lukin, M. D. (2015). State-selective intersystem crossing in nitrogen-vacancy centers. Physical Review B, 91(16), 165201.

[285] Felton, S., Edmonds, A. M., Newton, M. E., Martineau, P. M., Fisher, D., Twitchen, D. J., & Baker, J. M. (2009). Hyperfine interaction in the ground state of the negatively charged nitrogen vacancy center in diamond. Physical Review B, 79(7), 075203.

[286] Rabeau, J. R., Reichart, P., Tamanyan, G., Jamieson, D. N., Prawer, S., Jelezko, F., ... & Wrachtrup, J. (2006). Implantation of labelled single nitrogen vacancy centers in diamond using N 15. Applied Physics Letters, 88(2), 023113.

[287] Gruber, A., Dräbenstedt, A., Tietz, C., Fleury, L., Wrachtrup, J., & Von Borczyskowski, C. (1997). Scanning confocal optical microscopy and magnetic resonance on single defect centers. Science, 276(5321), 2012-2014.

[288] Batalov, A., Jacques, V., Kaiser, F., Siyushev, P., Neumann, P., Rogers, L. J., ... & Wrachtrup, J. (2009). Low temperature studies of the excited-state structure of negatively charged nitrogen-vacancy color centers in diamond. Physical review letters, 102(19), 195506.

[289] Tamarat, P., Manson, N. B., McMurtie, R. L., Nitsovtsev, N., Santori, C., Neumann, P., ... & Wrachtrup, J. (2006). The excited state structure of the nitrogen-vacancy center in diamond. arXiv preprint cond-mat/0610357.

[290] Chu, Y., & Lukin, M. D. (2015). Quantum optics with nitrogen-vacancy centers in diamond.

[291] Collins, A. T., Thomaz, M. F., & Jorge, M. I. B. (1983). Luminescence decay time of the 1.945 eV centre in type Ib diamond. Journal of Physics C: Solid State Physics, 16(11), 2177.

[292] Kehayias, P., Doherty, M. W., English, D., Fischer, R., Jarmola, A., Jensen, K., ... & Budker, D. (2013). Infrared absorption band and vibronic structure of the nitrogen-vacancy center in diamond. Physical Review B, 88(16), 165202.

[293] Davies, G., & Hamer, M. F. (1976). Optical studies of the 1.945 eV vibronic band in diamond. Proc. R. Soc. Lond. A, 348(1653), 285-298.

[294] Davies, G. (1974). Vibronic spectra in diamond. Journal of Physics C: Solid state physics, 7(20), 3797.

[295] Jelezko, F., Popa, I., Gruber, A., Tietz, C., Wrachtrup, J., Nizovtsev, A., & Kilin, S. (2002). Single spin states in a defect center resolved by optical spectroscopy. Applied physics letters, 81(12), 2160-2162.

[296] Santori, C., Barclay, P. E., Fu, K. C., Beausoleil, R. G., Spillane, S., & Fisch, M. (2010). Nanophotonics for quantum optics using nitrogen-vacancy centers in diamond. Nanotechnology, 21(27), 274008.

[297] Albrecht, R., Bommer, A., Pauly, C., Mücklich, F., Schell, A. W., Engel, P., ... & Becher, C. (2014). Narrow-band single photon emission at room temperature based on a single nitrogen-vacancy center coupled to an all-fiber-cavity. Applied Physics Letters, 105(7), 073113.

[298] Johnson, S., Dolan, P. R., Grange, T., Trichet, A. A. P., Hornecker, G., Chen, Y. C., ... & Smith, J. M. (2015). Tunable cavity coupling of the zero phonon line of a nitrogen-vacancy defect in diamond. New Journal of Physics, 17(12), 122003.

[299] Su, C. H., Greentree, A. D., & Hollenberg, L. C. (2008). Towards a picosecond transform-limited nitrogen-vacancy based single photon source. Optics Express, 16(9), 6240-6250.

[300] Robledo, L., Bernien, H., Van Der Sar, T., & Hanson, R. (2011). Spin dynamics in the optical cycle of single nitrogen-vacancy centres in diamond. New Journal of Physics, 13(2), 025013.

[301] Tetienne, J. P., Rondin, L., Spinicelli, P., Chipaux, M., Debuisschert, T., Roch, J. F., & Jacques, V. (2012). Magnetic-field-dependent photodynamics of single NV defects in diamond: an application to qualitative all-optical magnetic imaging. New Journal of Physics, 14(10), 103033.

[302] Acosta, V. M., Jarmola, A., Bauch, E., & Budker, D. (2010). Optical properties of the nitrogen-vacancy singlet levels in diamond. Physical Review B, 82(20), 201202.

[303] Hu, C. Y., Young, A., OBrien, J. L., Munro, W. J., & Rarity, J. (2008). Giant optical Faraday rotation induced by a single-electron spin in a quantum dot: applications to entangling remote spins via a single photon. Physical Review B, 78(8), 085307.

[304] Bonifacio, R., & Lugiato, L. A. (1976). Cooperative effects and bistability for resonance fluorescence. Optics Communications, 19(2), 172-176.

[305] Hilborn, R. C. (1982). Einstein coefficients, cross sections, f values, dipole moments, and all that. American Journal of Physics, 50(11), 982-986.

[306] Rephaeli, E., & Fan, S. (2012). Few-photon single-atom cavity QED with input-output formalism in Fock space. IEEE Journal of Selected Topics in Quantum Electronics, 18(6), 1754-1762.

[307] Gardiner, C. W., & Collett, M. J. (1985). Input and output in damped quantum systems: Quantum stochastic differential equations and the master equation. Physical Review A, 31(6), 3761.

[308] Reiserer, A., Kalb, N., Blok, M. S., van Bemmelen, K. J., Taminiau, T. H., Hanson, R., ... & Markham, M. (2016). Robust quantum-network memory using decoherence-protected subspaces of nuclear spins. Physical Review X, 6(2), 021040.

[309] First Sensor (2016, March 29). Silicon Photomultipliers Datasheet. Retrieved from http://www.first-sensor.com/cms/upload/datasheets/SiPM-RGB_501629.pdf

[310] Excelitas Technologies (2016, March 29). Single Photon Counting Module Datasheet. Retrieved from http://www.excelitas.com/Downloads/DTS_SPCM-AQRH.pdf

[311] Laser Components (2016, March 29). Single Photon Counting Modules Datasheet. Retrieved from http://www.lasercomponents.com/fileadmin/user_upload/home/Datasheets/lcp/count-series.pdf

[312] Janitz, E., Ruf, M., Dimock, M., Bourassa, A., Sankey, J., & Childress, L. (2015). Fabry-Perot microcavity for diamond-based photonics. Physical Review A, 92(4), 043844.

[313] ID Quantique (2016, March 26). ID350 PPLN Photon Pair Source Datasheet. Retrieved from http://marketing.idquantique.com/acton/attachment/11868/f-0039/1/-/-/-/-/ID350%20Datasheet.pdf

[314] Somaschi, N., Giesz, V., De Santis, L., Loredo, J. C., Almeida, M. P., Hornecker, G., ... & Gómez, C. (2016). Near-optimal single-photon sources in the solid state. Nature Photonics, 10(5), 340.

[315] Single Quantum (2016, June 19). Products. Retrieved from http://www.singlequantum.com/products/

[316] Scontel (2016, June 19). SSPD Brochure. Retrieved from http://www.scontel.ru/data/uploads/datasheet/brochure_sspd-newest.pdf

[317] Photon Spot (2016, June 19). Detectors. Retrieved from http://www.photonspot.com/detectors

[318] Quantum Opus (2016, June 19). Product Information. Retrieved from http://www.quantumopus.com/index.php/product-information/

[319] Volz, J., Gehr, R., Dubois, G., Estève, J., & Reichel, J. (2011). Measurement of the internal state of a single atom without energy exchange. Nature, 475(7355), 210.

[320] Aslam, N., Waldherr, G., Neumann, P., Jelezko, F., & Wrachtrup, J. (2013). Photo-induced ionization dynamics of the nitrogen vacancy defect in diamond investigated by single-shot charge state detection. New Journal of Physics, 15(1), 013064.

[321] Siyushev, P., Pinto, H., Vörös, M., Gali, A., Jelezko, F., & Wrachtrup, J. (2013). Optically controlled switching of the charge state of a single nitrogen-vacancy center in diamond at cryogenic temperatures. Physical review letters, 110(16), 167402.

[322] Beha, K., Batalov, A., Manson, N. B., Bratschitsch, R., & Leitenstorfer, A. (2012). Optimum photoluminescence excitation and recharging cycle of single nitrogen-vacancy centers in ultrapure diamond. Physical review letters, 109(9), 097404.

[323] Robledo, L., Bernien, H., Van Weperen, I., & Hanson, R. (2010). Control and coherence of the optical transition of single nitrogen vacancy centers in diamond. Physical review letters, 105(17), 177403.

[324] Burkard, G. (2014). Diamond spins shining bright. Physics, 7, 131.

[325] Rogers, L. J., Jahnke, K. D., Metsch, M. H., Sipahigil, A., Binder, J. M., Teraji, T., ... & Jelezko, F. (2014). All-optical initialization, readout, and coherent preparation of single silicon-vacancy spins in diamond. Physical review letters, 113(26), 263602.

[326] Pingault, B., Jarausch, D. D., Hepp, C., Klintberg, L., Becker, J. N., Markham, M., ... & Atatüre, M. (2017). Coherent control of the silicon-vacancy spin in diamond. Nature communications, 8, 15579.

[327] Meesala, S., Sohn, Y. I., Pingault, B., Shao, L., Atikian, H. A., Holzgrafe, J., ... & Burek, M. J. (2018). Strain engineering of the silicon-vacancy center in diamond. arXiv preprint arXiv:1801.09833.

[328] Wang, C., Kurtsiefer, C., Weinfurter, H., & Burchard, B. (2005). Single photon emission from SiV centres in diamond produced by ion implantation. Journal of Physics B: Atomic, Molecular and Optical Physics, 39(1), 37.

[329] Jahnke, K. D., Sipahigil, A., Binder, J. M., Doherty, M. W., Metsch, M., Rogers, L. J., ... & Jelezko, F. (2015). Electronphonon processes of the silicon-vacancy centre in diamond. New Journal of Physics, 17(4), 043011.

[330] Sukachev, D. D., Sipahigil, A., Nguyen, C. T., Bhaskar, M. K., Evans, R. E., Jelezko, F., & Lukin, M. D. (2017). Silicon-Vacancy Spin Qubit in Diamond: A Quantum Memory Exceeding 10 ms with Single-Shot State Readout. Physical review letters, 119(22), 223602.

[331] Bergmann, K., Vitanov, N. V., & Shore, B. W. (2015). Perspective: stimulated Raman adiabatic passage: the status after 25 years. The Journal of chemical physics, 142(17), 170901.

[332] Hepp, C., Müller, T., Waselowski, V., Becker, J. N., Pingault, B., Sternschulte, H., ... & Becher, C. (2014). Electronic structure of the silicon vacancy color center in diamond. Physical Review Letters, 112(3), 036405.

[333] Zhang, J. L., Sun, S., Burek, M. J., Dory, C., Tzeng, Y. K., Fischer, K. A., ... & Melosh, N. A. (2018). Strongly Cavity-Enhanced Spontaneous Emission from Silicon-Vacancy Centers in Diamond. Nano letters, 18(2), 1360-1365.

[334] Becker, J. N., Pingault, B., Groß, D., Gündoğan, M., Kukharchyk, N., Markham, M., ... & Becher, C. (2018). All-optical control of the silicon-vacancy spin in diamond at millikelvin temperatures. Physical review letters, 120(5), 053603.

[335] Higbie, J. M., Perreault, J. D., Acosta, V. M., Belthangady, C., Lebel, P., Kim, M. H., ... & Santori, C. (2017). Multiphoton-excited fluorescence of silicon-vacancy color centers in diamond. Physical Review Applied, 7(5), 054010.

[336] Häußler, S., Thiering, G., Dietrich, A., Waasem, N., Teraji, T., Isoya, J., ... & Kubanek, A. (2017). Photoluminescence excitation spectroscopy of SiV and GeV color center in diamond. New Journal of Physics, 19(6), 063036.

[337] Becker, J. N., Görlitz, J., Arend, C., Markham, M., & Becher, C. (2016). Ultrafast all-optical coherent control of single silicon vacancy colour centres in diamond. Nature communications, 7, 13512.

[338] Sohn, Y. I., Meesala, S., Pingault, B., Atikian, H. A., Holzgrafe, J., Gündoğan, M., ... & Zhang, M. (2017). Engineering a diamond spin-qubit with a nano-electro-mechanical system. arXiv preprint arXiv:1706.03881.

[339] Greentree, A. D., Cole, J. H., Hamilton, A. R., & Hollenberg, L. C. (2004). Coherent electronic transfer in quantum dot systems using adiabatic passage. Physical Review B, 70(23), 235317.

[340] Everitt, M. S., Devitt, S., Munro, W. J., & Nemoto, K. (2014). High-fidelity gate operations with the coupled nuclear and electron spins of a nitrogen-vacancy center in diamond. Physical Review A, 89(5), 052317.

[341] Farfurnik, D., Jarmola, A., Pham, L. M., Wang, Z. H., Dobrovitski, V. V., Walsworth, R. L., ... & Bar-Gill, N. (2016, April). Improving the coherence properties of solid-state spin ensembles via optimized dynamical decoupling. In Quantum Optics (Vol. 9900, p. 99000N). International Society for Optics and Photonics.

[342] Riedrich-Möller, J., Arend, C., Pauly, C., Mücklich, F., Fischer, M., Gsell, S., ... & Becher, C. (2014). Deterministic coupling of a single silicon-vacancy color center to a photonic crystal cavity in diamond. Nano letters, 14(9), 5281-5287.

[343] Piparo, N. L., Razavi, M., & Munro, W. J. (2017). Measurement-device-independent quantum key distribution with nitrogen vacancy centers in diamond. Physical Review A, 95(2), 022338.

[344] Park, D. (2010). Relative entropy of entanglement for two-qubit state with z-directional Bloch vectors. International Journal of Quantum Information, 8(05), 869-879.

[345] Browne, D. E., Elliott, M. B., Flammia, S. T., Merkel, S. T., Miyake, A., & Short, A. J. (2008). Phase transition of computational power in the resource states for one-way quantum computation. New Journal of Physics, 10(2), 023010.

[346] Jones, E., Oliphant, E., Peterson, P., et al. SciPy: Open Source Scientific Tools for Python, 2001-, http://www.scipy.org/ [Online; accessed 2018-05-10].

[347] Prince, P. J., & Dormand, J. R. (1981). High order embedded Runge-Kutta formulae. Journal of Computational and Applied Mathematics, 7(1), 67-75.

[348] Nelder, J. A., & Mead, R. (1965). A simplex method for function minimization. The computer journal, 7(4), 308-313.

[349] SIMD-oriented Fast Mersenne Twister (SFMT) (2019, Jan 10). Retrieved from http://www.math.sci.hiroshima-u.ac.jp/~m-mat/MT/SFMT/index.html

[350] The Boost Graph Library (2019, Jan 10). Retrieved from https://www.boost.org/doc/libs/1_69_0/libs/graph/doc/index.html